DISSERTATION

LAND SURFACE SENSITIVITY OF MESOSCALE CONVECTIVE SYSTEMS

Submitted by

Robert C. Tournay

Department of Atmospheric Science

In partial fulfillment of the requirements

For the Degree of Doctor of Philosophy

Colorado State University

Fort Collins, Colorado

Fall 2016

Doctoral Committee:

Advisor: Russ Schumacher
Co-Advisor: Thomas Vonder Haar

Susan van den Heever
Peter Nelson

Copyright by Robert C. Tournay 2016

All Rights Reserved

ABSTRACT

LAND SURFACE SENSITIVITY OF MESOSCALE CONVECTIVE SYSTEMS

Mesoscale convective systems (MCSs) are important contributors to the hydrologic cycle in many regions of the world as well as major sources of severe weather. MCSs continue to challenge forecasters and researchers alike, arising from difficulties in understanding system initiation, propagation, and demise. One distinct type of MCS is that formed from individual convective cells initiated primarily by daytime heating over high terrain. This work is aimed at improving our understanding of the land surface sensitivity of this class of MCS in the contiguous United States.

First, a climatology of mesoscale convective systems originating in the Rocky Mountains and adjacent high plains from Wyoming southward to New Mexico is developed through a combination of objective and subjective methods. This class of MCS is most important, in terms of total warm season precipitation, in the 500 to 1300m elevations of the Great Plains (GP) to the east in eastern Colorado to central Nebraska and northwest Kansas. Examining MCSs by longevity, short lasting MCSs (<12 hrs), medium (12-15 hrs) and long lasting MCSs (>15 hrs) reveals that longer lasting systems tend to form further south and have a longer track with a more southerly track. The environment into which the MCS is moving showed differences across commonly used variables in convection forecasting, with some variables showing more favorable conditions throughout (convective inhibition, 0-6 km shear and 250 hPa wind speed) ahead of longer lasting MCSs. Other variables, such as convective available potential energy,

showed improving conditions through time for longer lasting MCSs. Some variables showed no difference across longevity of MCS (precipitable water and large-scale vertical motion).

From subsets of this MCS climatology, three regions of origin were chosen based on the presence of ridgelines extending eastward from the Rocky Mountains known to be foci for convection initiation and subsequent MCS formation: Southern Wyoming (Cheyenne Ridge), Colorado (Palmer divide) and northern New Mexico (Raton Mesa). Composite initial and boundary conditions were developed from reanalysis data, from which control runs of regional MCSs were made as well a series of idealized experiments with imposed large scale soil moisture (SM) anomalies to study to impact to each regional MCS on SM variations in initiation region as well down stream in the GP. Another idealized experiment was made to study the impact of varying the planetary boundary layer (PBL) parameterization in the context of the idealized SM variations. While the distribution of SM has a major impact on CAPE and the location and magnitude of CI, also important is the differences in shear driven by the differences in large scale SM, playing a major, and varying depending on where the regional MCSs interact with the shear anomalies. Utilizing a different PBL parameterization impacts the timing and amount of initial CI, impacting the total precipitation produced by the MCSs, but not nearly the magnitude of alteration to the MCS as varying the SM distribution.

A climatology of CI in the Rocky Mountains and adjacent high plains is made using a high resolution observational dataset. From this climatology, the sensitivity of CI to land surface variables, including SM and vegetation is studied. It was found that the timing of CI had a stronger relationship with SM, with earlier CI over wetter than average soils, with the greatest difference in May in the north of the domain, nearly all statistical significant values across regions from north to south in June and July with little difference in August in the northern regions. Outside of May, which showed a strong relationship of earlier CI over less vegetated regions, the relationship was similar, but weaker than, that between SM and CI timing. Examining the CAPE, CIN and PW at CI and null points reveal that the values are generally more conducive to CI over wet soils and anomalously vegetated areas at both CI and null points, with stronger difference in the high plains in the east of regions. Examining the covariance of SM and vegetation at CI points revealed that July and August showed expected covariance relationships with concurrently measured convective variables (i.e., high SM/vegetation associated with high CAPE and vice versa for low SM/vegetation) while May and June higher CAPE and CIN over low vegetation anomalies.

A climatology of elevated mixed layers in the central GP was conducted, revealing that the greatest number of EMLS occurred in the northern GP. Back trajectories (BT) were conducted from the radiosonde point of detection for 18 and 36 hours, revealing that the BT point mean for days with severe weather were further west and south from the origin point. The SM and vegetation was sampled at the BT point, revealing a negative, significant correlation with EML depth when pooling the northern stations in 18-hr BTs, and a significant, negative correlation with EVI when pooling the southern sites. A modeling case study was conducted in which an idealized SM anomaly was imposed over the EML origin region. Experiments were also conducted to test the sensitivity of ML formation and EML transport using different PBL parameterizations. While the YSU PBL parameterization produced the deeper PBL over anonymously dry soils in the EML origin region, the EML was not transported to the east as it was in those experiments using the MYNN parameterization, impacting the timing and extent of precipitation in the model runs.

ACKNOWLEDGEMENTS

This research was supported by the United States Air Force. Stage IV precipitation data were obtained from the UCAR Earth Observing Laboratory. NARR data were obtained from the NCDC NOMADS server. MODIS data were obtained from the USGS Land Process Distributed Active Archive Center. Special thanks are given to the committee members – Tom Vonder Haar, Sue van den Heever and Peter Nelson for their guidance and support through this research. Thanks to all Schumacher Group members, especially Erik, Greg and John. And of course, thank you to my family for continuing to put up with me and all the moves we've been through over the years.

TABLE OF CONTENTS

CHAPTER 1

INTRODUCTION

At first order, the relationship between soil moisture (SM) and the overlaying atmosphere is simple in terms of the Bowen Ratio (sensible heat flux over latent heat flux). Over dry soil the Bowen Ratio is high as little incoming short wave radiation from the Sun is partitioned into latent heat flux, driving a warmer, dryer planetary boundary layer (PBL). When soils are more moist, more incoming short wave radiational heating is partitioned into latent heat flux, keeping the temperature of the PBL cooler and moister as SM is evaporated into the atmosphere.

With regards to the relationship between SM and deep, moist convection, the picture is clouded first by the state of the atmosphere above the PBL. Ek and Holtslag (2004) found mixed results regarding cumulus development depending on boundary layer and just above boundary layer conditions. They found that increased SM leads to increased cumulus cloud formation if the stability above the boundary layer is not too weak, whereas drier soils and weak stability above also leads to more cumulus cloud formation. At convective spatial scales, the distribution of SM is important for convection initiation (CI). Avissar and Liu (1994), using a model at convection permitting scales showed that the gradient of soil moisture was important on the mesoscale in developing convection by creating differential sensible and latent heat fluxes leading to differences in temperature and density over moist and dry surfaces, thus creating solenoidal circulations between the contrasting surfaces. The internal workings of numerical models impact the feedback between SM and convection as shown by Hohenneger et al (2009) , who found that the grid spacing and the use of convective parameterization in numerical simulations caused a switch between a positive and negative feedback between soil moisture and precipitation. Not to mention the complex pathways in which SM enters the atmosphere in the presence of vegetation, depending on the density of coverage of vegetation, type, root depth and health among other factors.

It has long been known that Rocky Mountains and High Plains provide a focal point for convection initiation for storms that then move eastward into the Great Plains, beginning with studies of crop damage from hail (Crow 1967), studies with early radar (Henz 1974) and studies with the first geostationary satellite data records (Banta and Schaaf 1987). More recently, Carbone et al. (2002) and Carbone and Tuttle (2008), using the WSI NOWrad dataset, a quality controlled dataset derived from WSR-88D radar data, found a distinct west to east propagating diurnal pattern, beginning with a maximum over the Rocky Mountains at 2100 UTC moving rapidly into the central Great Plains by 0700 UTC then more slowly into the eastern Great Plains by 1300 UTC then next morning. Highlighting the hydrologic importance of these systems, Schumacher and Johnson (2005) found 116 precipitation events that exceeded the 50-year recurrence interval from 1999 to 2001. They determined that 65% of events were associated with MCS activity.

CI remains a challenge to both forecasters and researchers to understand when and where CI will occur, what environmental factors are important in order to accurately portray CI in numerical models, as well as understanding the impact of timing and spatial errors in CI have on subsequent forecasts. Zhang et al. (2015) found that small shifts in simulation parameters, such as terrain and time, influenced planetary boundary layer and large-scale environmental characteristics, which then influenced timing and position of CI. The errors associated with CI timing and position then propagated through the simulation leading to large forecast uncertainties of subsequent supercells and mesoscale convective systems (MCSs).

A common feature throughout the central US throughout the warm season is the elevated mixed layer (EML), a region of steep, near adiabatic lapse rates found in the mid-levels, often associated with being formed in the higher terrain of the US and Mexico then advected over the lower laying terrain of the central Great Plains. The EML, located above a locally developed PBL that is generally cooler and moister, can act as a "lid" on deep, moist convection if the inversion at the base of the EML is sufficiently strong. The EML can also provide an environment for vigorous convection due to the associated steep lapse rate, if sufficiently warm and/or moist air exists below the EML.

In light of the complexities feedbacks between SM and the overlaying atmosphere and the importance of warm season MCSs to the hydrology and severe weather impact to a large portion of the US, this thesis seeks to understand the impact of SM and vegetation on MCSs originating in the Rocky Mountains and adjacent High Plains (RM/HP). In Chapter II, a climatology of MCSs originating in the RM/HP is developed to determine the frequency of occurrence, regions of origin and relationship between observed atmospheric and land surface variables to MCS longevity. This climatology is then used in two subsequent studies.

In Chapter III, subsets of the MCS climatology are extracted based on region of origin: Southern Wyoming, Colorado and Northern New Mexico. Using mean initial conditions from each region, the characteristics of each MCS will be studied then subject to idealized SM conditions to study the impact on MCS lifecycle.

Chapter IV contains a study of CI in the MCS origin region was undertaken using a high resolution precipitation data set. The temporal and spatial characteristic of CI in the region was studies, as well as the relationship between the SM and vegetation with overlaying atmospheric variables at the point of CI. Characteristics of CI on days which MCSs formed in the region were compared to days without MCSs formed in the region.

In addition to these three studies, a fourth study (Chapter V) was undertaken to examine the impact of SM and vegetation on EML formation. This was accomplished using radiosonde data from the central GP and back trajectories to the point of origin of the EML over high terrain to the west. A modeling case study under quasi -idealized conditions was accomplished to examine the role of an imposed SM anomaly as well as to examine the choice of PBL parameterization in developing and advecting an EML downstream to lower terrain.

CHAPTER 2

CLIMATOLOGY OF MCSS BORN IN THE ROCKY MOUNTAINS AND HIGH PLAINS OF THE US

2.1. Introduction

The Rocky Mountains and adjacent High Plains to the east provide a focal point for convection initiation for storms that then move eastward into the Great Plains. Crow (1967) in a study on hail using crop damage reports from insurers in Colorado, Nebraska, and Kansas found a distinct eastward progression in peak number of reports of hourly precipitation amounts greater than 0.1 inch from Fort Collins, CO at 2200-0000 UTC to successive stations eastward at 50 to 100 mile intervals to Wichita, KS, with a peak at 0700-0900 UTC, though no scientific explanation was provided for the phenomenon. Henz (1974),using WSR-57 weather radar data and Banta and Schaaf (1987),using geostationary satellite data, traced mature thunderstorm signatures back to the point of initiation over the Palmer Divide and Raton Mesa (topographic features highlighted in Fig. 2.11 in red elevation contours in central Colorado and on the Colorado/New Mexico Border respectively). More recently, Carbone et al. (2002) and Carbone and Tuttle (2008), using the WSI NOWrad dataset, a quality controlled dataset derived from WSR-88D radar data, found a distinct west to east propagating diurnal pattern, beginning with a maximum over the Rocky Mountains at 2100 UTC moving rapidly into the central Great Plains by 0700 UTC then more slowly into the eastern Great Plains by 1300 UTC then next morning.

Several climatology and classification studies of contiguous United States (CONUS) MCS and rainfall extrema have been produced. With the availability of a sufficient record of satellite observations, Maddox (1980) studied the prevalence of CONUS Mesoscale Convective

Complexes (MCCs). Houze et al. (1990) examined six years of Norman, Oklahoma WSR-57 radar data, assessing the degree of symmetry and prevalence of trailing stratiform in 63 systems. Parker and Johnson (2000), studying two years of nationwide WSR-88D data, identified 88 linear MCSs and classified each as trailing, leading or parallel stratiform, and discussed typical synoptic environments and evolution and presented case studies of each type. They found that the majority of cases were trailing stratiform and that each class existed in distinct storm relative flow environments. Highlighting the hydrological importance of MCSs, Schumacher and Johnson (2005) found 116 precipitation events that exceeded the 50-year recurrence interval from 1999 to 2001. They determined that 65% of events were associated with MCS activity. In addition to these climatology studies on specific types and impacts of MCS, several review articles of MCC/MCSs have been produced (Cotton and Anthes (1989), Fritsch and Forbes (2001) and Houze (2004)), detailing the state of the science on dynamics and climatology these systems.

Studies have been undertaken to understand factors contributing to the longevity of MCSs. Gale et al (2002) examined 47 nocturnal MCSs in Iowa and surrounding states from 1998-1999, finding that the low-level horizontal vorticity balance described in Rotunno et al. (1988, RKW88) was not important in longevity, as most of the storms studied formed in sub-optimal RKW balance conditions but progressed as MCSs. Rather, they found disconnect of the MCS from the low-level jet (LLJ), either through the system moving away for the LLJ dissipating, and/or rapid decrease in low or mid-level lapse rates to be the most common factors in dissipation. Coniglio et al (2007) identified 290 rapidly moving MCS (>10m/s) with proximity soundings, defined each as initiating, mature or decaying and identified the factors of maximum deep shear, 3-8-km lapse rate, CAPE, and 3-12 km mean wind speed as the most important factors. Using these factors, they developed a regression equation to predict MCS maintenance. Hane et al (2008) made a comprehensive study of Southern Plains MCSs collected by the Norman, Oklahoma and Dodge City, Kansas National Weather Service offices. They focused on systems transitioning from night-to-day over a 5-year period, finding 145 systems. While the majority of systems dissipated in the morning hours, 28% maintained intensity or strengthened. Then, taking a subset of 48 systems (32 decreasing in intensity, 16 increasing in intensity in the morning), they determined that CAPE, 350 hPa meridional wind component, system speed and system direction were the best discriminators between the two groups. Coniglio et al (2010) examined 94 MCS from 2005-2008 that met a strict criteria of being rapidly moving, long-lived and underwent a prescribed lifecycle, then broke this group into rapidly and slowly developing systems, then into long and short lived systems. Rapidly developing systems were found to have higher CAPE, lower 3-10km shear environments as well has being closer to a stronger LLJ than the slowly developing systems. Long-lived systems were found to exist in environments with broader, more southerly LLJs, in more well defined frontal zones and existed in stronger deep layer shear than the short lived systems.

From the early days of satellite and radar climatologies of MCC/MCSs, it was recognized that the high terrain of the Rocky Mountains and adjacent High Plains is an area of favored warm season convection initiation and region of transition from single to multicellular storm systems. The South Park Area Cumulus Experiment (SPACE) and High Plains Experiment (HiPlEX) of 1977 were designed to study the relationship between Rocky Mountain and High Plains convection. A case from these experiments is detailed in Cotton et al. (1983) in which a nocturnal Great Plains MCS is born from convection in the Rocky Mountains. The dynamics of this type of MCS was detailed in a 2-dimensional modelling study by Tripoli and Cotton (1989).

While several climatology studies of CONUS MCSs have been accomplished, the first goal of this study is to develop a climatology of warm season, weakly-forced MCSs originating from discrete convective cells initiated above 1100 meters elevation, west of -102 W and east of -106 W longitude, in the Rocky Mountains and High Plains from southern Wyoming southward through central New Mexico. The first section of the paper describes the data and methods of the observational climatology study. The second section describes the results of this climatology, examining the mean characteristics of these MCSs by mean life time of system, as well as where these systems produce precipitation relative to all warm season precipitation. The third section continues the analysis of MCSs by longevity, examining the atmospheric and land surface environment these systems encounter. Section 4 examines the MCSs by region of origin and section 5 presents a summary and conclusion.

2.2 Orogenic Precipitation and MCS Climatology

2.2.a. Data and Methods

A system for identifying and tracking precipitating systems east of the Rocky Mountains in the CONUS utilizing hourly Stage IV precipitation analyses (Lin and Mitchell 2005) was developed, similar in thresholds and design to Clark et al (2014), in which an object-based, objective method to identify and track precipitation systems developed for the purpose of verifying members of a high-resolution operational ensemble. Here, a convective precipitation system (CPS) is defined as a contiguous region of at least 100 grid points (~2,500km^2) of greater than 2 mm/hr precipitation rate. An automated system utilizing the Python programming language library Scipy (Oliphant and Peterson 2008) identifies the center of mass (CoM) of the CPS, and records the CoM position, total precipitation, areal extent of the system and assigns an identifying number, which is used to track the system through time while it meets the size and intensity criteria.

Tracking was accomplished using a mask based on the climatological tendency of precipitating systems to move eastward with time. At the starting time used in the study, 0300 UTC, all CPSs meeting the criteria were identified and given an identifying number and characteristics, including CoM latitude and longitude, size of contiguous precipitation area and total precipitation rate, were recorded in a database. At the next hour, all CPSs meeting the criteria were identified and numbered. Over each CoM, the mask was placed and all prior time step CoMs under the mask were identified. If more than one lies under the mask, the one closest to the size and precipitation rate characteristics of the current time step CPS is maintained and the system is tracked through time. A diagram illustrating the masking method is shown in Fig. 2.1.

Fig. 2.2 shows an example of the CPS tracking system for one of the MCSs identified in this study. Fig. 2.2a shows the NEXRAD mosaic composite reflectivity for 1947 UTC with the weak returns of a few individual, single-cell storms beginning to form on the eastern boundary of the study region in SE Colorado. While Stage IV shows precipitation accumulation at 2000 UTC in the region (Fig. 2.2b), the area of 2 mm/hr precipitation rate is not of sufficient size. By 2125 UTC, in Fig. 2.2c, the multiple supercell storms have formed from the initial convection initiation in SE CO, still along the eastern boundary of the area of study, but still no area of sufficient size and intensity to be picked up by the objective tracking system in the Stage IV data in Fig. 2.2d. At 0000 UTC on 26 May, the objective tracking system recognizes the convection moving out of central Colorado as a CPS (Fig. 2.2f). The NEXRAD composite reflectivity depiction at 2355 shows multiple supercell storms transitioning from single cell to an MCS. At

0200 UTC the MCS continues to be tracked by the objective tracking system as the size of the precipitation area and intensity of hourly precipitation rate increases as the radar depiction shows increased multicellular organization. By 0400 UTC the system is mature quasi-linear MCS with trailing stratiform precipitation shown in the radar depiction in Fig. 2.2h with the continued tracking of the system from Stage IV data shown in Fig. 2.2g.

From a database of all CONUS CPSs, all possible candidates for warm-season (May through August) MCSs originating from discrete convective cells over high terrain were separated if they existed in central and/or southern Great Plains at 0600 UTC. These candidates were then tracked back using both the objective tracking criteria above as well as subjective tracking of precipitation signatures on NEXRAD composites (from http://locust.mmm.ucar.edu). Subjective tracking was accomplished due to the tracking algorithm failing during the initiation of the individual storms at higher terrain as well as the limitations of the Stage IV data in the Rocky Mountains due to the lack of rain gauge data and poor performance of the NEXRAD network due to terrain interference. MCSs were retained in this climatology only if no precipitation existed within the region of origin at 1600 UTC to rule out more strongly-forced (i.e., synoptically forced) systems.

2.2.b. Climatology Results

From 2002 to 2013 232 systems were identified using the methods in section 2a above. Due to missing Stage IV data along the MCS track, 30 systems were not used in the remaining analysis. Of the 202 analyzed systems, 28 occurred in May, 77 in June, 45 in July and 52 occurred in August with 3 July being the mean date of occurrence. The mean initiation of the objective tracking system was 2330 UTC while the mean end time of the tracking was 1130 UTC the following day, making the mean lifespan of this type of MCS 12 hours.

With knowledge of the general motion of MCSs by region known and knowledge of the topography of the central CONUS a Hovmöller-like approach is taken to downscale the data and understand the evolution of these MCSs through time and space and to examine where geographically precipitation from these systems is most important in regards to the whole. Instead of averaging values of Stage IV precipitation rate data by longitude, as in a traditional Hovmöller, the data will be averaged in elevation bins (0-100 m, 100-200m, etc.) to examine evolution through time of the MCSs as they move from higher to lower terrain.

Fig. 2.3 shows distributions of area mean precipitation rate (mm/hr), averaged over the total area of the elevation bin, within given elevation bins through time from 1500 UTC through 1200 UTC the next day for days with MCSs (232 days) in (a) and all other days (b) in May through August 2002-2013 (1244 days). During MCS days the initiation of precipitation is clear in the peak at 2300 UTC in the highest elevation bin (1800-2000 meters). Through time, the area-averaged precipitation rate shows distinct growth with a definite signal from higher to lower elevations present, with the peak intensity seen at 600-800meters elevation at 0600-0700 UTC. The signal continues to lower elevations with less intensity through time after 0700 UTC. Of note, the lowest elevation bin, while showing some signs of the MCS activity with a peak at 1000-1200 UTC, follows a different pattern than the other elevation bins with a flatter curve (more precipitation through all times and a primary peak at 2200 UTC with afternoon thunderstorm activity, showing that, in this geographic window that other precipitation processes than the MCSs under study are important for precipitation at this elevation.

Fig. 2.3b shows the same diagram but for all days other than the 232 days in which MCSs under study occurred (1244 days). While similarly narrow distributions of precipitation rate over time exists at elevations above 1200 meters, the magnitudes of the maxima of precipitation rate decrease with time and are at roughly half the magnitude or less than for the MCS case graph. The peak area-averaged rain rate is greatest at the highest elevations and decreases successively down to the 1200-1400 m elevation bin. Below 1200 meters, the average precipitation rate distributions flatten considerably but do show increasing intensity through time and to lower elevations. Once again, the 0-200 meter bin shows behavior differing from the other bins with an afternoon maximum at 2200 UTC.

Comparing MCS-day to non-MCS-day averages we find that for both cases the primary maxima of precipitation begin at the highest elevations and the lowest elevations. Through time, the area averaged precipitation maximum is found at lower elevations and this maximum increases through time through 0600 UTC (midnight local time) in the MCS case. In the non-MCS case average the elevation bin average is found at later times, indicating a weaker translation of precipitation to lower elevations and less or no upscale growth or organization. In the non-MCS case, possible storm organization is found in the signal below 1200 meters, with precipitation maxima increasing through time and to lower elevations, but it is less clear if this activity is related to the storms originally initiated over higher terrain.

Examining the relative importance of precipitation from the MCSs under study to precipitation by all other processes in the warm season, Fig. 2.4 shows a graph of the proportion of precipitation from weakly-forced MCSs to all other warm season precipitation by elevation. It is clear from this graph that MCS precipitation is not as relatively important at the highest and lowest elevations but is much more important in between in the 500-1300 meters elevation range.

Fig. 2.5 shows a map of the percentage of precipitation from MCS days versus precipitation from non-MCS days across the region. First, the area with the highest percentage is, of course, in the elevation range from Eastern Colorado eastward in to central Nebraska, Kansas, Western Oklahoma and the Texas Panhandle. From the maximum value in the SW Kansas, near Dodge City, where nearly 90% of May through August precipitation comes on days of this type of MCS, there appear to be two MCS storm tracks emanating: one, shorter track to the SE through the Texas Panhandle and Western Oklahoma and one to the east along the Kansas/Oklahoma border. The track to the SE is shorter but broader, ending abruptly near Wichita Falls, Texas. Within this track, the percentage of precipitation from these MCSs constitutes a large percentage, with widespread values of 50% and greater with numerous areas of 70% throughout. In the easterly storm track, the percentages from these MCSs is much lower, with widespread values of up to 40% from these MCSs with very few maxima up to the 60% value. This track is much longer, extending into Missouri. To the north, MCS originating from northern Colorado to Southern Wyoming constitute a large percentage of the total warm season precipitation. MCS days make up a much greater percentage of the total warm season precipitation at higher elevations from central Colorado and northward than in the southern half of the domain. The greatest percentage from MCS day precipitation is in Western Nebraska, in the Platte River region. This area extends into eastern Nebraska and ends abruptly before reaching the Missouri River.

Examining only storms with lifespans between 9 and 18 hours (179 total) to analyze the difference between short (9-12 hours), medium (12-15) and long (15-18 hours) lasting MCSs, 59 were found in the short category, 64 in the medium and 56 in the long category. Fig. 2.6 shows the beginning (star) and end (circle) for all systems in each of the three categories with the mean track plotted. Note that several of the start points lay outside the domain where initiation was considered (west of -102 E longitude). This is due to the initial cells forming within the domain, but a contiguous precipitation rate area in Stage IV of sufficient size and intensity not forming until outside the domain (as in the example in Fig. 2.2). Intuitively, the long lasting MCSs have the longest track, ending in north central Oklahoma, medium ending in south central Kansas and short ending in western Kansas. The longer the mean track, the more the mean track pushes southward into the southern Great Plains. The mean average start being further south with lifespan is explained by the mean date of each type. Short lifespan MCSs occur on average on 28 June, medium lifespan MCSs on 2 July and long lifespan MCSs occur on average on 6 July. Short lifespan MCSs lasted started, on average, at 0025 UTC and ended at 0942 UTC, medium began, on average, at 2342 UTC and ended at 1136 UTC while long lasting MCS began at 2224 UTC and ended at 1312 UTC.

Fig. 2.7 shows the total precipitation rate across the tracked MCS object by length of MCS life span. Generally, the longer the lifespan of the MCS, the later and larger the peak total rain rate. The peak total rain rate is found at 5-7, 7-8 and 10-12 hours after being picked up by the tracking algorithm for short, medium and long MCS respectively. After the time of peak total rain rate, medium and long life span MCSs face a gradual decline between 4-7 hours, while short lifespan MCSs decline more rapidly before not meeting the criteria of the tracking algorithm, in 1-3 hours. Likewise, the peak total rain rate falls between 6000-9000, 8000-13000 and 12000-18000 mm /hr for short, medium and long MCS respectively.

2.3. Differences in Storm Environment for Different Length MCSs

To examine the differences in environment for varying length MCSs, the North American Regional Reanalysis is used. The NARR is sampled at the nearest neighbor to the CoM point three hours prior to the MCS occupying the point (i.e., the NARR data is sampled at 1800 UTC CoM point at 2100UTC) to examine the state of the environment into which the MCS is moving. Fig. 2.8 shows the evolution of mixed layer convective available potential energy (MLCAPE), mixed layer convective inhibition (MLCIN), precipitable water (PW) and 0-6km wind shear in (a) through (d) respectively. Plots are made of the mean of the variable through the shortest length MCS in each category (through 9, 12 and 15 hours for short, medium and long lifespan MCSs). For MLCAPE, both short and medium lifespan MCS begin in higher CAPE environments, with values over 700 J/kg, while long lifespan MCS begin at 600 J/kg on average. Through the next four hours, the MLCAPE into which the short and long life MCS increase at just over 100 J/kg per hour while the MLCAPE ahead of the medium lifespan MCSs grows at a slower rate and is passed by the long life MCS. Through the last hours of the short life span MCSs, the increase in CAPE slows then shrinks in the last hour, attained the maximum value of 1300 J/kg at hour seven. The medium lifespan MCSs sees the MLCAPE into which it is moving flatten out from hour 5 onward at roughly 1100 J/kg.

In Fig. 2.8b, the same graph is shown, but this time for MLCIN. At the start of the tracking of the MCS, the long life MCSs show the least inhibition (39 J/kg), with medium second (46 J/kg) and short with the most inhibition (58 J/kg). Through the lifetimes of each mean system, the inhibition generally increases with time. For long life span MCSs, the inhibition decreases into the second hour to 34 J/kg, then increases slowly into hour 4 to 40 J/kg, after which the inhibition increases rapidly into hour 11 at a rate of about 6 J/kg per hour to 80 J/kg.

For the remainder, the MLCIN shows minor increases and decreases to end at -78 J/kg. Medium lifespan MCS show a steady increase in inhibition through hour 9, also at about 6 J/kg per hour, after which the MLCIN shows little change. Short lived MCSs show a decrease in inhibition through the first 3 hours to -52 J/kg, then a steady increase, though at a slower rate than medium and long lived MCSs to -78 J/kg in the final hour with no levelling off of values as in long and medium lived MCSs.

Fig. 2.8c shows the trend for PW in the environment preceding the MCS. The graphs shows that the PW surrounding the MCSs is very similar no matter the lifespan of the system, with short and medium life span MCSs starting at 20.7 mm and long life span starting at 20.1 mm. The PW increases at nearly an identical, linear rate for all lengths of MCS through hour 6, after which the PW preceding medium and short length MCSs slows. At hour 7 all types have PW of 34 mm, the value short length MCSs end. Medium length MCSs end at 37 mm after oscillating through the last three hours. After hour 9 the rate of increase of long length MCSs slows with an end value of 41.4 mm.

Fig. 2.8d shows the 0-6km shear trends for each MCS length. The trend of shear is most similar to the trend of MLCIN, with long length MCSs having the most favorable shear environment preceding the MCS than short and medium length MCSs. Also similar to MLCIN is the decrease in favorability ahead of the MCS, no matter the length, through time. Starting values are 9.7, 9.2 and 8.8 m/s respectively for long, short and medium length MCSs. Long length MCSs see a slow, oscillating decrease until hour 7, with a value of 8.5 m/s. From hour 7 through 10 the value falls rapidly to 6.8 m/s, with a slow decrease through hour 13 to 6.4 m/s then an increase to a final value of 7.0 m/s. Medium and short length MCSs see a similar pattern, but with shorter periods of slow decrease at the start (two and five hours respectively for short and medium length, versus 7 hours for long length MCSs) after which is a rapid decrease in favorable shear conditions to final values of 6.9 and 6.4 for short and medium length MCSs.

Fig. 2.9 shows similar graphs to Fig. 2.8 for 250 hPa wind speed, 700 hPa vertical velocity, 850 hPa and turbulent kinetic energy (TKE). For 250 hPa wind speed (Fig. 2.9a), all lengths of MCS show a similar pattern with slow decrease in speed through the first 4-5 hours ahead of the MCS, then more rapid, nearly linear decrease in speed through the rest of the MCS life. This variable shows the most direct correlation to MCS lifespan, with the greatest value in long life, medium lifespan in the middle and the lowest value in short life MCSs.

Mid-level vertical velocity (Fig. 2.9b) with respect to pressure level shows no distinct pattern through time relatable to MCS life span. Values begin nearly identical then decrease rapidly through hour 4. Between hours 4 and 8 the values stay steady but oscillate for short and medium life span MCSs and increase (less favorable) for long life MCS. Values then decease through the remaining hours for long life MCSs.

TKE (Fig. 2.9c) shows a large disparity in pattern between long lifespan and shorter lifespan MCSs. Short and medium lifespan MCSs have nearly identical patterns through time, with a slight increase in values from 1.5 to 2.0 through the first 3-4 hours then a gradual decline below 0.5. While the pattern is similar for long life MCSs, the values increase much faster in the first hours ahead of the MCS to 2.75 at hour 2, but then trail off to nearly the same value as medium length MCS by hour 8.

PBL height (Fig. 2.9d) reflects the fact that the longest lived MCSs form earlier in the day and move through deepening PBLs through the first hours of existence. The longest lived MCS begin in PBLs just over 3000 m, and PBLs ahead of the MCS grow to a maximum of just over 3500m at three hours after formation, with PBL heights decreasing rapidly at hours five through eight. Similarly, medium length MCSs reach a peak PBL height of near 3400 m one hour after formation, with a rapid decrease in PBL height through hour eight after formation, though not as rapid a decrease as the long lived MCSs. Short lived MCSs begin at the highest PBL height in the storm history and decrease afterwards.

Similar to the analysis above, the state of the land surface is assessed along the track of each MCS and analyzed with respect to the length of the MCS lifespan. Soil moisture (SM) is obtained from the NLDAS 0-10 cm liquid water content from the Noah land surface model offline integration. The SM is sampled at 1200 UTC under the assumption that no significant precipitation occurs between 1200 UTC and the time of the MCS. For vegetation, the MODIS Enhanced Vegetation Index (EVI) 16-day product is utilized. The following analysis is conducted on an approximately 100 by 100 km box (4 by 4 and 100 by 100 grid points for NLDAS and MODIS data respectively) centered on the MCS center of mass. Fig. 2.10 shows the results for vegetation (a) and SM (b). For vegetation, the trend is for the MCS to move into greater and greater anomalous vegetation for all lengths of MCS. Long and short length MCS begin with nearly identical values through the first three hours, with the values tailing off for short length MCS in the remaining hours. Medium length MCS move over the greatest anomaly of vegetation through the 10 hours, then see a sharp drop off in values for the remaining two hours. Similarly, long length MCS move over increasing values of vegetation anomaly, then decrease in the final hour.

For SM, the relationship through time and for different length MCS is more complex than for vegetation. For all MCS lengths and times, the mean value of SM anomaly is positive. For short length MCS, values oscillate through time, but change very little from an initial value of 0.5. Through the first 7 hours, the mean SM experienced by medium and long length MCS is nearly identical with beginning values of 0.08 and 0.29 kg/m^3 respectively. Values then increase steadily along the track to near 1.5 kg/m^3 by hour seven. From here, the pattern is very different, with medium length MCS experiencing lower anomaly of SM with each hour to a final value of 0.25 kg/m3 by hour 11. Long length MCS experience steady values of SM through hour 12, then increase sharply to a final value of 2.1 kg/m3.

Different size boxes were used (not shown) and the results showed little sensitivity to the area over which the anomaly was measured. There was no statistical significance found between the distributions of SM between the three length categories of MCS for any size area. For vegetation, the greatest statistical significance was found for 64 by 64 km box centered on the MCS CoM, with statistical significance found for the first three hours between medium and short and medium and long length MCS to the 95% level using the Mann-Whitney U test.

2.4. Analysis of MCSs by Region of Initiation

Six primary regions of convection initiation were determined: Southern Wyoming (SWY), Northern Colorado (NCO), Central Colorado (CCO), Southern Colorado (SCO), Northern New Mexico (NNM) and Central New Mexico (CNM). Often, there was ambiguity from which primary region an MCS initiated. Five secondary regions were established, each being a combination of two or more of the primary regions: SWY/NCO (SWY+NCO), CO (All CO primary regions), SCO/NNM (SCO+NNM), CO/NM (all CO and NM primary regions) and NM (NNM+CNM). Fig. 2.11 shows the 11 regions of convection initiation as well as the number of MCSs initiated from each region.

To examine the regional characteristics of these storm systems, three regional MCS composites are developed: Wyoming (WY, using SWY, 13 cases and SWY/NCO, 15 cases for a total of 28 cases in the composite, Colorado (CO, using the CO region, 18 cases) and New Mexico (NM, using the NM, NNM and CNM regions, for a total of 25 cases). These regions were selected due to knowledge from previous studies on favorable areas for convection in high terrain, e.g., the east-to-west ridges in the high plains in each of the three regions (the Cheyenne Ridge in Southern WY, the Palmer Divide in CO and the Raton Mesa in NM) as well as a comparable number of cases for each geographic region.

Composited mean Stage IV hourly precipitation rate for the WY, CO and NM cases are shown in Fig. 2.12 for 2100, 0300 and 0900 UTC. At 2100 UTC, higher mean precipitation rates are found in the higher terrain of the Cheyenne Ridge and the Raton Mesa in the WY and NM case respectively. The more widespread mean precipitation field in the CO case at higher elevations is consistent with the fact that the CO case consists of precipitation events in which the specific region of convection initiation was ambiguous, where the WY and NM composites consist of cases focused on specific regions. At 0300 UTC the mean field shows a widespread area of precipitation rates with greater maxima within this area, showing signs of averaging organized convection. The WY and CO case both move easterly out of higher terrain while the NM case moves east-southeasterly into the Texas Panhandle. By 0900 UTC the WY and NM case show a coherent mean signal, with both moving more southeasterly with time. The CO case shows less coherence in the average precipitation rate signal.

The general patterns of 250-hPa and 850-hPa winds are very similar for all cases at both levels, as shown by NARR-based composites (Fig. 2.13). At 250 hPa, the general pattern moves from a mean trough over the Rocky Mountains in the WY case veering to a ridge over the Rocky Mountains in the NM case with the CO in between these two patterns. At 850 hPa the tongue of warm air pushes into the region of convection initiation, with the warm air pushing furthest north in the WY case. The NM case shows the strongest evidence of a low-level baroclinic zone with cooler temperatures and northwesterly winds pushing into Colorado and South Dakota. Compositing NARR surface variables, such as sensible heat flux, latent heat flux, and soil moisture, bore no discernable difference between the three regional MCSs (not shown).

2.5. Summary and Conclusions

A climatology of CONUS MCSs initiated in the high terrain of the Rocky Mountains and the adjacent High Plains, including an analysis of precipitation rate patterns and characteristics of longevity, was developed. The climatology was constructed with Stage IV hourly precipitation rate data using a combination of objective (using image tracking software in the Scipy package of the Python programming language) and subjective (tracking individual cells back to point of origin in radar composites) techniques. This study found and classified, by region of convection initiation, 232 MCSs meeting the criteria. These MCSs were found to provide the most precipitation, by proportion of total warm season precipitation, to the area between 500 and 1300 meters elevation, especially in the northern half of the domain in north eastern Colorado and western Kansas and Nebraska.

An examination of MCSs by longevity revealed that the longest lasting MCSs tend to have longer tracks, initiate further south, and have the greatest north to south movement through time. These tendencies are somewhat explained by the mean dates of occurrence for medium length (12-15 hours) being 4 days later than short length (9-12 hours) and long length MCSs (15-18 hours) being a further 4 days later in the season than medium length MCSs. The mean total precipitation rate by longevity of MCS in hours showed that longer lasting MCSs tended to have later peak total precipitation rate and greater total precipitation rate. Interestingly, over the first three hours along the MCS track, there is no indication of the relationship between greater eventual longevity and precipitation rate, i.e., longer lasting MCSs do not show a tendency, on average, to produce greater precipitation during the first hours of existence versus shorter life span MCSs.

The mean environment into which these MCSs propagate into was examined, utilizing the NARR for atmospheric variables, NLDAS 0-10 cm soil moisture and MODIS derived vegetation. For MLCAPE, all lengths of MCS showed similar trends through the first 7 hours, with increasing values as the mean systems moved east south east into the Plains. From here, short lifespan MCS showed a slight decrease in the final hour, medium length MCSs showed steady values through the remaining times while long length MCS continued to increase rapidly through hour nine then decrease at a rapid linear rate through the remaining hours. MLCIN and 0-6 km wind shear showed nearly identical trends, with all length MCS showing a slow decrease in favorability in the first hours, then a rapid decrease in favorable conditions followed by a steadying of values in the final hours of the mean system, with long length MCSs having more favorable conditions (low inhibition, greater shear) throughout all times. 250 hPa was similar in that the values decreased nearly monotonically for all length categories, with long length MCS always having the greatest value. PW was very similar for all categories of MCS longevity, with all showing increase in values through the lifetimes of the mean systems. 700 hPa vertical velocity showed no distinct relationship between length categories, and only a slight tendency for increasing values through time. TKE at 850 hPa showed a large difference between long length MCS and medium and short, which had nearly identical graphs, while long lived MCSs moved through a growing PBL through the first hours of existence while medium and short lived MCSs saw a decrease in PBL heights after the first hour of existence. Both of these variables reflect the fact that longer lived MCSs form earlier in a more active, in regards to low level turbulence and deepening PBL.

For MODIS derived enhanced vegetation index, all longevity categories showed increasing values through time, meaning that the MCSs tended to move into areas with locally anomalously high vegetation amounts. SM was more complex, with short length MCSs seeing a flat tendency through time, medium length MCSs moving into locally anomalously greater SM through hour seven then decreasing sharply, and long length MCS moving into generally greater SM anomalies through time.

The typical evolution of precipitation through time on days with these type MCSs showed peaks in the precipitation distribution growing through time, from a peak at the highest elevations (1800-2000m) at 2300 UTC to the maximum peak at 0600 UTC at 600-800 meters elevation. The precipitation pattern on all other warm season days showed a large precipitation rate per unit area peak at the highest elevations which then decreased with time then showed an increase with time in the peak precipitation amount in a broad distribution at levels below 800 meters late in the night. As discussed in Carbone and Tuttle (2008) there are three mechanisms for the apparent west-to-east, day to night precipitation signal from the Rockies into the Plains of the CONUS 1) the passage of eastward propagating precipitation systems originating near the Continental Divide 2) reversal of the mountain-plains solenoidal circulation 3) nocturnal maxima and oscillation of the LLJ. It is apparent that mechanism one dominates the pattern through time in the MCS type days while the other two factors play a larger role in the differing pattern for all other days seen in Fig. 2.3.

Three regional subsets of MCSs were made based on area of convection initiation: Wyoming, Colorado and New Mexico. NARR composites of the upper and lower troposphere wind, temperatures and geopotential height fields showed little difference between the three regional types. Composites and analysis of other fields revealed nothing significant between the three regional types with regards to sensitivity to boundary and surface properties, most likely due to the coarse resolution of the NARR data.

This work is heavily utilized in subsequent chapter of this dissertation. The mean conditions of the Wyoming, Colorado and New Mexico MCS types are used to form the initial and boundary conditions of the quasi-idealized numerical modeling experiments in chapter 3. In chapter 4, differences in characteristics of convection initiation are examined using the MCS days and non-MCS days derived in section 2 of this chapter. Future work on this line of research includes utilizing higher fidelity soil moisture data from current satellite platforms, such as SMOS, to enhance the study of land surface interaction with developing, mature and decaying MCSs.

2.6. Figures

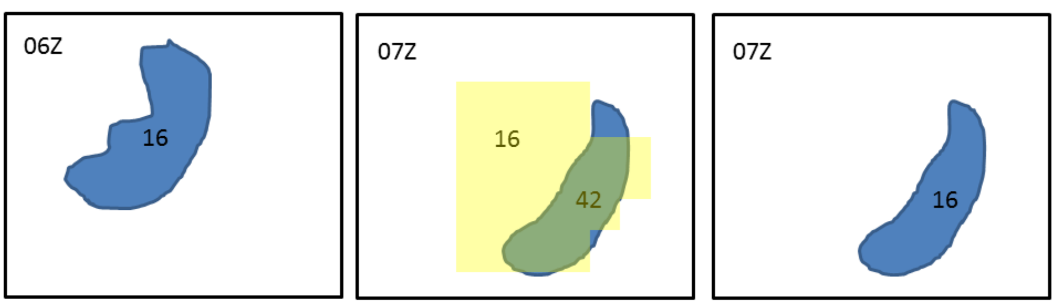

Figure 2.1. Process of labeling and continuity in the precipitation system tracker. At 0600 UTC (left) all systems meeting the size and intensity criteria are assigned a label (16 in this case). At 0700 UTC (center), new, temporary labels are assigned to all CPS meeting the criteria, then a mask based on the climatological movement of CPS is placed over each CPS center of mass to find previous time step CoMs. If found (right), the previous time step label is assigned and the characteristics are recorded in a database through the lifespan of the system.

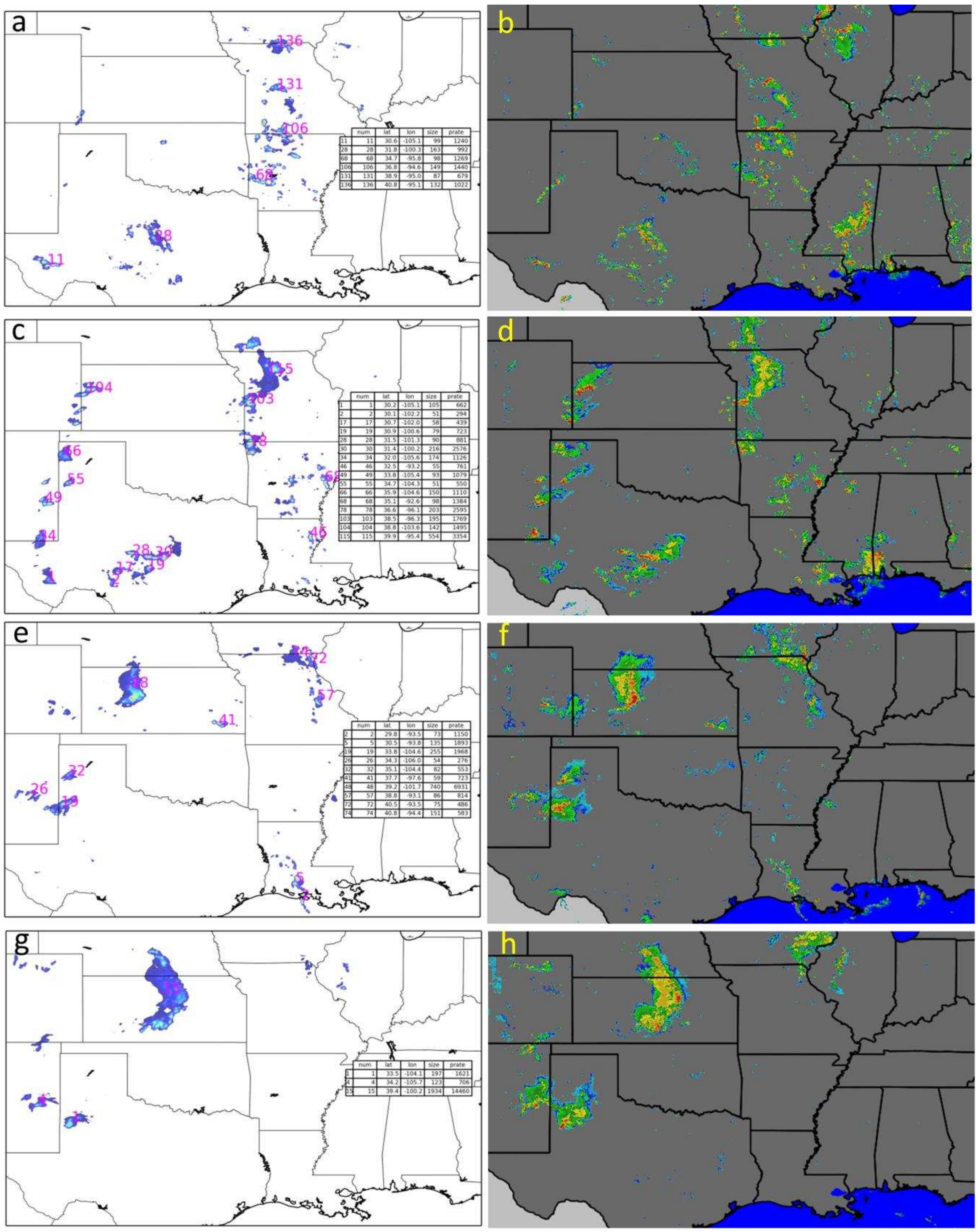

Figure 2.2. Example of the evolution of one MCS from 25-26 May 2010 at 1947 (2000) UTC (a and b), 2125 (2200) UTC (c and d), 2355 (0000) UTC (e and f) and 0355 (0400) UTC (g and h) for each NEXRAD composite image (left) and CPS tracking algorithm output with Stage IV data (right).

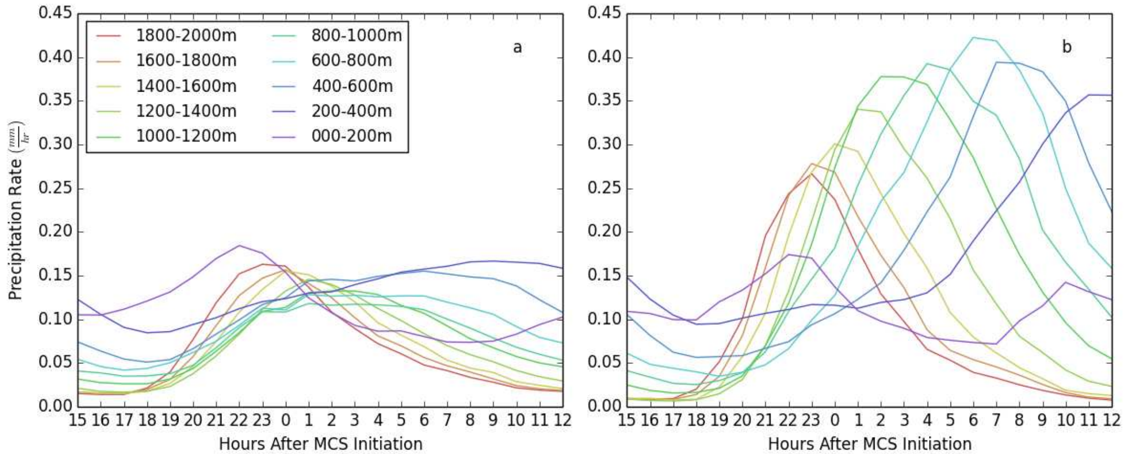

Figure 2.3. Graphs of distributions of area averaged precipitation rate per day for 200 meter elevation bins for all days (left) and days with MCSs (right).

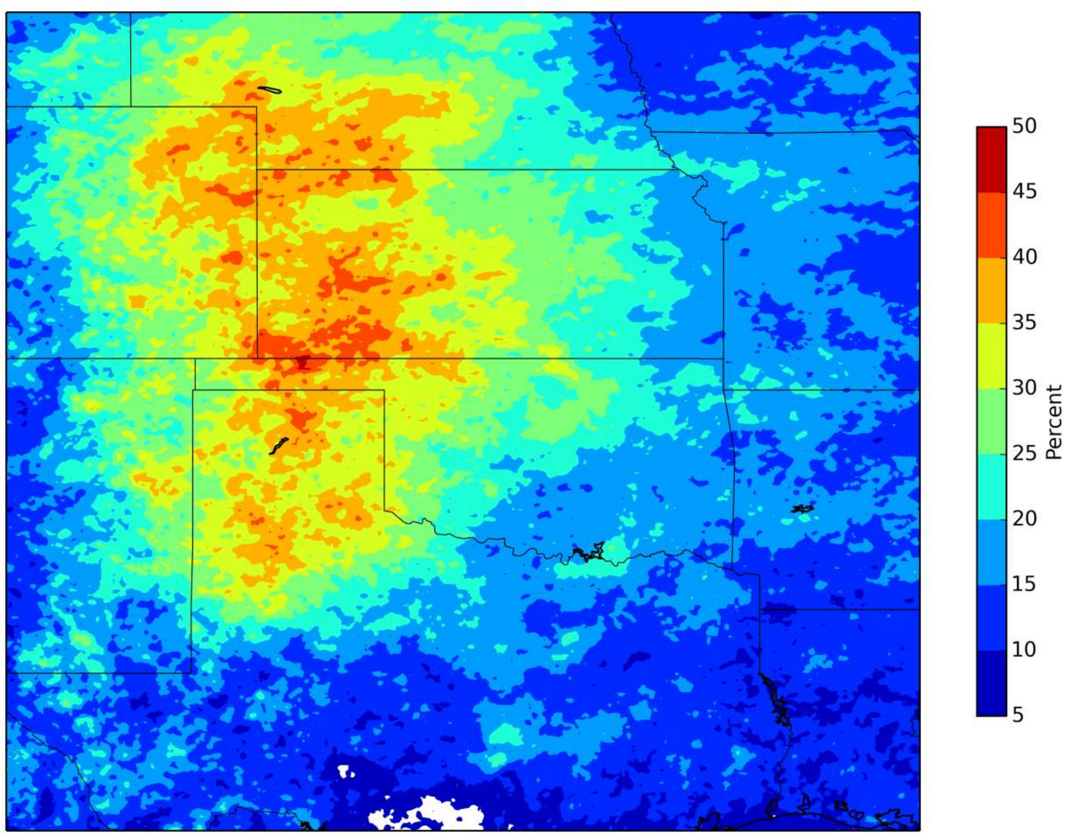

Figure 2.4. Percentage of warm season precipitation from days with high plains born MCS.

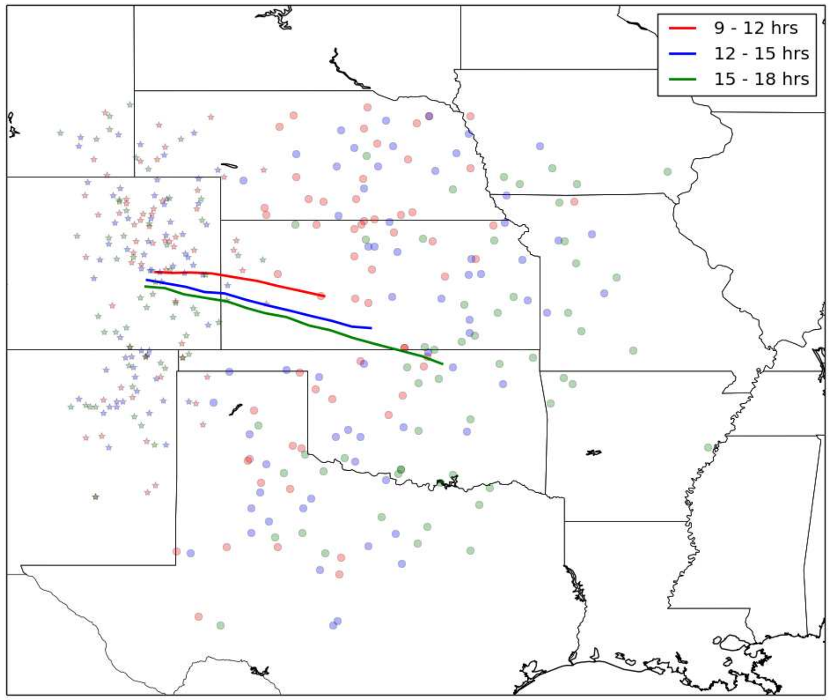

Figure 2.5. Start (star) and endpoints (circle) for all short (blue), medium (green) and long (red) lifespan MCS with mean tracks of each short, medium and long length MCSs.

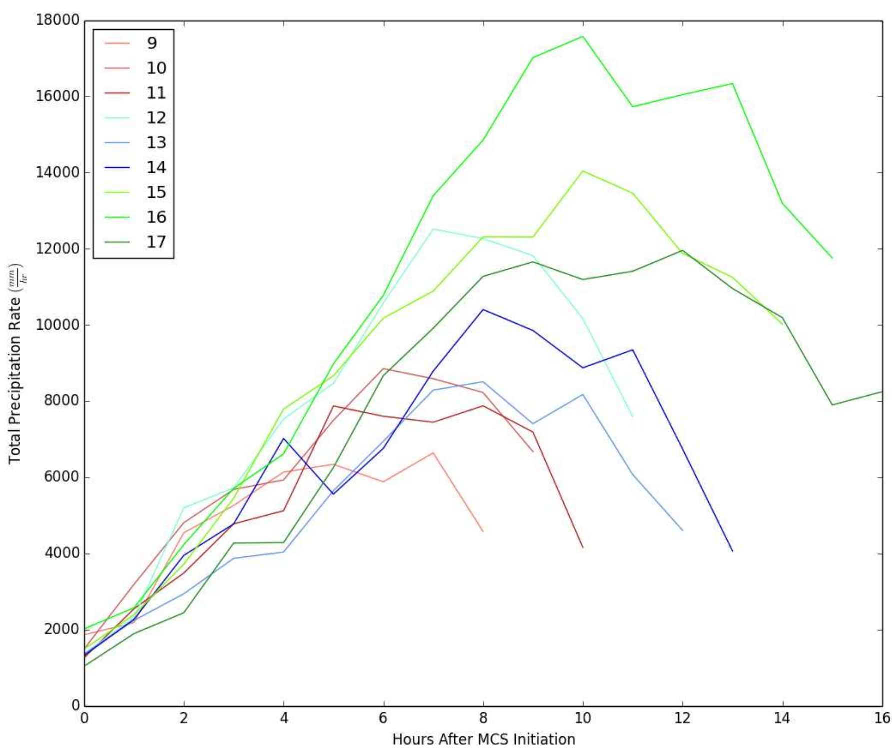

Figure 2.6. Total mean precipitation rate for all systems lasting 9 to 16 hours.

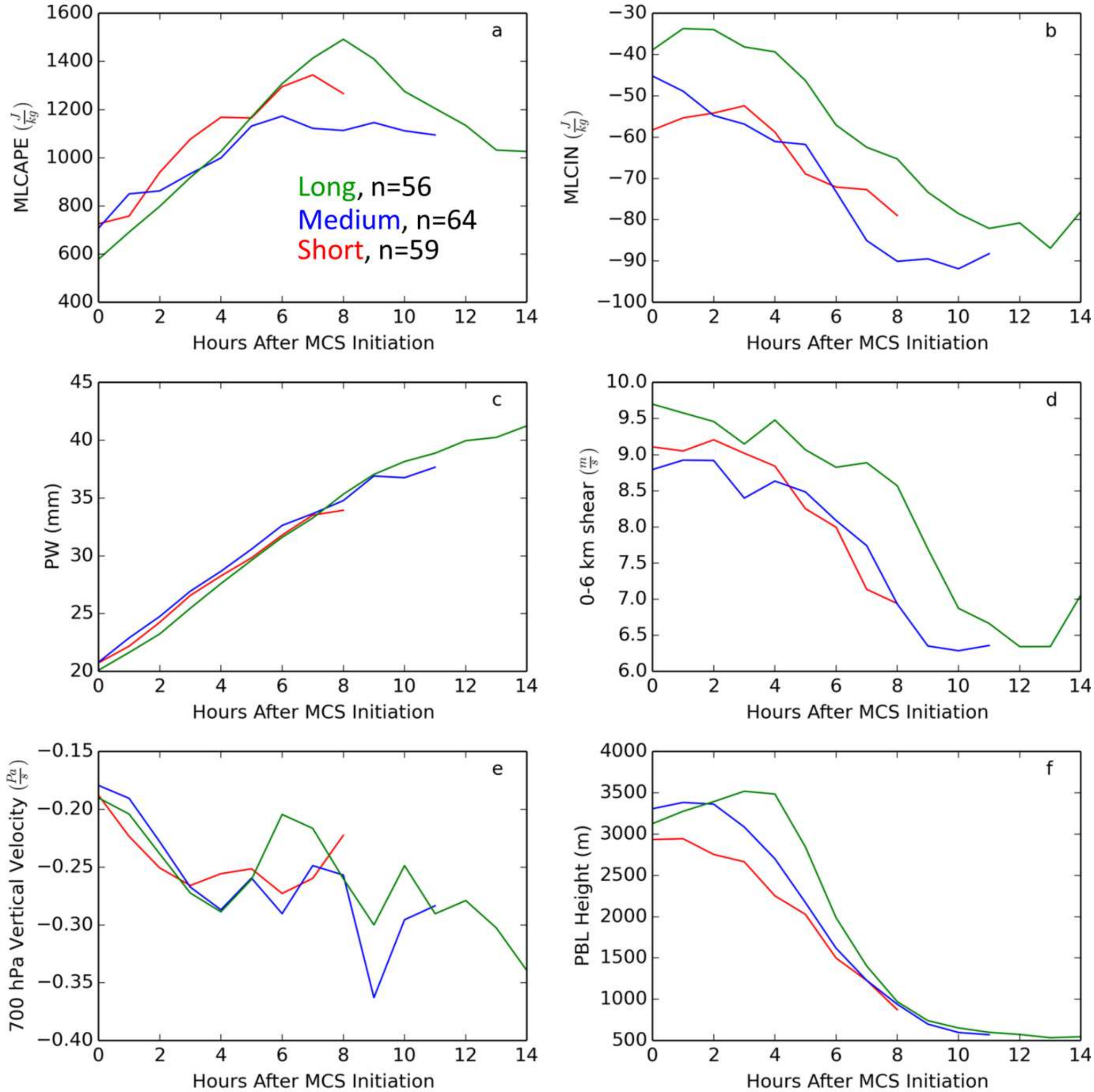

Figure 2.7. Mean variable by hour for all systems lasting 9 to 11 hours (red), 12 to 14 hours (blue) and 15-17 hours (green) for MLCAPE (a), MLCIN (b), PW (c) and 0-6 km shear (d), 700 hPa vertical velocity (e), and PBL height (f).

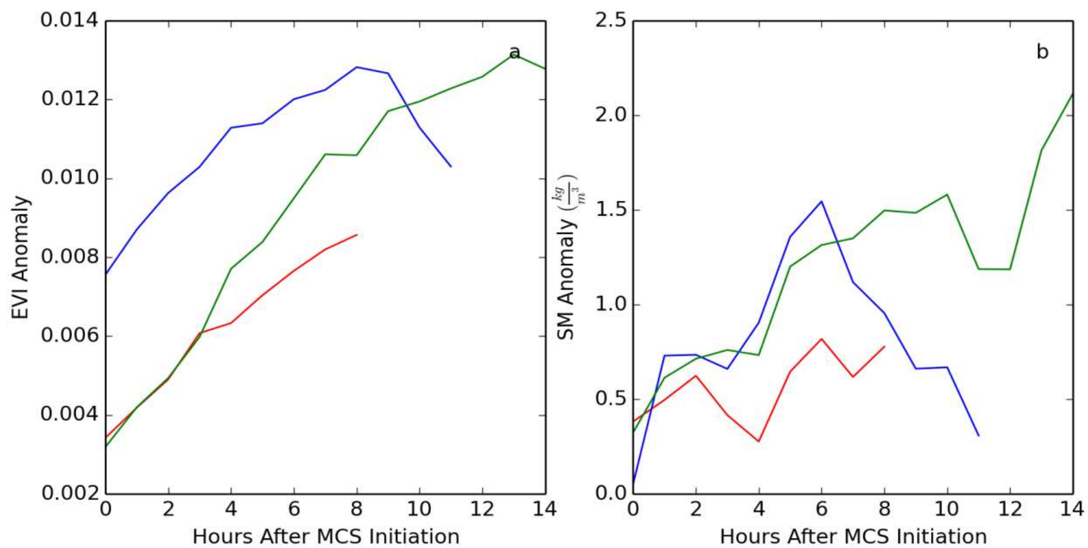

Figure 2.8. Mean variable by hour for all systems lasting 9 to 11 hours (red), 12 to 14 hours (blue) and 15-17 hours (green) for MODIS EVI (a), NLDAS soil moisture (b).

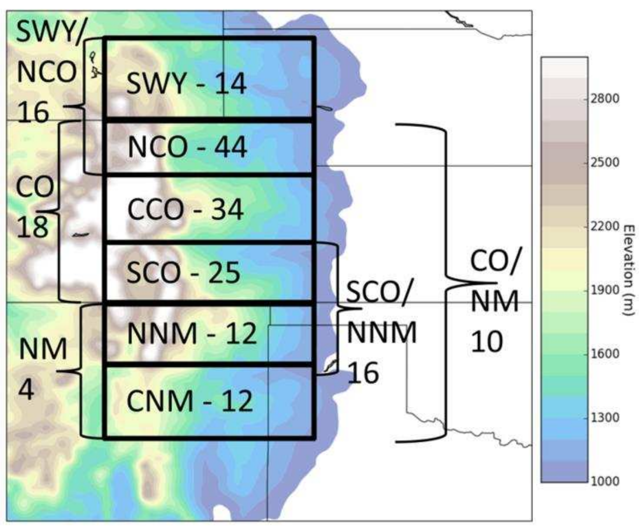

Figure 2.9. All convection initiation regions, including primary regions (boxes) and regions for which ambiguity existed as to which region MCS initiated in (to the right and left of the boxes, with numbers of systems initiated in the regions.

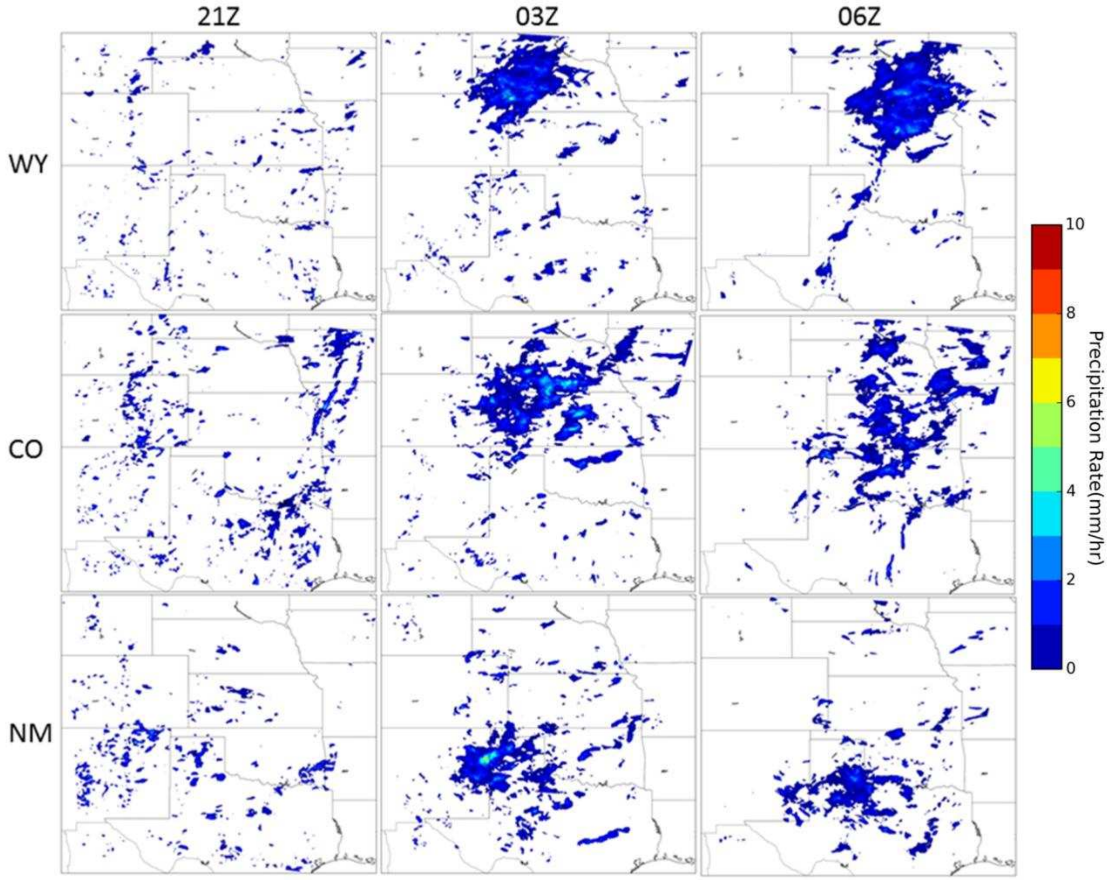

Figure 2.10. Composite of Stage IV precipitation rate by case for Wyoming (top), Colorado (center) and New Mexico (bottom) MCS types at 2100 UTC (left), 0300 UTC (middle) and 0600 UTC (right).

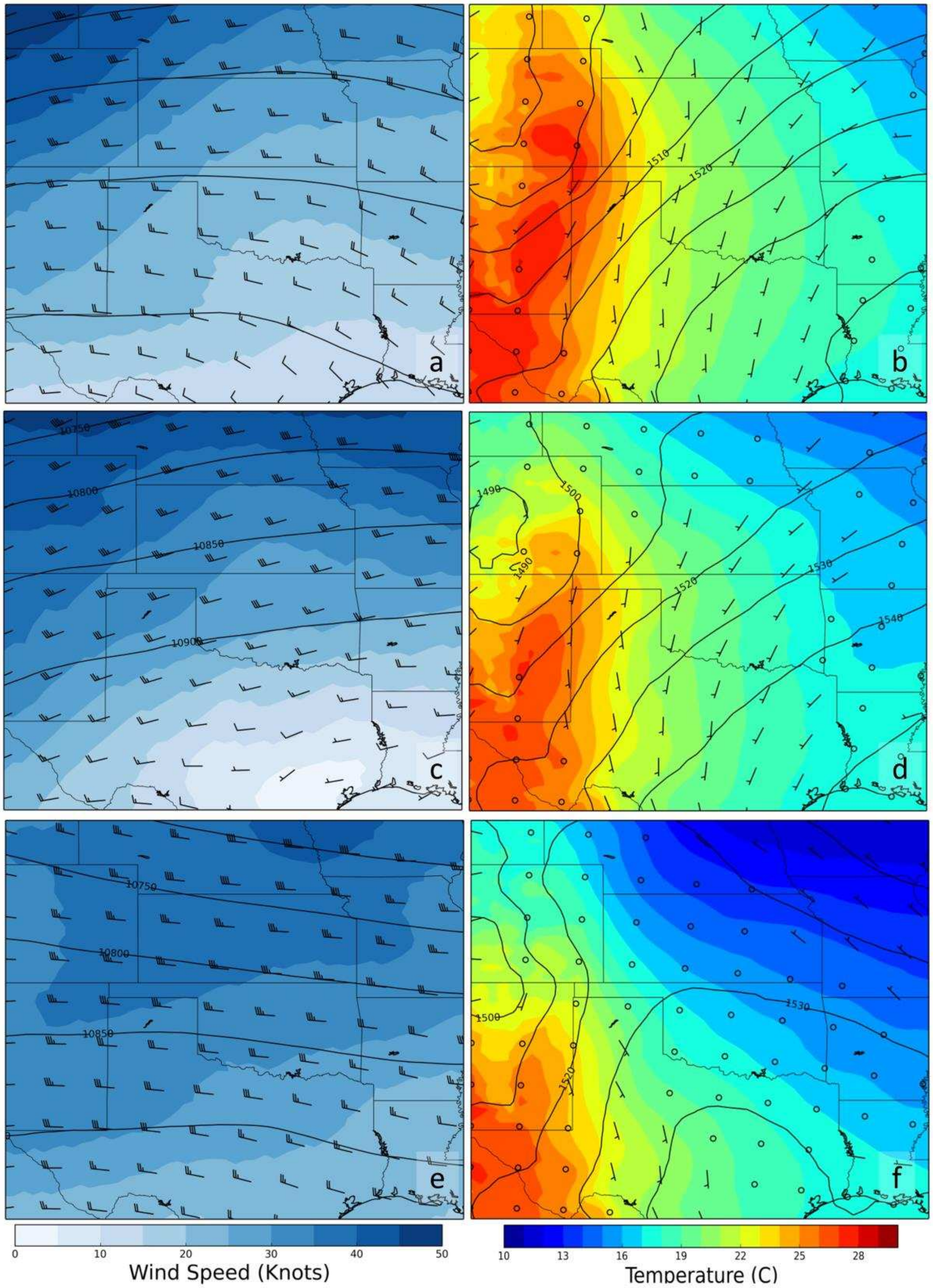

Figure 2.11. NARR composites for Wyoming (top), Colorado (middle) and New Mexico (bottom) MCS cases for 250 hPa (left) geopotential height (black contour), winds (knots) and isotachs (color fill) and 850 hPa (right) winds (knots), temperature (Celsius, color fill) and geopotential height (black contour).

CHAPTER 3

SIMULATED MCS RESPONSE TO AN IDEALIZED SOIL MOISTURE ANOMALIES IN THE HIGH AND LOW PLAINS OF THE US

3.1. Introduction

The state of the land surface plays a major role in determining the state of the planetary boundary layer (PBL) which, in turn influences convective precipitation, from the spatial and time scales of individual cumulus clouds to synoptic spatial scales and climatic timescales. Koster et al. (2004) showed, through an ensemble of global climate models, that “hot spots” exist in the degree to which local soil moisture (SM) variations drive feedbacks to precipitation during the warm season. One such hot spot found was in the US Great Plains (GP). Contrary to this result, Findell and Eltahir (2003), using a combination of indices derived from radiosonde data, found regional differences in the feedback between SM and initiation of deep convection throughout the CONUS finding a positive feedback in the eastern US, a negative feedback in the desert southwest, and transition areas in between, as well as mid- to upper-troposphere controlled feedback in the central Rockies.

On the mesoscale, the bulk of studies on the impact of variations in SM on convection are numerical due to the lack of observations at this scale (Zhou and Geerts 2013). Avissar and Liu (1996) showed that the gradient of SM was important on the mesoscale in developing convection by creating differential sensible and latent heat fluxes leading to differences in temperature and density over moist and dry surfaces, thus creating solenoidal circulations between the contrasting surfaces. Holt et al (2006) conducted a modeling sensitivity study of Southern Plains convection during the IHOP field campaign finding forecast improvement using high resolution

SM data versus typical operational scale data, as well as further improvement using a more advanced land surface model with vegetation and transpiration effects. Erlingis and Barros (2014) conducted a modeling study to examine the importance of land use and SM in relation to the PBL parameterization in forecasting a day-to-night transitioning MCS. They found that, while land use impacted thermodynamic variables, and to a lesser extent shear, the choice of PBL parameterization had a greater impact on the depiction of the pre-storm PBL and subsequent MCS. Hohenneger et al (2009) showed that the grid spacing and the use of convective parameterization in numerical simulations caused a switch between a positive and negative feedback between SM and precipitation.

SM and land surface variability on the meso-alpha (200-2000km) scale can impact the development of larger scale features, such as the nocturnal low-level jet (LLJ). Fast and McCorcle (1990) conducted a sensitivity study of the Plains LLJ using a 2-dimensional model, finding that, while the usual factors attributed to causing the LLJ were key, those being the inertial oscillation and decoupling of the surface layer from LLJ layer above (e.g., Blackadar 1957; Holton 1966), there were key other factors that promoted the phenomenon. One was the turning of ageostrophic flow from east to west caused by differential heating of elevated terrain on the west side of the plains. Another factor was the presence of dry soils, which were found to enhance the LLJ relative to other soil conditions due to enhanced decoupling between the near surface and free atmosphere.

Sensitivity studies of convection to land use at cloud-system-resolving scales extend back to Pielke et al (1997). They found that by varying the land surface in the Texas Panhandle from current use to a uniform short grass, the progression of the dryline is slowed, and sensible heat flux is increased at the expense of water vapor flux and deep convection does not develop in the short grass case. Oberthaler and Markowski (2013) examined the impact of anvil shading on a quasi-linear convective system (QLCS) in an idealized model environment, finding that shading both reduces the buoyancy of low-level parcels entering the updraft as well as exacerbating the impact of low level shear. The lack of anvil shading makes favorable low level shear (favorable in the sense of Rotunno et. al. (1988)) more favorable and vice versa for unfavorable low level shear.

The goal of this study is to assess the sensitivity of MCSs initiating in the northern, central and southern regions of the Rocky Mountains and High Plains to a series of large-scale, idealized SM anomalies; one anomaly in the high plains, in the region of convection initiation and another downstream in the central plains. Section 2 describes the methods used to study the sensitivity of these three regional MCSs to an idealized large-scale SM forcing. Section 3 describes the results of the modeling study and section 4 presents a summary and conclusion.

3.2. Model Configuration

All model simulations were accomplished with the Advanced Research Weather Research and Forecasting Model (WRF; Skamarock et al. 2008) version 3.4.1. A two-domain nested structure was used with the outer and inner domain horizontal grid spacing set to 16 and 4 kilometers respectively with 50 vertical levels on a stretched grid (Fig. 3.1). The 4:1 parent grid ratio is not optimal for operational or long-run simulations, it was chosen for computational efficiency due to the large number of model runs and the relatively short run time of each model run, leading to little influence of lateral boundary conditions on the solution. The interface between the outer and inner nest was one-way (i.e., no feedback from the inner to outer nest). Parameterizations used were the Noah Land Surface Model (Ek et al. 2003), Goddard radiation (Chou and Suarez 1999), Thompson microphysics (Thompson et al, 2008) and Kain-Fritsch cumulus (Kain et al 2004) in only the outer domain and the Mellor-Yamada-Nakanishi-Niino (MYNN) PBL scheme (Nakanishi and Niino, 2006)

The MYNN PBL scheme, specifically the MYNN2 implementation in WRF, is a local scheme with 1.5 order closure. The MYNN scheme was developed as an improvement to the popular Mellor-Yamada-Janjic (MYJ) scheme (Mellor and Yamada (1982) Janjic (1990)) and shows improved performance in stable boundary layers (NN06) as well as in developing deep, warm season boundary layers (Coniglio et. al. 2013) over prior local PBL schemes. Simulations were also accomplished with the Yonsei University (YSU) PBL scheme (Hong et al. 2006) to rule out sensitivity to the PBL scheme used and to examine the difference in MCS and MCS environment resulting from the change in scheme. The YSU scheme, based on the Troen and Mahrt (1986) concept of incorporating a countergradient correction term into downgradient diffusion expressed solely by local mixing, includes more recent innovations such as better accounting of entrainment at the top of the PBL. With the advantage of being computationally efficient compared to local PBL schemes, the YSU scheme does over deepen PBLs, resulting in a dry bias near the surface and lowering the mixed layer convective available potential energy (Coniglio et al. 2013).

All lateral boundary conditions for the outer nest and all initial conditions were derived from the North American Regional Reanalysis (NARR: Mesinger et al. 2006). Simulations for three regional MCS regions were conducted: Wyoming (SWY and SWY/NCO cases from the observational study above, 28 cases), Colorado (CO, 18 cases) and New Mexico (NM, CNM and NNM, 22 cases). For each of the three regional experiments the NARR data for all cases from the respective observational study were composited to create the initial and lateral boundary conditions, similar to techniques used to study MCSs as in Coniglio and Stensrud (2001) and

Peters and Schumacher (2015). For each individual case comprising the composite, the full NARR Gridded Binary file for 1500 through 1200 UTC, every three hours, were processed by the WRF Preprocessing System. The processed files were then composited using the netCDF operator software to create the composited files which was then initialized by WRF software (real.exe) to create a single set of initial and boundary conditions.

For each of the three regional MCS initiation regions in the study, eight simulations were conducted: 1) unaltered lower boundary condition (UNALTERED), IC is not altered in any way from that derived from the NARR composites 2) dry to moist soil (D2M), SM is prescribed in an idealized pattern shown in Fig. 3.2 between a minima of 10% by volume in the high plains of CO to a maximum in the GP of 40%) moist to dry soil (M2D), SM is prescribed in an idealized pattern shown in Fig. 3.2 but the "polarity" switched between a maximum of 40% by volume in the high plains of CO to a minimum in the GP of 10%. Soil type and land use are made uniform in the D2M and M2D experiments, set to clay loam soil and grassland land use. The soil anomalies were chosen to be large enough to span the three regions under study in order to examine the varying impact on MCS lifecycle from a single, large-scale SM anomaly. The magnitude of the wet soil anomaly was chosen based on the wettest soil anomaly from the NARR input data, as an upper bound expected in the region. The dry soil anomaly was chosen based on sensitivity experiments, as the driest large-scale SM anomaly permitted while disallowing spurious deep, moist convection inconsistent with the UNALTERED solution. These four experiments were conducted were conducted for each region, for a total of 12 simulations. All simulations were conducted from 1500 UTC through 1200 UTC the next day. For purposes of radiation, the median of the composited dates was used for each of the three regions. A summary of the setup for all simulations is shown in Table 2. All results discussed in the results section are from the inner domain (4km horizontal grid spacing).

3.3. Model Simulation Results

3.3.a. UNALTERED Simulation Results

First examining the UNALTERED model runs, Fig. 3.3 shows the simulated composite reflectivity at 2000, 0000, 0400 and 0800 UTC for WY in (a) through (d), CO in (e) through (h) and NM in (i) through (l). At 2000 UTC, for all regions, convection initiation (CI) occurs throughout the Rocky Mountains of CO. The WY case exhibits the strongest convection in northern CO and southern WY at 2000 UTC (Fig. 3.3a). By 0000 UTC it (Fig. 3.3b) shows the greatest amount of organization with a squall line beginning to form in the panhandle of Nebraska. At 0400 UTC, the trends from 0000 UTC persist with the WY case showing the greatest organization as a quasi-linear (QL) MCS moves through central NE with numerous embedded cells exceeding 65 dBZ (Fig. 3.3c). By the final panel (Fig. 3.3d), the MCS shows signs of weakening, with fewer cells exceeding 65dBZ and a less solid, leading QL MCS.

The CO begins (Fig. 3.3e) with the widest spread CI in the Rocky Mountains of the three regions, as well as cells initiating to the east in NE CO and western Nebraska. In the CO (Fig. 3.3f) case, convective activity continues to be the most widespread of the three regions, with intense, in terms of simulated reflectivity, cells building into western KS at 0000 UTC. CO emerges from having the most widespread convection to having the largest MCS at 0400 UTC, but with fewer intense cells than the WY case at this time (Fig. 3.3g). At 0800 UTC (Fig. 3.3h) the MCS grows in areal extent and in the stratiform region.

The NM case shows the least amount of CI, and shows no more CI in NM than the other two regional cases at the start (Fig. 3.3i). At 0000 UTC (Fig. 3.3j), the initial convective activity on the Raton Mesa from 2000 UTC is transitioning to an MCS while widespread, intense (> 60 dBZ) convection initiates throughout the TX Panhandle ahead of the initial CI to the west. At 0400 (Fig. 3.3k) there appears to be two separate MCSs, one persisting from the CI on the Raton Mesa and one formed ahead in the TX Panhandle. By 0800 (Fig. 3.3l) the two separate MCSs have merged into a single MCS, shows signs of a “bow and arrow" structure described by Keene and Schumacher (2013) with large amounts of convective activity trailing the leading QL portion of the MCS.

To examine the frequency, intensity and size of convective cells across the three regional model experiments, Fig. 3.4 shows the count (bar graph) and mean size (line graph) of convective cells with updraft speeds of 5 (Fig. 3.4a) and 10 (Fig. 3.4b) m/s at 500 hPa. Individual convective cells were determined using image processing software of the Scipy library of the Python programming language. The software identified cells by finding contiguous grid points of at least 5 and 10 m/s vertical velocity at 500 hPa respectively, keeping in mind previous studies that have shown that the size of individual convective cells adapt to the grid spacing, growing larger at, say, 4 km grid spacing versus 250 km grid spacing (Bryan and Morrison 2012)

Looking first at Fig. 3.4a, using cells with contiguous regions of at least 5 m/s as a proxy for examining the characteristics of all convective cells, while the WY case begins with the greatest cell count and cell size at 2000 UTC, it is quickly surpassed by CO at 2200 UTC, which maintains the lead through the period of initial cell growth through 0200 UTC. Early on, all cases show an increase in individual cell size, beginning with cells averaging two grid points at

2000 UTC (32 km^2) with all growing to mean cell size of more than 4 grid points (64 km^2) by 0300 UTC. After 0300 UTC, roughly the time the MCSs reach maturity, the mean cell size drops, most rapidly in the NM case and least in the WY case. All three cases follow roughly the same pattern to cell count with an increase to a peak near 0000 UTC due to cells forming from daytime heating, a lull between daytime heating and MCS maturity between 0000 and 0400 UTC and a growth in cell count through 0800 UTC as the MCS grows in size and intensity.

Fig. 3.4b, showing the count and size of cells with contiguous regions of 10 m/s vertical velocity updrafts to examine only intense convective cells, a different pattern emerges compared to Fig. 3.4a. The mean size of intense convective cells is nearly constant throughout at about two grid points (32 km^2), though there is a slight increase until 0300 UTC and a decrease after, but not nearly the amplitude seen in Fig. 3.4a. While the plot for all convective cell counts (Fig. 3.4a) saw a consistent temporal pattern for all regions, for intense cells, NM climbed to between 10 and 20 cells by 2300 UTC and remained steady through the remainder of the model run. CO and WY on the other hand saw a steady increase in the number of intense convective cells until 0600 UTC then a slight drop to the end of the model run with slightly higher count in the CO case on average.

Figs. 3.5 and 3.6 show the spatial distribution of most unstable CAPE (Fig. 3.5) and precipitable water (PW) and 0-6 km wind shear (Fig. 3.6). For CAPE, at 2000 UTC all three regional cases show a westward extension of higher CAPE values into the higher terrain in the area of MCS formation (Figs. 3.5a,e and i). By 0000 UTC, WY (Fig. 3.5b) shows in increase in CAPE across Nebraska, while values stay similar in the CO and NM cases (Figs. 3.5f and j). Through the remainder, there is little change in the CAPE ahead of the system, with the highest values in each case remaining ahead of the system. The NM case sees CAPE increases ahead of the system, in central and eastern TX, as moist low level air is pulled northward out of the Gulf of Mexico late in the model run.

The PW Field (color fill, Fig. 3.6) shows similar results to the CAPE field in Fig. 3.5, with WY and CO showing very similar patterns through time with high values throughout the length of the GP ahead of the system moving out of high terrain. NM has lower values of PW from Kansas northward, but high values in the southern GP. All three regional cases show comparable values from 2000 to 0400 UTC then an increase in PW values ahead and to the south of the MCS. For 0-6km wind shear, from 2000 to 0400 UTC, CO and WY show consistent values of 15 m/s and greater ahead of the MCS. By 0800 the values ahead of the CO MCS (Fig. 3.6h) show a decrease to near 10 m/s. For the NM case, while the initial convective cells are born in shear greater than 15 m/s in NM and TX, the MCS moves into steadily lower shear values into central and eastern TX by 0800 UTC (Fig. 3.6l).

Fig. 3.7 shows a graph of the most unstable CAPE (bar) and CIN at the most unstable parcel level (line) at 50 to 100 km ahead of the MCS, centered on the MCS in the north south direction. For 2000 and 2200 UTC, when individual convective cells are forming, the environment is not inhibited and CAPE values are comparable across the regions. As the MCSs form and mature from 0000 to 0600 UTC, the trends vary by region, increasing ahead of the WY system hour by hour to over 2000 J/kg, decreasing then steadying to 1300 J/kg in the CO case and holding steady at roughly 900 J/kg in the NM case. CIN values increase the greatest in the CO case and the slowest in the NM case. At 0800 and 1000 UTC, CAPE values jump sharply in the NM case as the system encounters more unstable air in vicinity of the GOM.

Fig. 3.8 shows the PW (bar graph) and 0-6km wind shear (line graph) for values 50 to 100 km ahead of the MCS, centered in the north south direction. PW values steadily climb ahead of each MCS, though most dramatically in the WY case, which begins with the lowest PW, below 25 mm, but rises to over 40 mm by 0800 UTC. Inversely, shear values fall steadily ahead of each MCS, above 15 m/s for all cases at 0000 UTC, but falling steadily to below 9 m/s by 1000 UTC, with CO consistently experiencing greatest shear values and NM the lowest, on average.

Area-summed precipitation totals for each region is shown in Fig. 3.9. The area-wide precipitation rate in the CO case grows rapidly after convection initiates due this case having the most widespread CI and single-cell convection early on. Domain-wide precipitation rate slows going into night as convection organizes, speeds again as the MCS reaches organization and decreases near morning as the MCS begins to lose organization. The NM case also sees rapid growth of precipitation throughout the domain early, mostly not associated with MCS activity. As the small scale MCS moves into TX and the larger scale MCS forms around 0400 UTC, the precipitation rates are fairly steady through the rest of the time period as the MCS moves to the SE. The WY case sees the slowest growth of precipitation rate near the initiation region due to the least widespread convection early on of the three cases. Through time though, the WY case forms the most organized MCS early, around 0100 UTC and sees steady precipitation rate growth through the model simulation.

3.3.b. Idealized SM Simulation Results

This section examines the results of the model experiments using the MYNN PBL scheme, comparing the results of the D2M versus the M2D model runs. Fig. 3.10 shows the 35 dBZ isopleth for D2M (red) and M2D (blue) for 2000-0800 UTC in 4-hr intervals. At 2000 UTC, CI occurs further east in the D2M case for all regions, and further south in the NM (Fig.

3.10i) case than in the M2D experiment. This trend continues at 0000 UTC as individual cells begin to transition to MCSs further east in the D2M model runs. In the M2D experiments, signs of late, more widespread CI are apparent in the central GP in the CO and NM case. At 0400 UTC, only in the WY case is the systems still further east in the D2M run, with CO and NM at roughly the same position eastward due to the system moving out of the Rocky Mountains merging with developing MCSs from CI in the central GP at 0400 UTC. By 0800 UTC, the southern flank of the MCS in the D2M model runs has progressed further south and east in the CO and NM cases, while the WY D2M MCS continues to be further east of the M2D MCS and has taken on a more southwest to northeast orientation than that found in the M2D model run.

Fig. 3.11 shows Hovmöller diagrams for all D2M (left column) and M2D (right column). CO (Fig. 3.11c) and WY (Fig. 3.11a) show similarities in D2M having a distinct, rapidly moving precipitation signal associated with the MCS beginning at about -104W, just east of the longitude of Denver, CO, at 0100 to 0200 UTC and progressing eastward at a consistent pace with consistent amounts of precipitation through time. For M2D, both show a pattern of subdued precipitation west of the CO/KS border (-102 W) and before 0500 UTC, then an increase in precipitation associated with the MCS, more dramatic in the WY case (Fig. 3.11b). For all three regions, the D2M case shows more focused, greater precipitation amounts than the M2D case associated with pre-MCS and transition precipitation prior to 0200 UTC and west of -102 W. Likewise, the CO and NM cases show precipitation over a greater east-west extent after 0200, or after the time of MCS formation. Fig. 3.11 shows that the main source of the increased precipitation being convection ahead of the MCS in the CO case and increased convective activity ahead and behind the main line in the form of increased stratiform region precipitation in the NM case.

Examining a graph of MU CAPE and CIN at the MU level (Fig. 3.12), similar to Fig. 3.7, but here is the difference of D2M minus M2D, we see generally more favorable conditions in the D2M model run, with higher CAPE values for all regions after 2000 UTC and less inhibition, especially after 0000 UTC. At 0200 UTC, inhibition over the anomalously dry central plains in the M2D run jumps rapidly in early evening in all regions but highest in CO. This is followed by a period of lower inhibition in the M2D experiment for all regions, then higher inhibition into the end of the model run. While the CAPE difference is positive after 2000 UTC (e.g., higher CAPE values in the D2M experiment), it reaches a peak at 0200 to 0400 UTC, as the MCS is traversing the maximum difference in the SM anomaly. The difference decreases into the end of the model run, with the least difference, less than 100 J/kg in the NM experiment.

For the difference in PW and 0-6 km shear (Fig. 3.13), the difference is PW is similar to the difference in CAPE in Fig. 3.12. Here, the PW difference is nearly all negative prior to 00Z, with higher PW over the moist anomaly in the high plains. The differences are all positive from 0000 to 0600, but the difference is far greater in the WY case. By 0800, the difference is small for all regions, with NM showing a negative difference or higher PW in the M2D run. The difference in deep layer shear begins with positive values from 2200 to 0000 UTC, with a large increase in the WY region to over 8 m/s by 0000 UTC. From here, shear values for WY and CO decrease to a minimum at 0400 and 0600 UTC respectively at difference values roughly -4 m/s. NM on the other hand, after a negative value at 0200 UTC continues with positive values at 0400 and 0600 UTC before values decrease below zero at the end of the model run.

The difference in shear between the different idealized SM distributions is explained by difference in the density of low-level atmosphere, driven by differing heat fluxes over the SM anomaly. That is, anomalously dry soils experience greater sensible heat flux, higher low-level temperatures and lower density low-level air (vice versa for moist soils). Fig. 3.14 shows the difference in surface pressure (bar graph) averaged over a 48 by 48 km box in southern Oklahoma (as close to the center of the GP SM anomaly without contamination from convection in any of the three regional experiments). We see that the pressure difference is positive, or higher pressure over the moist soil anomaly of the D2M experiment, throughout the time period and is a fairly consistent difference across all three regional experiments. The line graphs display the difference in zonal wind at 500m above the surface in central TX (32N, -97W, solid line) and in south eastern Kansas (38N and -95W, dashed line), both points not contaminated by convection and on the southern and eastern edge of the imposed GP SM anomaly. The results point to cyclonic (anticyclonic) wind anomaly around anomalously dry (wet) soils in the GP. The strength of the wind anomaly increases through time in the nighttime hours, especially in the meridional component on the eastern edge of the SM anomaly. This explains the difference in 0-6km shear seen between the CO and WY, which saw decreased shear in the D2M case, and NM which saw in increase in shear in the D2M relative to the M2D case.

Examining the precipitation rates over the domain for each of the three idealized experiments in Fig. 3.15, we see in all cases, but especially the WY and CO cases, that the D2M experiment precipitation rate accelerates rapidly early in the evening with M2D lagging. Between 0000 and 0200 UTC, when transition to MCSs occurs, the total precipitation rate in the D2M case slows relative to M2D. In the CO and NM case, as pointed out in Fig. 3.10, more widespread convection occurs late over the anomalously dry soil in the GP in the M2D experiment, causing much greater rain rates over the domain in these two regions. Despite the more unfavorable CAPE conditions ahead of the MCS in the M2D experiment relative to the D2M and unaltered runs, the rain rate is boosted in the WY case by favorable deep layer shear driven by the density difference from the GP SM anomaly. Favorable shear also boosts the rain rate in the CO and NM experiments, but the results are skewed by the additional convective activity and by an increase in CAPE ahead of the NM system in the M2D experiment.

Fig. 3.16 summarizes the differences in shear and CAPE brought about by the differing SM anomalies, with plots of 500m AGL wind and most unstable CAPE for D2M minus M2D as well as composite reflectivity of all three regional MCSs for 0000 and 0800 UTC. CI in the high plains is assisted by anomalous upslope, low-level flow in the D2M case (Fig. 3.16a) driven by the air flowing from the anomalously higher pressure in the GP flowing westward to the anomalously lower pressure air in the high plains. Likewise, while higher CAPE to the west over the Rocky Mountains assists CI further to the west over high terrain in the M2D case (Fig. 3.16c). As MCSs mature in the central GP, the magnitude of the CAPE difference decreases ahead of the systems, but the difference in low-level winds is clearly in circulation around the GP SM anomaly, forming an anticyclone in the difference of the wind field, forcing anomalously greater (lesser) convergence into the WY MCS in the M2D (D2M) case in Fig. 3.16d (Fig. 3.16b) and vice-versa for the NM MCS at the south end of the GP SM anomaly.

Also of note is the difference in CAPE and shear on the flanks and trailing the quasi linear portion of the MCS in the NM and CO case. While the difference in low-level wind is unfavorable in the M2D case (Fig. 3.16d), negative CAPE values, meaning higher CAPE in the M2D case, lead to more widespread convection in the TX Panhandle as higher CAPE is moved off the moist anomaly to the west. In the CO case, the difference in low-level winds boost convection on opposite flanks of the MCS in each idealized case, with greater convergence on the north flank in the M2D case, forcing the convection near the KS/NE border, and on the south flank in the D2M case, where convergence and higher CAPE values are found in the OK

Panhandle region. This differing structure based on flow and stability is seen in the simulated rainfall totals in Fig. 3.17 with greater total precipitation where the line parallel structures appear in precipitation maxima in western OK/northern TX in the D2M case and central NE into northeast KS in the M2D case.

3.3.c. PBL Parameterization Sensitivity Results

This section compares the results of the idealized SM distribution model experiments conducted using the YSU PBL scheme versus the MYNN scheme used in section 3 and 4. Fig. 3.18 shows the total precipitation by hour. In all three regions the early, higher precipitation from 2200 to 0000 UTC is accelerated in the YSU runs. Unlike the other two domains, the WY D2M_YSU holds an edge in total precipitation until 0300 UTC when rate drop below the MYNN. D2M_YSU shows consistently higher precipitation in the CO and NM domain. The M2D results are similar for the NM domain with consistently higher precipitation through all times. WY results are the same, with consistently higher values in the YSU results while CO sees YSU precipitation rates peak at 0600 UTC and surpassed by MYNN in the final hours.

Precipitation Hovmöller diagrams for D2M model runs (Fig. 3.19) reveals that the rapid onset of precipitation in the YSU model run in the WY case after CI is owed to more focused precipitation in the High Plains between 2300 to 0200 UTC in the maxima east of Denver in Fig. 3.19b, as well as more widespread precipitation westward from 2200 to 0100 UTC. For CO (Figs. 3.19c and d), the slightly greater precipitation rates in the YSU scheme is seen the greater longitudinal extent of precipitation from 2200 to 0100 UTC. Afterwards, the pattern of precipitation is the same, but at a clearly greater magnitude along the track of the MCS eastward. For NM, the width of the signal in the Hovmöller is clearly wider in the YSU case (Fig. 3.19f), indicating more widespread precipitation from west to east, caused by more persistent convection behind the MCS as well as more convection preceding the MCS, with little difference along the maximum return axis caused by the MCS after 0400 UTC. Fig. 3.20 shows the precipitation totals Hovmöller for the M2D cases. For WY (Figs. 3.20a and b) there no noticeable difference between the diagrams, which matches the small difference in precipitation rate in Fig. 3.19. For CO, the large difference in precipitation rate from 0000 to 0500 UTC in Fig. 3.20 is seen to be at first greater east to west extent of precipitation at 0000 UTC in the YSU run, then a greater intensity of the MCS until 0500 when the diagrams are similar. For NM, while the extent of precipitation is roughly the same for both PBL scheme experiments, the intensity of precipitation is clearly stronger in the YSU case throughout the model run.

Examining the number and size of convective cells, Fig. 3.21a shows the difference between D2M_MYNN minus D2M_YSU for contiguous cells with 5 m/s updrafts at 500 hPa. Until 2200 UTC there are more cells that are on average smaller in the MYNN run. From 0000 UTC onward, the trends diverge, with many more convective cells in the CO YSU than MYNN run, though no evident trend on cell size. WY on the other hand trends toward more cells, though smaller cells on average, in the MYNN run. NM trends slightly toward more cells in the YSU run, with more cells in six of ten hours from 0000 to 1000 UTC. Fig. 3.21b shows the difference between M2D_MYNN minus M2D_YSU. Here, the number of cells is greater in the YSU run for nearly all times with the greatest difference coming in the CO case from 0000 to 0300 UTC when widespread convection occurs in the central GP and merges with the eastward moving MCS. There is less variance in the difference in cell size between the model runs in the M2D model runs compared to the D2M model runs. While neither difference plots for 10 m/s updraft cell counts and size show no interesting relationships, the M2D difference for 15 m/s cells reveals a reversal from the findings in Fig. 3.20b, with many more intense cells in the MYNN case rather than the YSU (not shown).

Fig. 3.22a shows the difference in CAPE and CIN for D2M_MYNN minus D2M_YSU. Differences in CAPE show no common trends across regions, with WY having higher CAPE in MYNN in nearly all times, CO higher in YSU until 0200 UTC then in MYNN for the remainder of the night, while NM shows higher values in MYNN only early night between 0400 to 0600 UTC. For CIN, for WY, MYNN has higher inhibition until 0600 UTC and beyond when YSU has higher inhibition. NM and CO share similar patterns for CIN with no difference in inhibition until 0200 when MYNN has greater inhibition than YSU for nearly all hours in both regions, with greater differences at 0600 UTC and later. Fig. 3.22b shows the differences in CAPE and CIN for M2D_MYNN minus M2D_YSU. CAPE values are higher in the YSU run for nearly all times, except very early and late in the WY case. Only NM shows a consistent relationship through time for CIN with greater inhibition in the MYNN case from 0200 to 0800 UTC, while CO and WY oscillate between higher CIN values in MYNN and YSU through time.

Fig. 3.23a shows the difference in PW and 0-6km shear for D2M_MYNN minus D2M_YSU. For D2M, WY shows consistently higher PW values in MYNN, NM higher values in YSU, while CO has no consistent relationship through time. While all regions begin with greater deep layer shear in YSU model runs, CO and WY have consistently higher shear values in with MYNN than YSU, while NM switches from higher shear with MYNN early and late, with YSU having higher shear 0400 to 0600 UTC. For M2D, before 0200 UTC MYNN tends to have higher PW values, but 0200 and later YSU shows higher PW values, especially in the 0200 to 0600 UTC timeframe. For shear, WY tends to have greater shear in the YSU experiment, while NM tends to have greater shear in the MYNN, while CO gradually shifts from higher shear in YSU early to higher shear in MYNN late.

3.4. Summary and Conclusions

Utilizing the results of a climatology of warm season MCSs originating in the high terrain of the Rocky Mountains and adjacent high plains developed in Chapter 2 of this dissertation, composite initial and boundary conditions were developed from three distinct source regions: southern WY/northern CO, Colorado, and southern CO/New Mexico. Each of these three source regions is home to an east-west oriented ridgeline extending from the Rocky Mountains, namely the Cheyenne Ridge (WY), Palmer Divide (CO) and the Raton Mesa (NM). These ridgelines are known foci for CI and source regions for MCSs. Composite initial conditions were developed from the NARR by taking the mean over all days for which the region was the source region for an MCS. For each region, a model run was made with no changes to the lower boundary condition, called UNALTERED model runs. Additionally, a series of idealized model runs were conducted in which idealized soil moisture (SM) anomalies and surface cover were imposed. The SM was made uniform throughout the domain (based on the average SM in the top soil layer in the UNALTERED initial condition) then anomalies were imposed in the MCS source region of the Rocky Mountain front range and adjacent high plains, and in the Great Plains (GP) to the east into which the MCS move in the night time hours. For example a positive (negative) SM anomaly in the high terrain and negative (positive) anomaly in the GP is a Moist-to-Dry or M2D (Dry-to-Moist, D2M) configuration. In these idealized model runs, the land use and soil type were made uniform throughout to remove these as factors impacting the results. First, a set of idealized runs were accomplished using only the MYNN PBL parameterization to compare the reaction of MCSs born in the three regions to the atmospheric changes brought about by the imposed SM anomalies. Second a set of model runs was made using the YSU PBL parameterization to compare the atmospheric response from differing the PBL parameterization and the response of the simulated MCSs to the change in parameterization.

In the UNALTERED experiment, all three regional model runs produce simulated MCSs with realistic features in the simulated composite reflectivity fields in Fig. 3.3. The WY case is the quickest to transition from individual convective cells to an organized MCS, at roughly 0000 UTC. The CO case shows the most widespread initial convection at 0000 UTC then the MCS of greatest areal extent by 0800 UTC. The NM case shows widespread convection in NM as well as east of the source region in the TX Panhandle, then two MCSs, one originating in northern NM and one originating to the east in TX at 0400, then the weakest of the three MCSs at 0800 pushing to the southeast into central TX. Examination of updrafts with a minimum of 5 m/s vertical velocity at 500 hPa (Fig. 3.4a) confirms what is apparent from the reflectivity fields, with the CO model run showing the largest number of convective cells and NM the least. Interestingly, all three regions show an increase in the number of cells until 000-0100 UTC, then a lull between 0200 and 0400 UTC as the individual cells transition to organized MCS. Looking at mean size of all convective cells, WY shows larger cells throughout, increasing in size until 0400 UTC then slightly decreasing into the end of the model run. Examining only intense convective cells (Fig. 3.4b), there are comparable numbers in both the WY and CO model runs, with both showing steadily growing numbers of intense cells until 0600 UTC, while the NM model run shows a steady number after 2300 UTC. The size of intense convective cells remains steady across model runs and times.

The reason for variance in the areal extent and numbers and intensity of convective cells across the regional model runs are explained by examining the horizontal variations of CAPE (Fig. 3.5), PW and deep layer shear (Fig. 3.6) as well as the development of these variables in the environment preceding each MCS (Figs. 3.7 and 8). The most striking difference seen in the spatial extent of thermodynamic variables is the lack of CAPE and PW in the northern half of the domain in the NM model run, limiting the spatial extent of this system, whereas the WY and CO case move into the GP with abundant CAPE and PW throughout, with CAPE higher over a wider area in the WY case and higher PW in the CO case. Examining the change in variables preceding the system, while most unstable CAPE values rise steadily in the WY case to a maximum of 2400 J/kg at 0800 UTC and remain steady in the CO case between 1000 and 1500 J/kg, both see large values of CIN from 0200 UTC onward. This is opposed to the NM case with low CAPE until 0800, then a jump and low CIN until a steady increase starting at 0600 UTC. The 0-6km shear values show a similar pattern for all three regional cases, with a steady decrease through time.

Comparing the idealized model runs using the MYNN PBL scheme, Fig. 3.10 shows that the initial convection occurs much further east in the D2M experiments, with cells transitioning to MCSs nearly 200km further east in than in the M2D experiment at 0000 UTC. The other major difference in development is more widespread convection ahead of the MCS in the CO and NM model runs. While initial CI in higher terrain is impacted by the western SM anomaly, timing and cell motion in Fig. 3.10 shows that the MCSs spend most of their time over the larger GP SM anomaly, which has a greater impact on the thermodynamic variables preceding the system. This is seen in the differences of MUCAPE, CIN (Fig. 3.12) and PW and shear (Fig. 3.13) for D2M minus M2D. While slightly higher PW and CAPE are seen in the initial hours for

M2D, this quickly reverses with much larger CAPE and PW, with the smallest difference in CAPE in the NM case.

The 0-6km shear shows similar patterns through time for WY and CO, with positive values early switching dramatically to negative values after 0200 UTC, meaning higher shear values over D2M early and larger over M2D late. This difference in shear is caused by low-level air density anomalies over the GP SM anomaly due to differences in sensible heat flux and air temperature. Fig. 3.14 shows that a positive low-level pressure anomaly develops and persists over this area, driving a cyclonic (anticyclonic) low level wind flow around the anomalously dry (wet) soils in the central GP, driving differences in shear, most starkly between the WY and NM cases, which transit the north and south edges of the GP SM anomaly and differing directions of shear brought on by the SM anomaly.

In terms of domain-wide precipitation amounts (Fig. 3.15), despite D2M showing large precipitation rates early in all regions, rates diminish through time despite much higher values of CAPE preceding the system compared to the M2D experiments. In the WY case, the decrease of precipitation rate is most dramatic, falling below the rate in the UNALTERED run until the final hours. The greater precipitation rates in the CO and NM cases are attributed mainly to the more widespread convection over the GP over the relatively hot, dry SM surface which persists until the end of the run. The NM M2D experiments shows the most dramatic advantage in total precipitation, owed also to more favorable deep layer wind shear caused by the GP SM anomaly.

Examining the difference in variable and MCS development due to the use of PBL parameterization, Fig. 3.18 shows that in nearly all regions and SM configuration, the model runs using the YSU parameterization produce a higher precipitation rate, with higher precipitation rates earlier. Fig. 3.22 shows that CAPE tends to be higher over dry soils when using the YSU scheme, with higher values early in the area of CI in the D2M experiments and higher values later ahead of the MCS in the GP in the M2D experiments. Evidence of a stronger boundary layer response in the YSU model runs is seen in Fig. 3.23b, with opposite responses in the difference between shear experienced by the NM and WY MCSs with stronger shear experienced by the WY MCS and the opposite by the NM MCS in the YSU run, due to a stronger low level density anomaly and anomalous cyclonic flow around the SM anomaly in the GP.

Future work includes the use of satellite data to further develop the climatology of this class of MCS, including MODIS land surface variables as well as satellite measured SM data. Additionally, a more idealized study of the importance of land use, SM and slope play on the initiation of convection and the development of subsequent MCSs will be undertaken. While the differences between the MYNN and YSU PBL parameterization scheme were subtle, further study should be undertaken to understand the sensitivity of MCS lifecycle to PBL scheme with varying topography, land cover, soil type and SM. Additionally, the transportability of this study to similar MCS regimes in other regions of the world, including China and Argentina, should be explored to study the effects of idealized soil moisture variations to differences in background flow and land/ocean configurations presented in other regions.

3.5. Figures

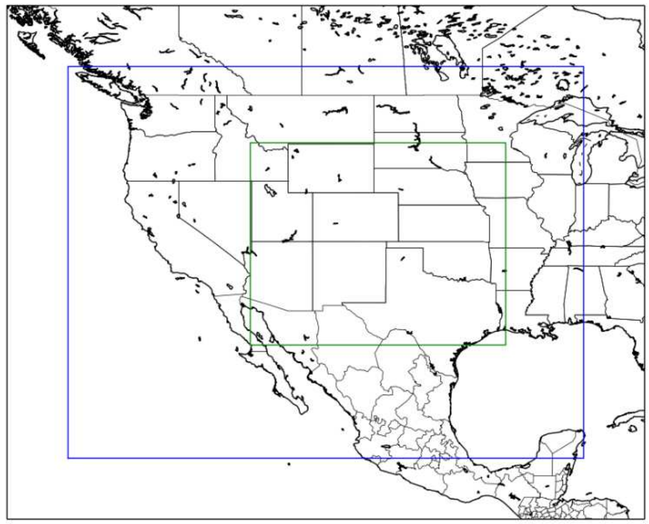

Figure 3.1. WRF simulation domains for 16 kilometer grid spacing (blue) and 4 kilometer grid spacing (green).

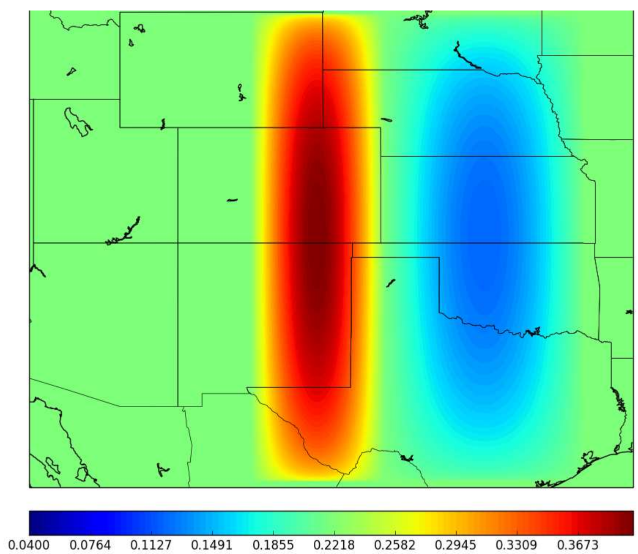

Figure 3.2. Idealized soil moisture anomaly for the moist to dry (M2D) experiment. D2M would have the dry anomaly in the High Plains and wet soil anomaly in the central plains.

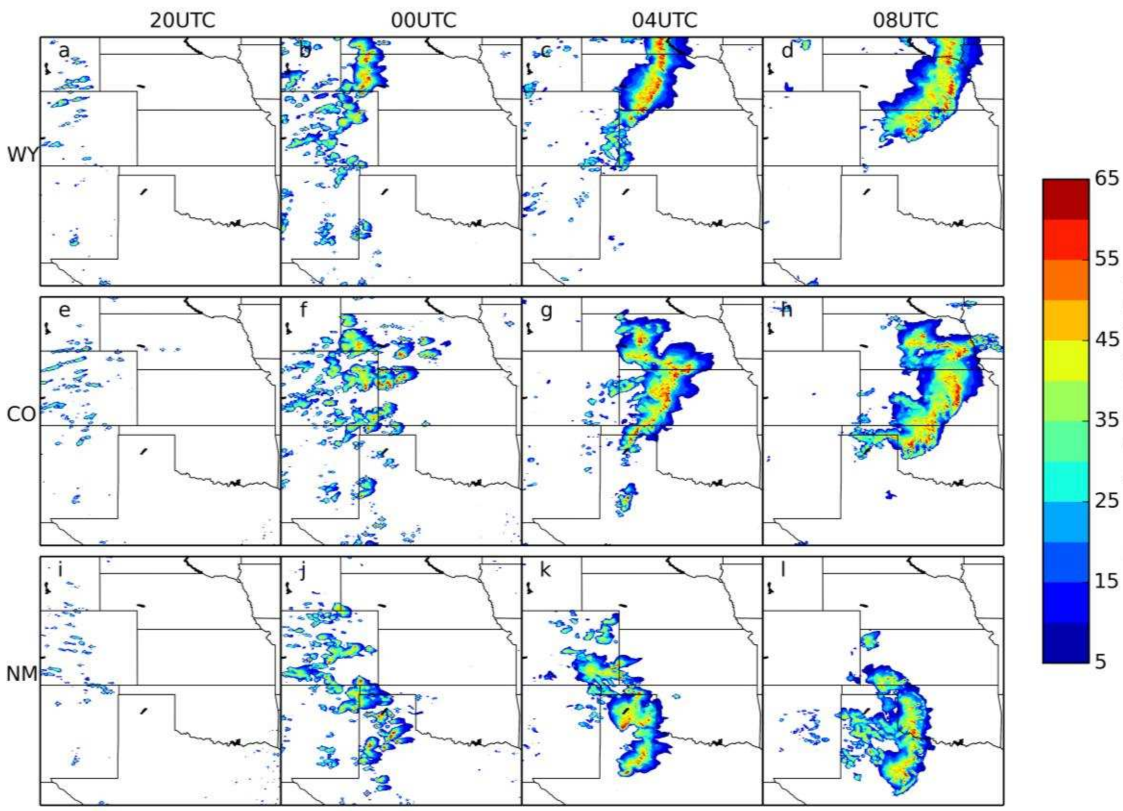

Figure 3.3. Simulated Composite Reflectivity, UNALTERED lower boundary condition for the Wyoming (top, a to d), Colorado (middle, e to h) and New Mexico (i through l) for 2000, 0000, 0400 and 0800 UTC.

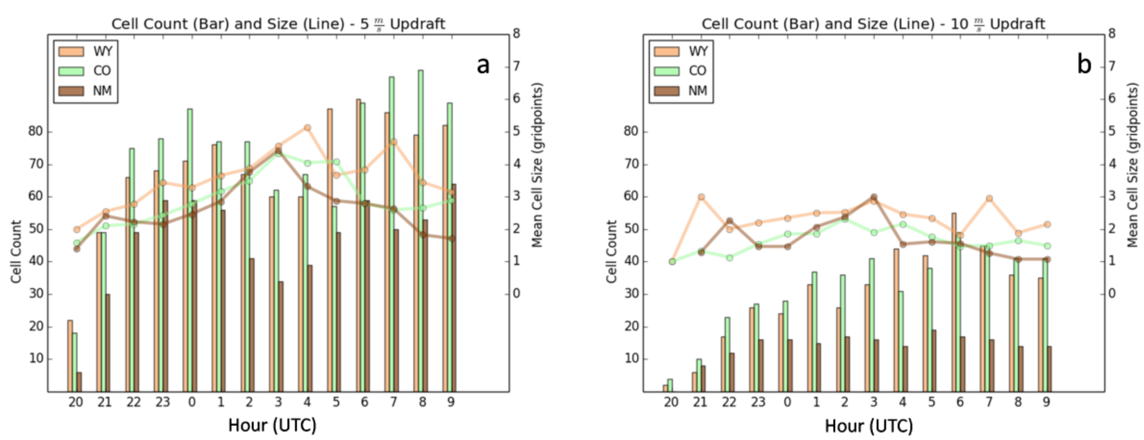

Figure 3.4. Convective cell count and mean convective cell size for cells with contiguous areas of at least (a) 5 m/s and (b) 10 m/s.

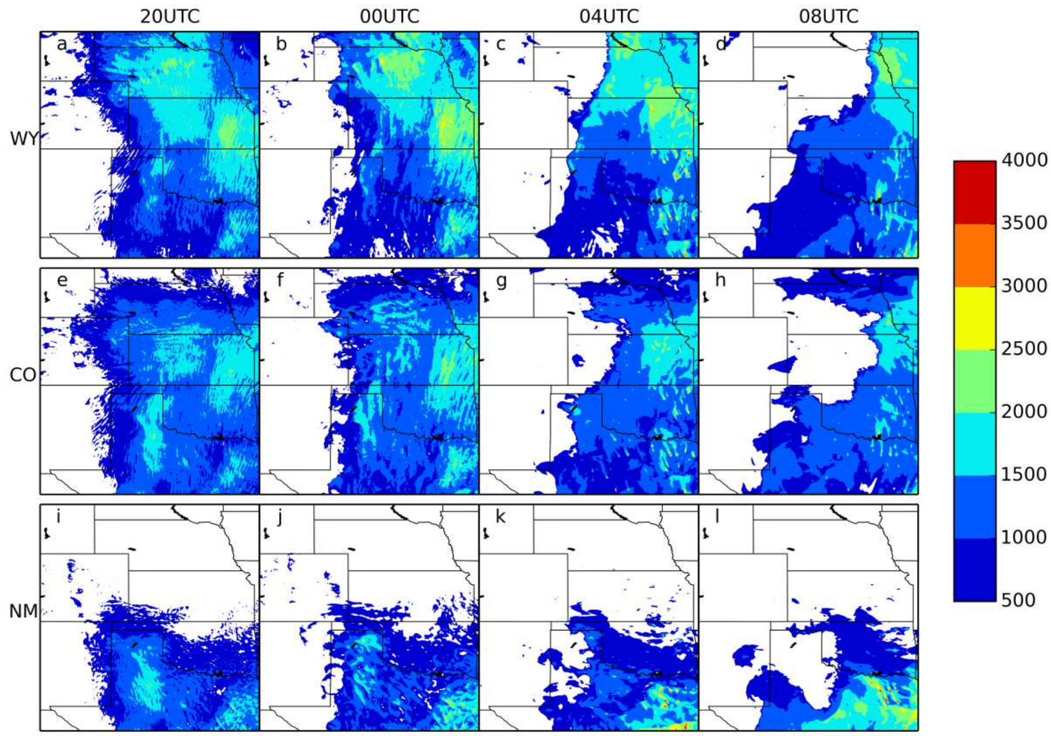

Figure 3.5. Most Unstable CAPE, UNALTERED lower boundary condition for the Wyoming (top, a to d), Colorado (middle, e to h) and New Mexico (i through l) for 2000, 0000, 0400 and 0800 UTC.

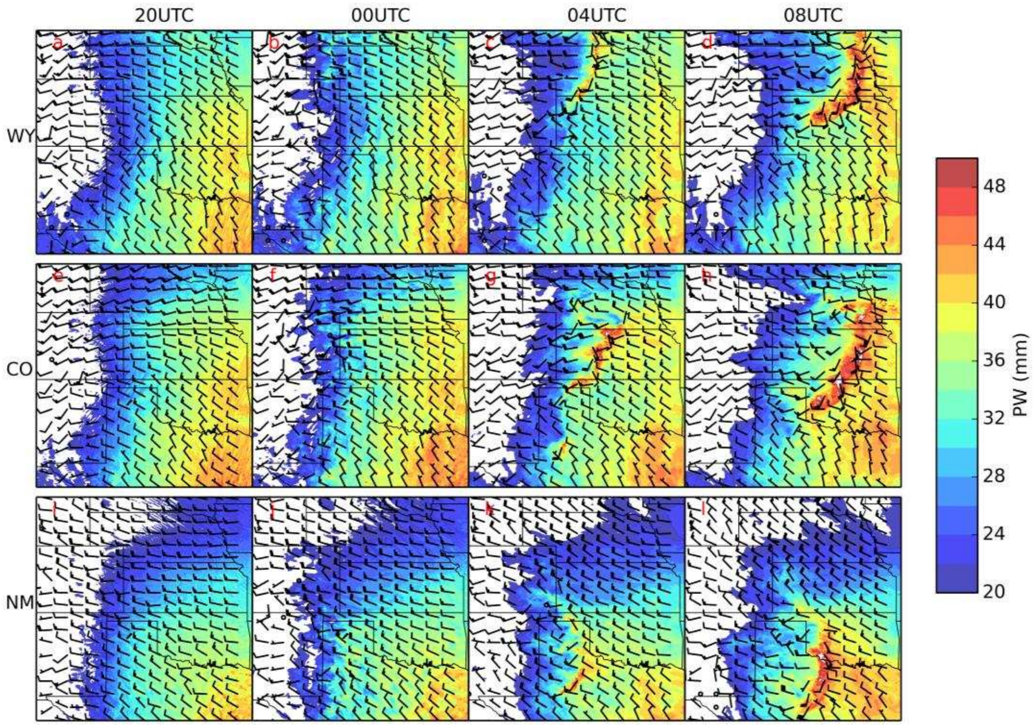

Figure 3.6. PW (color fill) and 0-6km shear (wind barbs) for the Wyoming (top, a to d), Colorado (middle, e to h) and New Mexico (i through l) for 2000, 0000, 0400 and 0800 UTC.

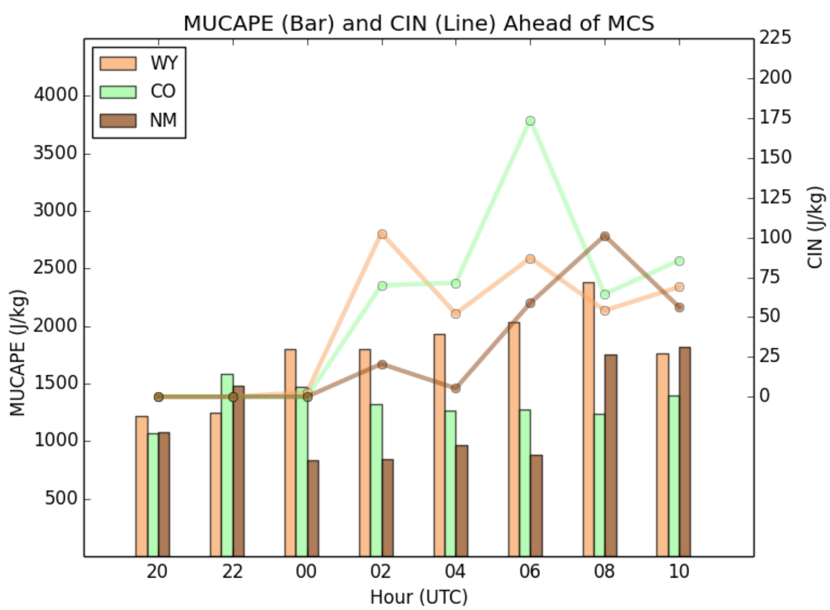

Figure 3.7. Most Unstable CAPE (bar) and CIN at the MU level (line graph) by hour and region for UNALTERED model runs.

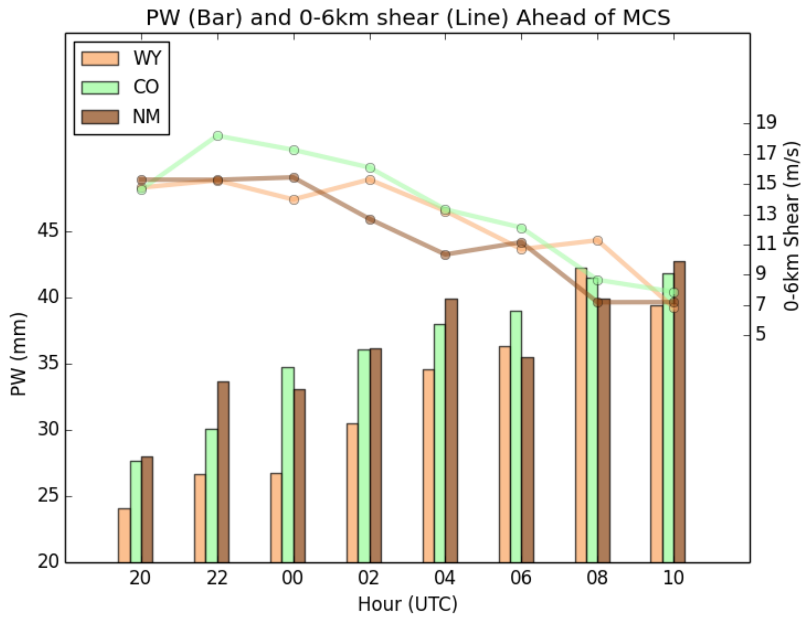

Figure 3.8. PW (bar graph) and 0-6km shear (line graph) by hour and region for UNALTERED model runs.

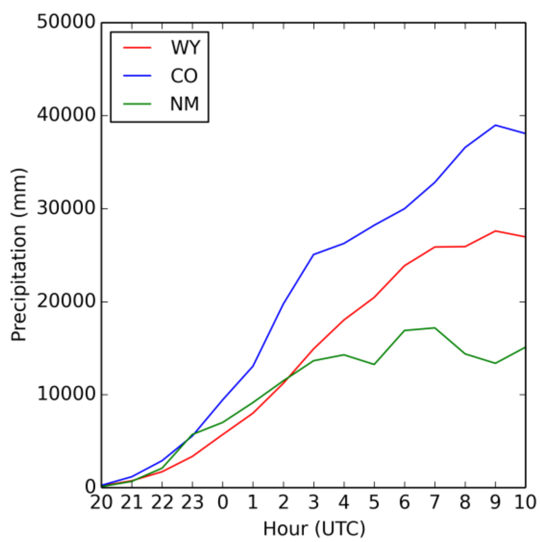

Figure 3.9. Domain-wide accumulated precipitation for each unaltered model run.

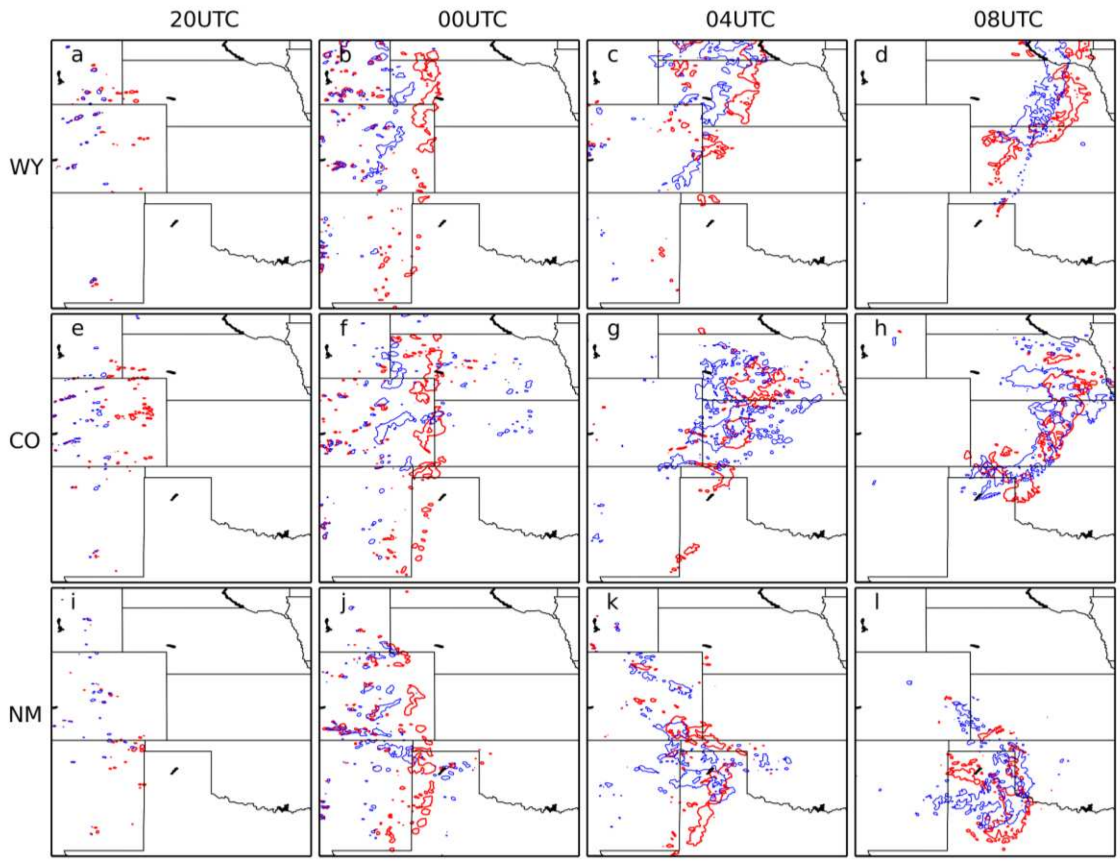

Figure 3.10. Isopleths of the simulated composite reflectivity 35 dBZ contour for D2M (red) and M2D (blue) model runs utilizing the MYNN PBL parameterization for the Wyoming (top, a to d), Colorado (middle, e to h) and New Mexico (i through l) for 2000, 0000, 0400 and 0800 UTC.

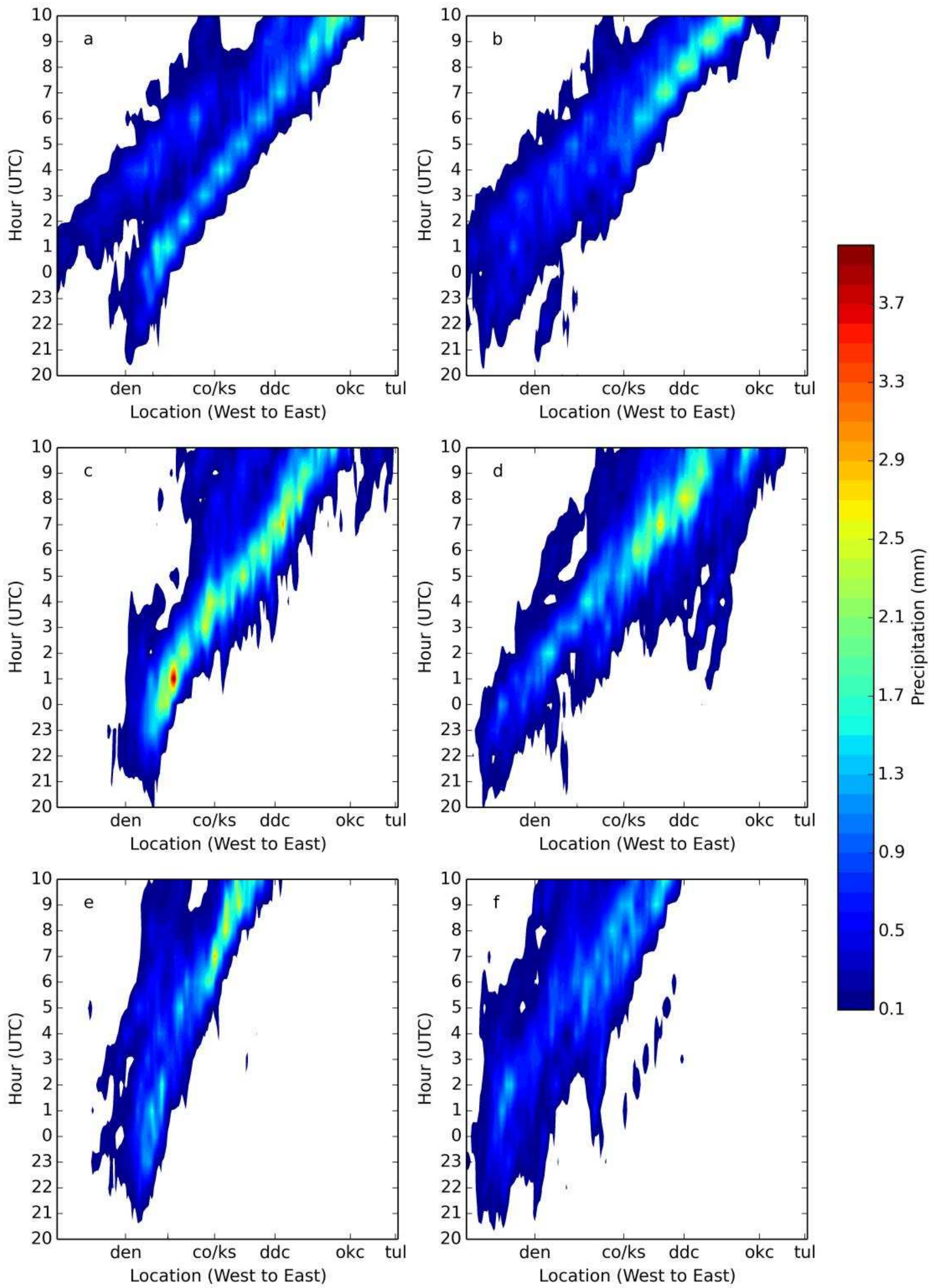

Figure 3.11. Hovmöller diagrams for hourly precipitation (y-axis) by longitude location (x axis) for the Wyoming (top, D2M, a andM2D, b), Colorado (middle, D2M, c and M2D, d) and New Mexico (D2M, e and M2D, f).

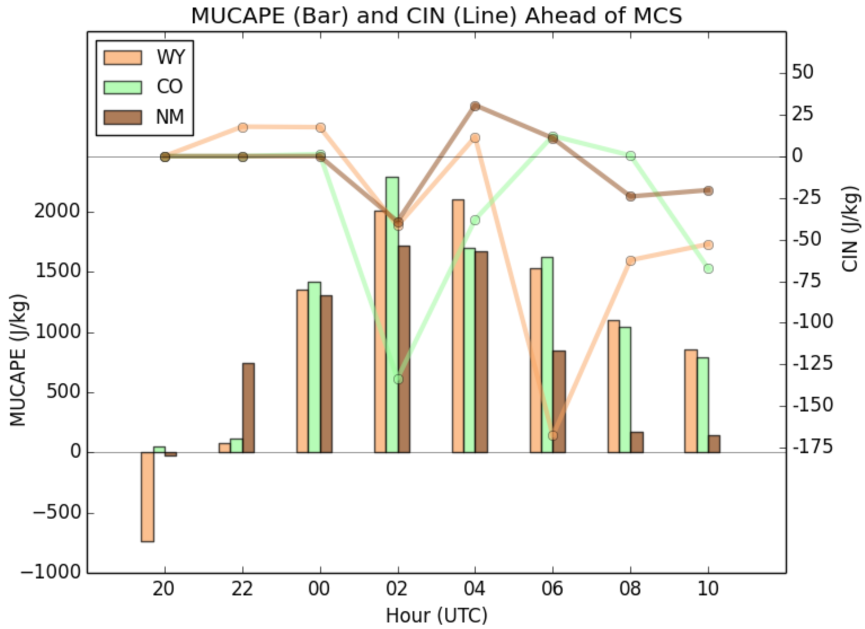

Figure 3.12. Most Unstable CAPE (bar) and CIN at the MU level (line graph) difference for D2m minus M2D by hour and region for UNALTERED model runs.

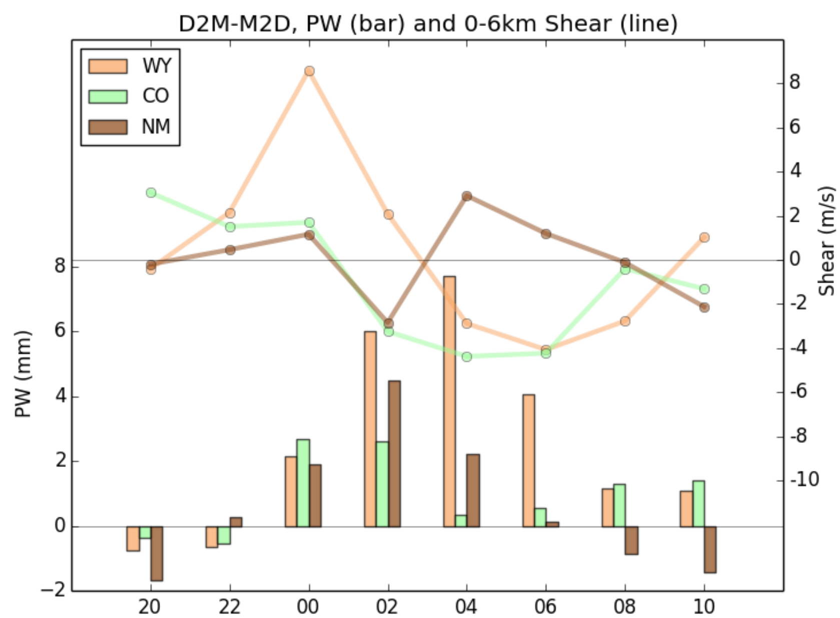

Figure 3.13. PW (bar) and 0-6 km shear (line graph) difference for D2m minus M2D by hour and region for UNALTERED model runs.

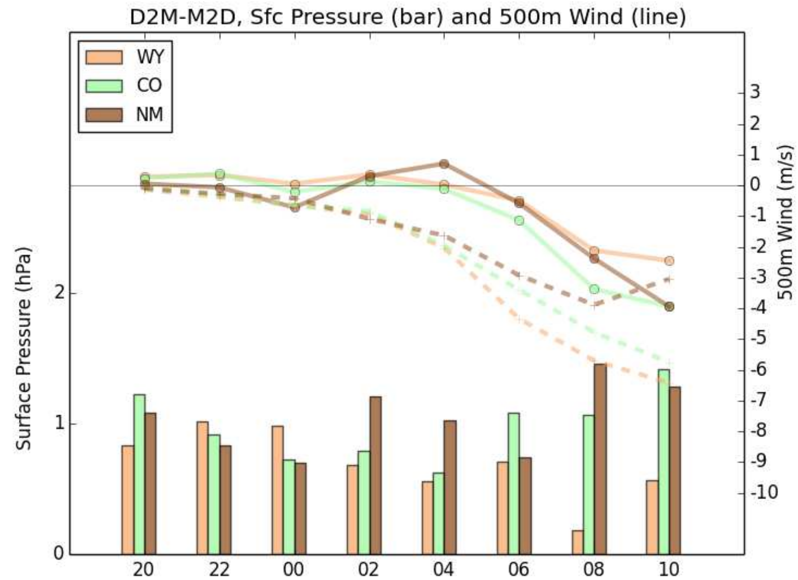

Figure 3.14. Mean sea level pressure averaged over southern Oklahoma (bar) and meridional wind anomaly in eastern Kansas (dotted line graph) and zonal wind in central Texas (solid line graph) difference for D2m minus M2D by hour and region for UNALTERED model runs.

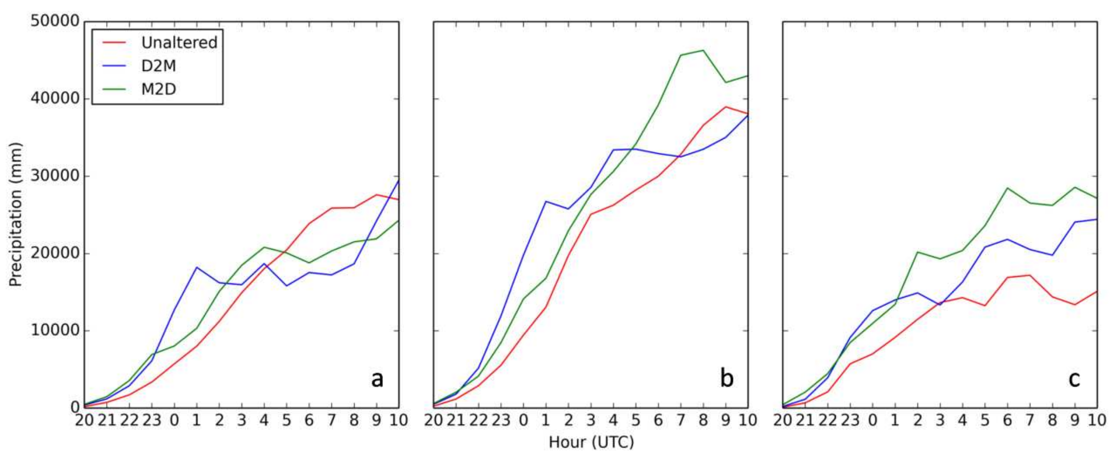

Figure 3.15. Domain-wide accumulated precipitation for each unaltered (red), D2M (blue) and M2D model run for (a) Wyoming, (b) Colorado and (c) New Mexico.

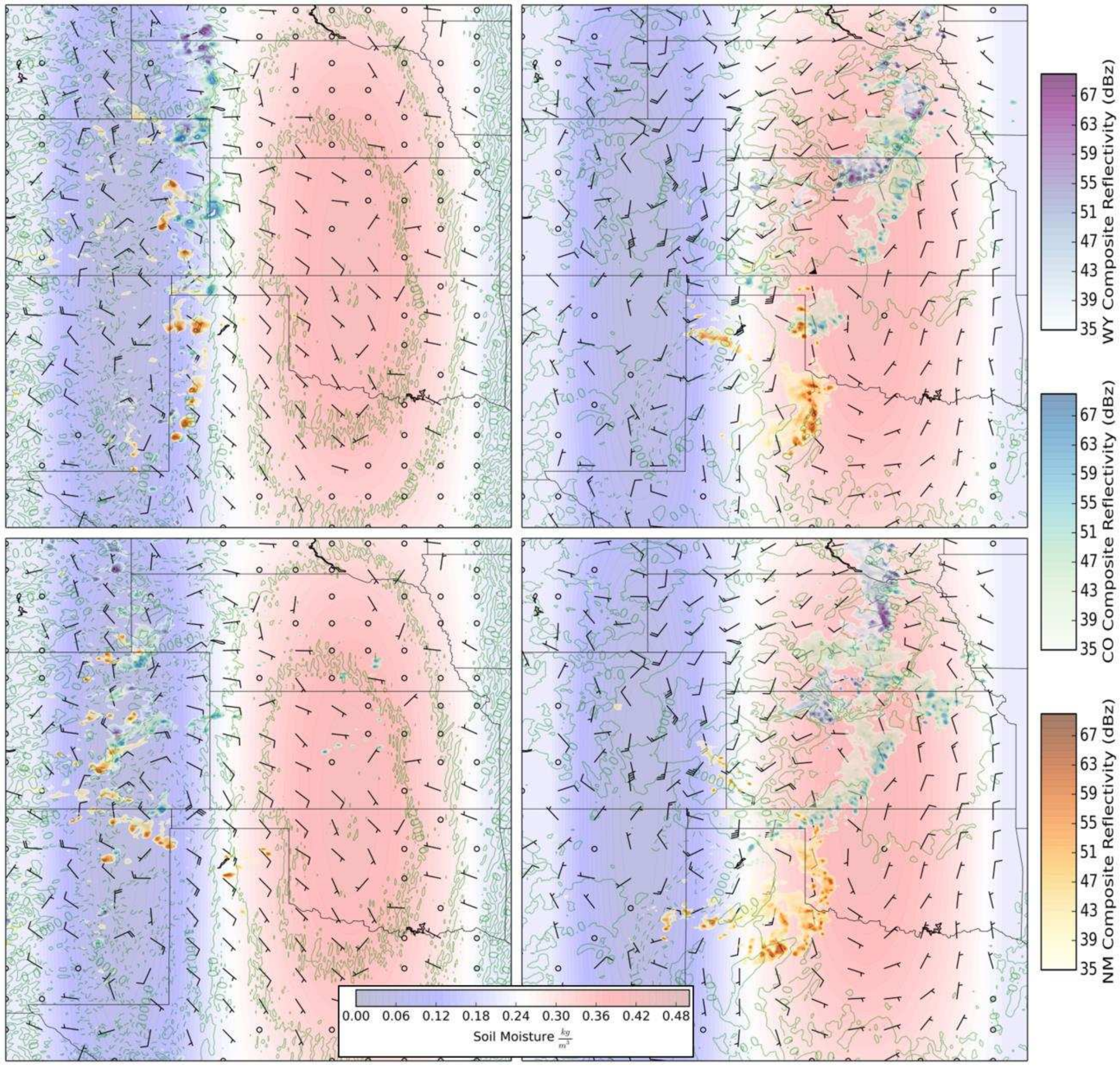

Figure 3.16. Differences for 500m AGL wind and most unstable CAPE (green contour, negative in dashed contours) for D2M minus M2D. Composite reflectivity is plotted for each regional MCS for D2M in (a) and (b) and M2D in (c) and (d). Background is the initial SM anomaly imposed in the D2M simulations.

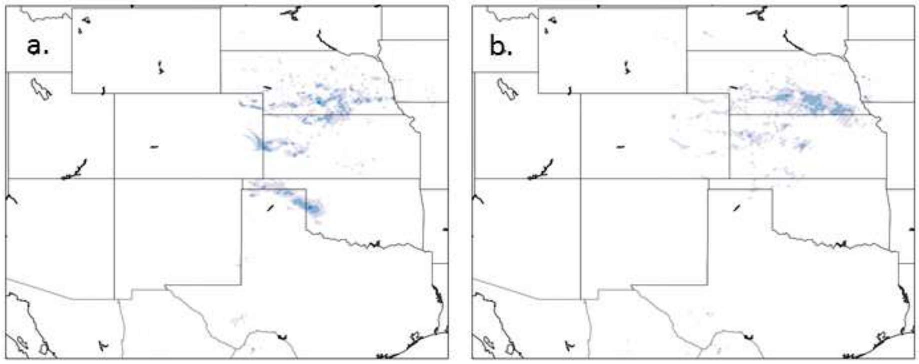

Figure 3.17. Total simulated precipitation in excess of 25 mm (light blue) and 50 mm (dark blue) for the Colorado D2M (a) and M2D case (b).

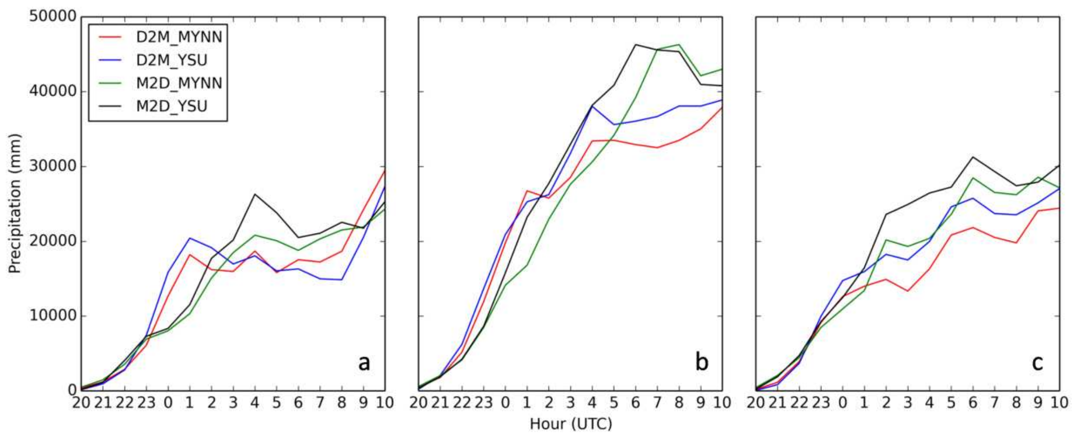

Figure 3.18. Domain-wide accumulated precipitation for each D2M model run using MYNN PBL parameterization (red), D2M using YSU (blue) and M2D using MYNN (green) and M2D using YSU for (a) Wyoming, (b) Colorado and (c) New Mexico.

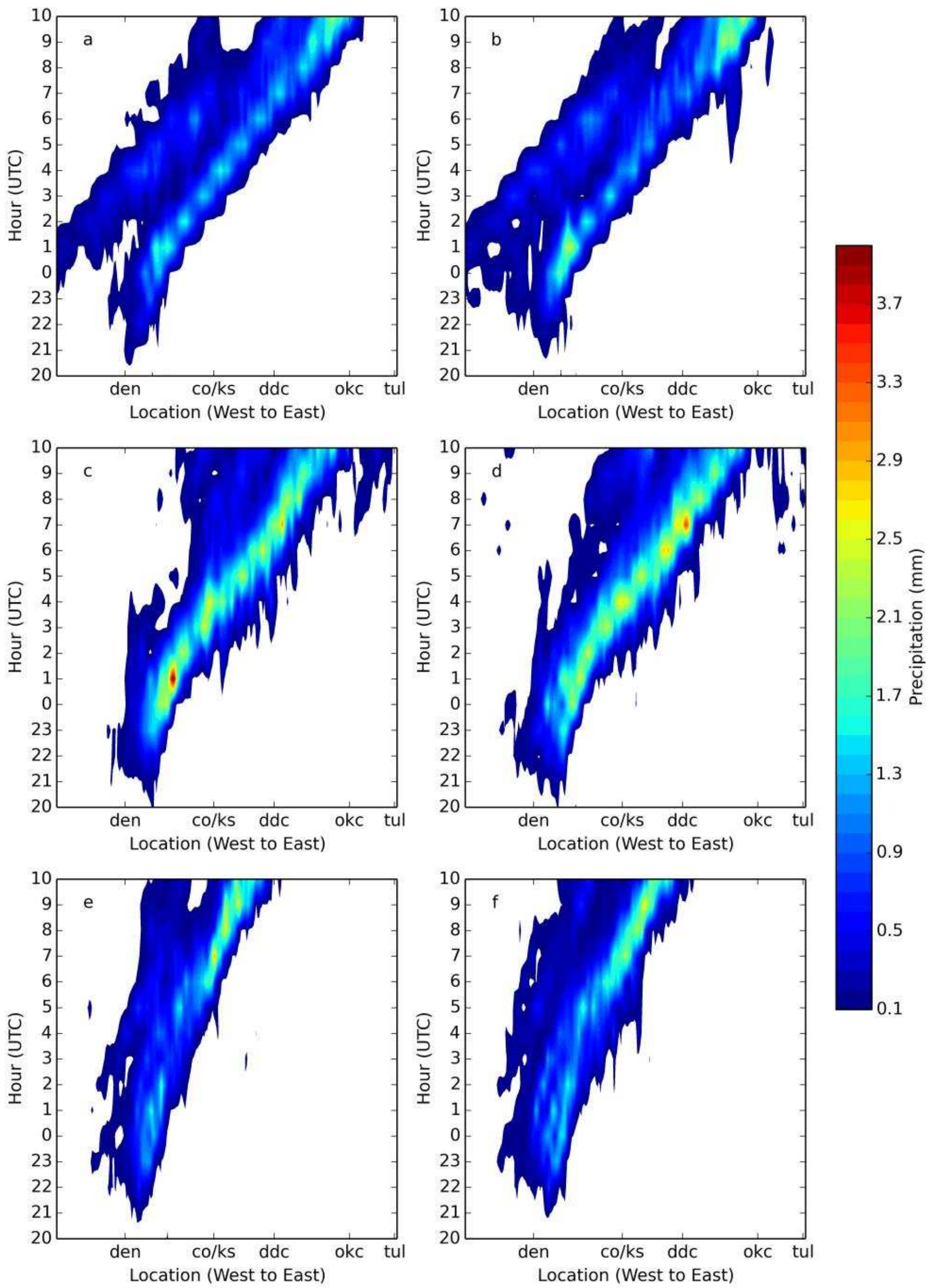

Figure 3.19. D2M Hovmöller diagrams for hourly precipitation (y-axis) by longitude location (x axis) for the Wyoming (top, MYNN, a and YSU, b), Colorado (middle, MYNN, c and YSU, d) and New Mexico (MYNN, e and YSU, f).

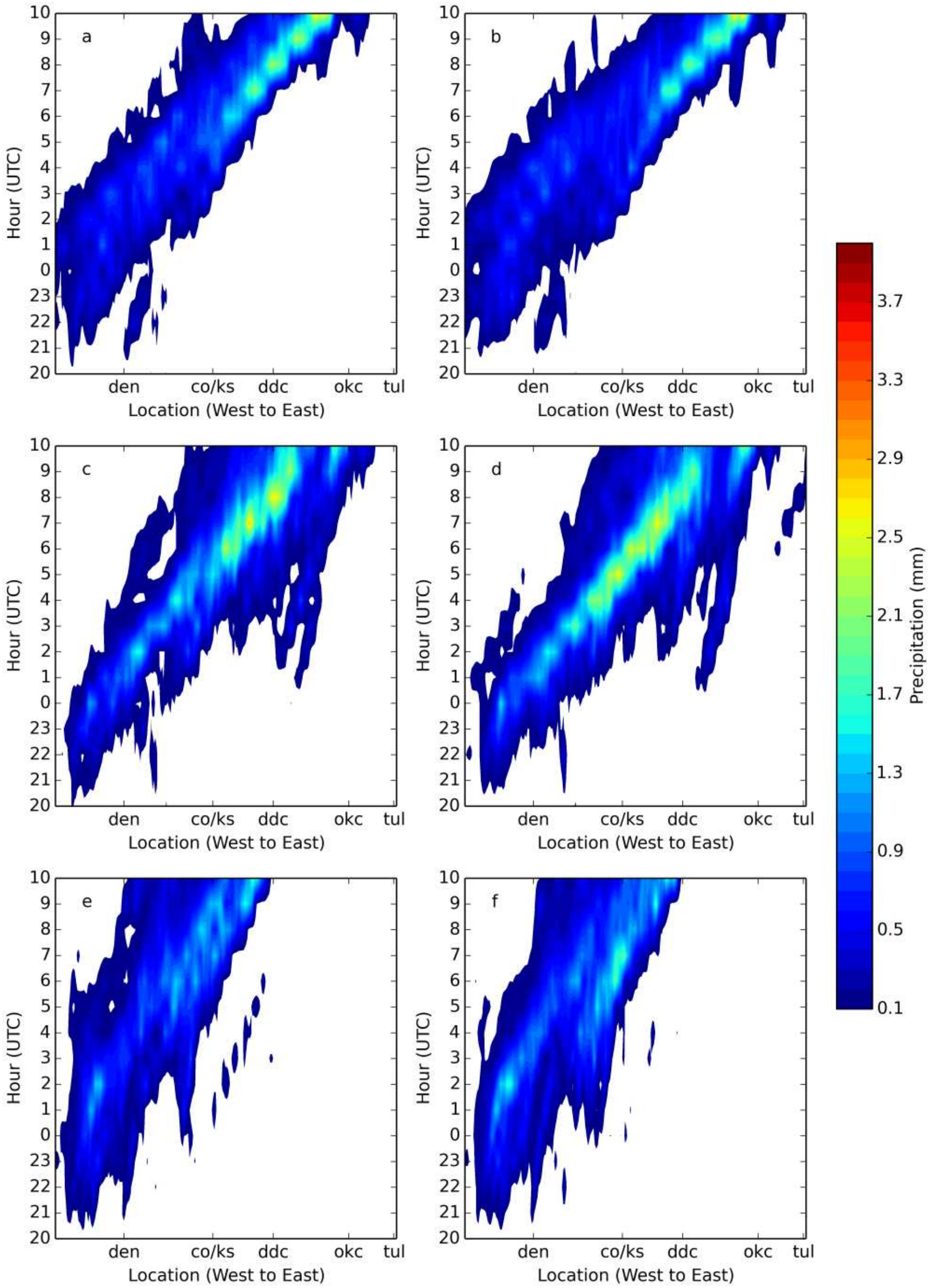

Figure 3.20. M2D Hovmöller diagrams for hourly precipitation (y-axis) by longitude location (x axis) for the Wyoming (top, MYNN, a and YSU, b), Colorado (middle, MYNN, c and YSU, d) and New Mexico (MYNN, e and YSU, f).

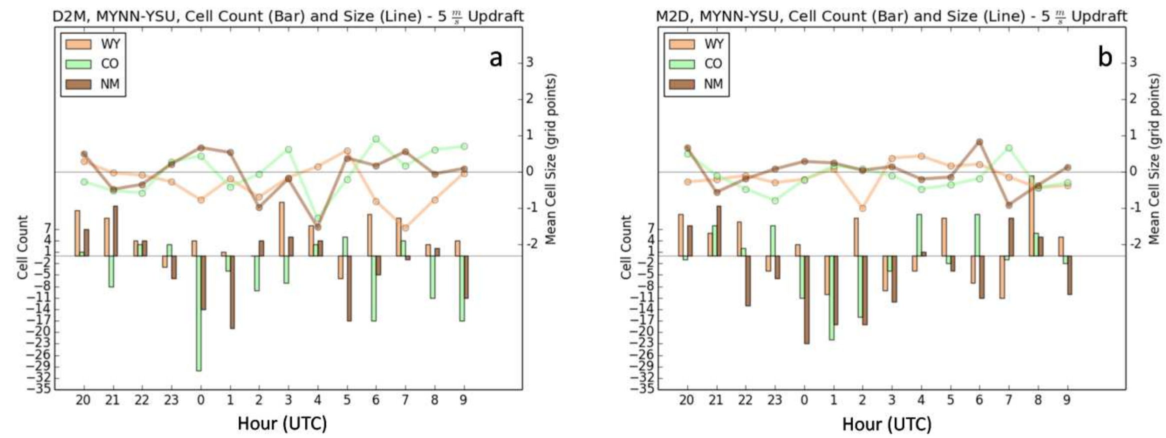

Figure 3.21. Convective cell count (bar) and mean cell size total grid points (line graph) for cells with contiguous vertical velocity of at least 5 m/s at 500 hPa. Difference for MYNN minus YSU model runs for (a) D2M and (b) M2D experiments.

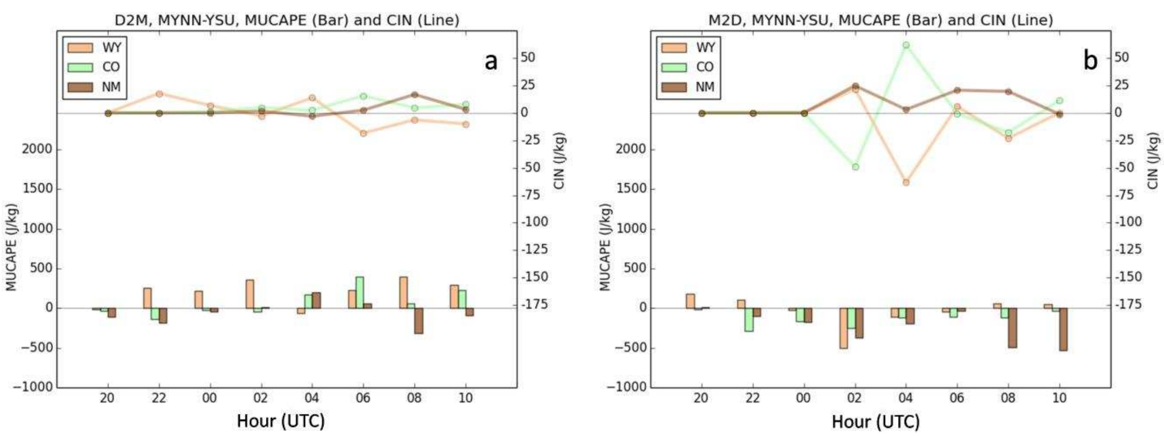

Figure 3.22. Most Unstable CAPE (bar) and CIN at the MU level (line graph) difference for MYNN minus YSU model runs for (a) D2M and (b) M2D experiments.

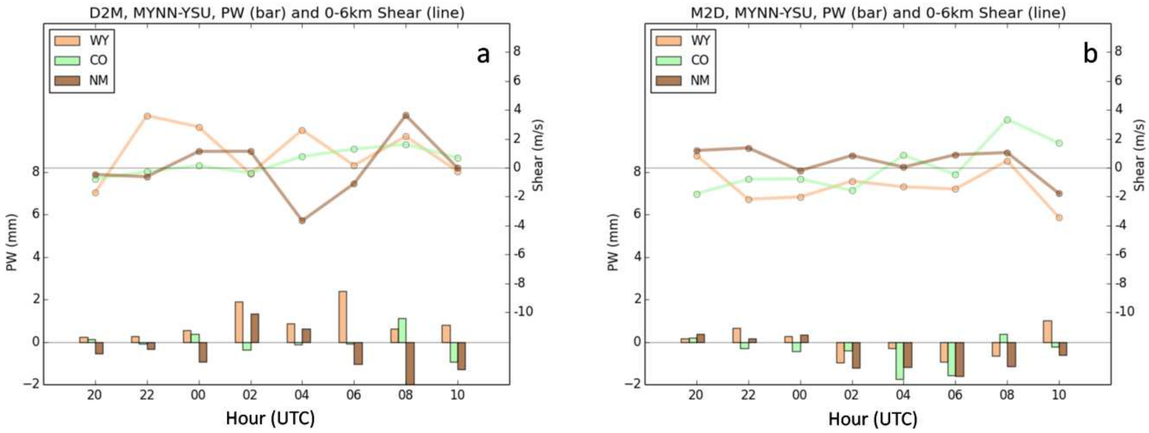

Figure 3.23. PW (bar) and 0-6 km shear (line graph) difference for MYNN minus YSU model runs for (a) D2M and (b) M2D experiments.

CHAPTER 4

THE IMPACT OF SOIL MOISTURE AND VEGETATION COVER ON ROCKY MOUNTAIN FRONT RANGE AND HIGH PLAINS CONVECTION INITIATION

4.1. Introduction

Convection Initiation (CI) remains a challenge to both forecasters and researchers to understand when and where CI where occur, what environmental factors are important in order to accurately portray CI in numerical models, as well as understanding the impact of timing and spatial errors in CI have on subsequent forecasts. Lock and Houston (2014) examined CI over the central CONUS using Level II WSR-88D data from 2005-2007 in context of atmospheric variables derived from the 20-km Rapid Update Cycle 2 dataset, finding over 55,000 CI events which were then compared to null points that were similar temporally and spatially. Across all cases, lift was found to be the most important factor in discriminating between areas with CI and not. Burghardt et al. (2014) examined 25cases of CI in the Front Range of the Rocky Mountains and adjacent high plains using the WRF model at 429m horizontal grid spacing. They found a high probability of detection of CI events, but an overproduction of CI events led to high false alarm rate and bias, especially in the higher elevations in the Front Range. Zhang et al. (2015) found that small shifts in simulation parameters, such as terrain and time, influenced planetary boundary layer and large-scale environmental characteristics, which then influenced timing and position of CI. The errors associated with CI timing and position then propagated through the simulation leading to large forecast uncertainties of subsequent supercells and mesoscale convective systems (MCSs).

The state of the land surface plays a major role in determining the state of the PBL which, in turn, influences convective precipitation, from the spatial and time scales of individual cumulus clouds to synoptic spatial scales and climate timescales. Lamb et al (2012) found that, from a moisture budget perspective, that local recycling of water vapor had a minimal impact on precipitation from daily to seasonal timescales during the warm season of 2007 in the GP. Frye and Mote (2010) examined a seven-year dataset of TRMM Microwave Imager SM data and CI points derived from KTLX WSR-88D radar data over Oklahoma, finding that, while CI was more prevalent on days that were synoptically primed, that differences existed in the behavior of initiation based on SM amount, SM gradients and LLJ presence over the region. Ford et al (2015) found a link between synoptic conditions and precipitation patterns, finding that in the warm season over Oklahoma, afternoon precipitation tends to fall over wet soils when the LLJ is absent and over dry soils when the LLJ is present.

The role of the SM in conjunction with the state of the overlaying atmosphere has been explored in the development of the PBL, cumulus clouds at the top of the PBL and deep moist convection. Utilizing a Large Eddy Simulation, Ek and Holtslag (2004) found mixed results regarding cumulus development depending on boundary layer and just above boundary layer conditions. They found that increased SM leads to increased cumulus cloud formation if the stability above the boundary layer is not too weak, whereas drier soils and weak stability above also leads to more cumulus cloud formation.

Convection initiating in the higher elevation of the Rockies/HP often propagates to the east with the mean mid-tropospheric flow, sometimes growing upscale from individual cells into mesoscale convective systems that are of great importance to the hydrologic cycle of the lower plains to the east. The importance of this phenomenon has been studied and refined through the years with the advent of more advanced data sets, beginning with studies of crop damage from hail (Crow 1967), studies with early radar (Henz 1974) and studies with the first geostationary satellite data records (Banta and Schaaf 1987) and more recently with Carbone et al. (2002) and Carbone and Tuttle (2008), using the WSI NOWrad dataset.

The aim of this study is to utilize a modern, high temporal and horizontal resolution precipitation dataset to develop climatology of CI in the High Plains and adjacent Rocky Mountains from central New Mexico to southern Wyoming. Using an offline land surface model derived SM dataset and a satellite derived vegetation index, the sensitivity of CI to SM and vegetation will be studied by region and elevation. The relationship between underlying SM and vegetation states and atmospheric variables related to buoyancy and total column water vapor to CI will be examined.

The remainder of this paper is as follows. Section 2 provides an overview of the datasets and methods applied in this research. Section 3a develops climatology of CI in the region of study and examines the relationship between SM and vegetation to CI timing. Section 3b examines the relationship of CI events to SM and vegetation as well as overlaying atmospheric variables. Section 3c examines the covarying relationship between SM, CI and overlaying atmospheric variables. Section 3d looks at the difference in CI characteristics on MCS and non-MCS days as defined in chapter 2 of this dissertation. Section 4 concludes the paper with a discussion of results and future work.

4.2. Data and Methods

A system for identifying initial precipitating areas, used as a proxy for CI, was developed using the hourly Stage IV precipitation analysis (Lin and Mitchell 2005) from 2003 through 2015 for May through August over central and eastern Colorado, Wyoming, and New Mexico. Starting at 1500 UTC (9:00am local time), areas of CI were identified as individual areas between ~50 and 500 km^2, or the area of individual deep, moist convective cells and exceeded 2 mm/hr rain rate in each grid point in the object. This approach was similar to that used by Duda and Gallus (2013) who used initial precipitation rates of 3mm/hr over at least one grid cell to define CI objects. A lower threshold is used in this study due to the probable underestimation of precipitation by NEXRAD and Stage IV over the elevated, complex terrain of the Rocky Mountains. Other threshold size and magnitude thresholds were implemented to test the sensitivity of results, varying the magnitude of precipitation rate from at least 1 to 4 mm/hr and varying the size of precipitation area from 1 to 6 grid cells. Varying magnitude to less than 2 mm/hr too often failed to identify the footprints from individual convective cells, but instead bounded the footprint of several convective cells, incorrectly finding the center of mass of a larger precipitation rate area. Using magnitudes greater than 2 mm/hr and sizes greater than 2 grid cells found most of the same cells in the 2/2 threshold at lower elevations to the east but failed to detect many cells at higher elevations when examined in subjective verification.

For the succeeding hour, a mask is placed over the identified CI area and downstream for a distance indicated by the North American Regional Reanalysis (NARR: Mesinger et al. 2006) 600-hPa wind, to account for the movement of the convective cell. This mask is persisted for three hours after initiation time then removed to allow for new CI objects to be identified in this area. Masks are developed and carried forward in a similar way for systems exceeding the size threshold of 500 km^2. An example of object identification is shown in Fig. 4.1. Fig. 4.1a shows the identification of CI objects 0 through 5 and the NEXRAD composite for the same hour. Fig. 4.1b shows the next hour, with the masks, in green, developed for the objects identified in Fig.

4.1a. Also depicted in Fig. 4.1a are the seven regions of this study. Each of the seven regions is broken down into a west and east sub-regions based on the presence of mountainous terrain to the west and plains to the east based on a subjective examination of the greatest change in gradient of elevation. North to south, the regions were made based on the presence of east-to-west ridgelines (Cheyenne Ridge-CHY, Palmer Divide-PAL and Raton Mesa-RAT) with relatively low laying areas adjacent (NOR-North, PLT-South Platte River Valley, ARK-Arkansas River Valley, SOU-South).

To evaluate possible relationships between CI and SM, SM data from the North American Land Data Assimilation System 2 (NLDAS) are used (Xia et al 2012). The NLDAS is an offline land surface model run with observations of surface weather and hydrologic phenomenon. The CPC gauge-only precipitation dataset is used, disaggregated through time with NEXRAD Stage II data. For this study, the 1200 UTC analysis of 0-10 cm depth SM is used to examine relationship with CI on the following 1500-0300 UTC day. The horizontal resolution of the NLDAS is one-eighth degree or roughly 14 km. The NLDAS snow mask was also used to eliminate CI points occurring at points with greater than 25% snow cover at the grid point. The vegetation data used was from the Moderate Resolution Imaging Spectroradiometer (MODIS) Enhanced Vegetation Index (EVI) dataset updated every 16 days. The level 3 dataset was utilized, which has 1-kilometer resolution and utilizes data from both the Aqua and Terra Satellites.

NARR surface-based Convective Available Potential Energy (CAPE), Convective Inhibition (CIN) and precipitable water (PW) are used to examine the variability commonly used CI and convective potential/intensity variables as surface characteristics (SM and EVI) change through time and space. First, CAPE is useful to study the phenomenon in this research, afternoon convection initiated during the daytime with well-mixed deep boundary layers. Second, due to the limited number of vertical layers in the NARR, the mixed-layer CAPE shows little to no correlation to that derived from radiosonde derived data in the region, while surface-based CAPE (CAPE) does (Gensini et al. 2014). Though Gensini et al. found no correlation between the NARR surface-based CIN (CIN) versus the Denver radiosonde record (the only sounding site within the domain), for the time period of this study in the warm season a correlation coefficients of 0.36 for CIN, 0.67 for CAPE and 0.97 for PW were found. These correlation coefficients were nearly identical for the two nearby sounding sites, North Platte, Nebraska and Dodge City, Kansas. Albuquerque, New Mexico had comparable correlation with respect to CAPE and PW, but dropped to 0.11 for CIN, though still statistically significant using the Mann-Whitney U test at the 0.95 level. For all sites, CIN was compared using all days and only days with non-zero CAPE with no appreciable difference for all correlations.

4.3. Results

Over the period of study, May through August 2003 to 2015, just over 56,000 CI events were found with the peak found in July with 21,386 events and May with the least at just over 6,000 events. Fig. 4.2a shows that in the west sub-regions, the number of events climbs gradually across all regions from May to June, then south of CHY grows rapidly into July then subsides in Aug. While PAL is the leading region in all months, the number of events in the southern regions relative to those north of PAL grows through the season. In the east (Fig. 4.2b), although the pattern of increasing number of events until July then subsiding in August holds, the amplitude is not nearly as dramatic. PAL clearly has the largest number of events through June with RAT nearing in July then SOU overtaking PAL in Aug. The influence of the east-to-west ridgelines in the east sub-regions of CHY, PAL and RAT are clear in July and August with local maxima in these regions compared to the lower land to the north.

Fig. 4.3 examines the distributions of CI events binned by hour of occurrence, east or west sub-region, and by the state of the soil, wet or dry anomaly, at the CI point. In May and June, in especially in the east, it is clear in most regions that there is an early bias in CI events over wet soil versus dry soil. This is evident in every region at 1800 UTC where the number of CI events over wet soil is greater than the number over dry soil in May and June for every region. The relationship is not as evident in the west sub-regions, but is seen in the CHY and PAL regions in May. This is in sharp contrast to July, when there is little to no difference in the number of CI events at from 1600-1900 UTC, but the number of events over dry soil is greater later in the day at 0000 UTC, indicating a shift from an early bias over wet soils in the early months to a switch to a late bias over dry soils in July. This late bias holds into Aug, but is not as strong from these graphs.

Despite the early bias in June and May over wet soils in the east, there is no apparent bias in the total number of CI events over wet and dry soil in the east. In the west, from PAL southward, there is a clear bias of a greater number of events over wet soil, with the greatest difference in RAT. This continues in June, but is weaker, with only PAL, RAT and ARK showing the bias of more events over wet soil. July again sees a dramatic shift for a greater number of CI events over dry soil, in both west and east. The greatest difference is seen at the top of the peaks of the distributions, 1900-2200 UTC in the west and 2100-0100 UTC in the east. The bias of more CI events over dry soils continues in the east in August, but weakens in the west with some regions showing greater number over events over wet soil (ARK), no difference (NOR, PLT, PAL) and the rest with more events over dry soil still.

The months with the greatest number of CI events, July and August, also see the sharpest distributions, with a large proportion of the CI events at and near the mode, especially in the west. Earlier in the warm season, the distributions are relatively flat, with more similar number of CI events throughout the day, rather than being focused at greater numbers at high elevation near solar maximum.

Fig. 4.4 shows the difference, in hours, between the mean CI time over wet and dry soil and above minus below average EVI by region and month as well as west/east sub-region. Comparing these results to Fig. 4.3, we see the negative difference values in the east sub-regions, meaning earlier mean CI over wet soils versus dry soils. The mean CI time differences over wet and dry soils in June and July (Fig. 4.4b and c) in the east are nearly all statistically significant and with differences at roughly 30 minutes. This is far different than the response in May (Fig. 4.4a), where the greatest values are from PLT northward, and August (Fig. 4.4d), where the only significant values are from ARK southward show a large difference in the sensitivity of CI timing to SM at the beginning and end of the season. The west shows many fewer significant differences with only 7 significant differences versus 18 in the east, with most of the significant differences coming in August.

For EVI, similar to SM in June and July (Fig. 4.4b and c), the difference values in the east sub-regions are negative, meaning earlier mean CI over heavier than average vegetation, with the mean time difference at about 30 minutes in June and 15 minutes in July. In the southern regions in August (Fig. 4.4d), the response is similar to SM with large negative differences and statistically significant values in RAT and SOU. In the north in August, the differences in NOR, CHY and PLT are positive and significant in the eastern sub-regions. May (Fig. 4.4a) sees an even larger departure from the SM response, with none of the eastern sub-regions showing statistically significant differences. Rather, western sub regions in the central part of the domain (CHY, PAL, ARK and RAT) shows statistically significant positive differences.

4.4. Differences in Convective Variables by Over Anomalies of SM and EVI

This section examines the difference in mean values the convective variables CAPE, CIN and PW at CI points over positive anomaly and negative anomaly SM and vegetation in the form of EVI. Time of day, in four groups, 1800-2059 (18-21, early afternoon), 2100-2359 (21-00, later afternoon), and 0000-0259 (00-03, evening) UTC are arranged on the abscissa with region from north at the top to south at the bottom on the ordinate. West CI points are in the top plot and east on the bottom (note different scales in the color bar for east and west in both the difference and mean fields) with month from left (May) to right (August). Fig. 4.5 shows an example of difference plot for CAPE, June, with west sub-regions on the top and east on bottom. The center plots show the means for a given time of day and region of CAPE over wet soil. The right figures show the mean CAPE for a given region and time of day over dry soil. The left plot is the difference plot of center (wet soil mean) minus right (dry soil mean) featured in Figs. 4.6 through 4.17 with statistically significant values, at the 95% level, in bold color. The statistical significance between the distribution of convective variable values at a given point on the plot between those occurring over wet and dry soils is ascertained using the Mann-Whitney U Test.

Beginning with SM, overall in May, the trend is increasing values in the difference in the later months and in the east for both CI points and null points. For difference in CAPE over null points with above minus below mean SM (Fig. 4.6), the difference is nearly universally positive and significant in both the east and west, with greater difference values in the east in July (Fig.

4.6g) and August (Fig. 4.6h). For the difference over CI points (Fig. 4.7), May and June are very different from the null comparison. In the east in May (Fig. 4.7e), the values are sharply negative and largely significant from PAL northward and positive in RAT and SOU, while values are nearly all negative in the west as well, but only significant in CHY, PLT and PAL at 2100-0000 UTC. The difference in June at CI points shows negative, significant values scattered across both east (Fig. 4.7f) and west (Fig. 4.7b), with difference values increasing through the day with few significant values in the second two time periods. The difference values in July are more similar to the null values, especially in the west (Fig. 4.7c) with weaker but significant differences, mostly from PAL southward. While in the null difference, the greatest difference values were in the 1800-2100 UTC timeframe, the greatest differences in the CI point values (Fig. 4.7g) is in the 2100-0000 UTC time. In August (Fig. 4.7d and 4.7h) the difference fields are again similar between the null and CI point datasets with both difference fields showing nearly universal positive, significant differences throughout the east and weaker differences in the west.

For CIN, the difference in the null points (Fig. 4.8) between wet minus moist soil shows a similar pattern throughout the months in the east, with all nearly all difference values positive, meaning less inhibition over wet soil, and greater values in the first and third time period. In May in the west for null points (Fig. 4.8a), the differences are similar to those in the east, with the greatest difference early and late. Again, May shows the largest departure in the CI point differences from the null case, with nearly no difference in the west (Fig. 4.9a) and the only positive significant differences from PAL northward in the east (Fig. 4.9e). In the west in June, there is little to no spatial or temporal pattern in either the CI (Fig. 4.9b) or null (Fig. 4.8b) point differences, with a few significant differences early in both cases and little difference afterwards.

In the east, July (Fig. 4.9g) shows the most similarity to the null point difference (Fig. 4.8g), with nearly all positive significant differences and the weakest difference in the 2100-0000 UTC timeframe. June (Fig. 4.9f) and August (Fig. 4.9h) also have a large number of significant, positive differences, but show a decreasing number of significant differences in the 0000-0300 time period, with both months showing a greater number of positive, significant differences than the null point differences.

For PW, the difference in the null points (Fig. 4.10) between wet minus moist soil shows a similar pattern to the previous variables in the east, with all nearly all difference values positive, meaning less inhibition over wet soil, and greater values in the third time period. In the west, the difference values and significance values are stronger from ARK southward. Compared to the null point differences, the CI point differences show the greatest difference in the bookend months, with May showing significant, negative values in the east (Fig. 4.11e) north or PAL, similar to the CAPE pattern (Fig. 4.7e) and few significant values in the west (Fig. 4.11a), but negative. June differences at CI points bear more similarity to the null point case. In the west (Fig. 4.11b), there is a greater number of significant positive differences in the CI point case than the null, while in the east (Fig. 4.11f) the number of significant cases is greatly reduced compared to the null with the strongest response in the 2100-0000 UTC timeframe. In July CI point differences are very similar to the null point differences, with a large number of significant positive differences, with the strongest result in from ARK southward and in the 0000-0300 UTC timeframe. August shows a large decrease in the number of significant values in both west (Fig. 4.11d) and east (Fig. 4.11h) with positive difference values in SOU in both cases and early in the west and late in the east.

The same analysis is conducted for EVI as for SM above. In May, in the east, the response at null points is nearly identical to the response in in the SM null points difference plot (Fig. 4.6f to h) with nearly all significant positive difference values in June through August (Fig. 4.12f to h). Unlike the SM response, the difference in May in the east shows little significance and no coherent pattern across space and time (Fig. 4.12e). In the west (Fig. 4.12a), May again shows little spatial coherence, with significant positive difference in PAL and SOU and a mixture of negative and positive significant values elsewhere. June through August sees an increase month to month of significant positive difference values, concentrated in the south in June and July (Fig. 4.12b and c), then from PAL northward and in SOU in Aug (Fig. 4.12d). Difference values at CI points in the west show few significant values in May (Fig. 4.13a) and June (Fig. 4.13b), with May showing positive significant values in the north early and late in the south. June sees negative values early, positive values in the 2100-0000 UTC time then little difference late. July (Fig. 4.13c) sees nearly all positive, significant values in a jump in count over the null points difference. August (Fig. 4.13d) has little significant difference, only in the middle time period. In the east, in May (Fig. 4.13e), there is a large departure from the null points with positive significant difference in most times and regions. June (Fig. 4.13f) also sees a large difference from the null points, here with almost no significant difference throughout. In July in the east (Fig. 4.13g) nearly all positive significant differences in the 1800-0000 UTC time, with only ARK southward in the final time period. August (Fig. 4.13h) sees nearly all significant positive differences from 2100-0300 UTC.

The EVI null points difference for CI is similar to that for SM in the east sub-regions (Fig. 4.14 e to h) in that the strongest positive significant difference pattern is found in the 1800-2100 and 0000-0300 UTC timeframe with a weaker difference in the middle time period.

Compared to the SM null points there are fewer and smaller significant differences in the east for the EVI case. In the west, the opposite is true, with more and larger significant differences throughout, mostly positive. May, July and August (Fig. 4.14a, c, and d) have nearly all positive, significant values throughout. June (Fig. 4.14b) stands out as having almost no significant values and many negative, but not statistically significant values throughout. Difference values at CI points show a large decrease from those at null points in the west, much larger than the decrease in the SM case. May and June (Fig. 4.15a and b) difference values in the west show almost no significant values, with June showing a pattern of negative values in the 0000-0300 UTC time. July and August (Fig. 4.15c and d) see an increase in positive significant values, primarily from 1800-0000 UTC, with July again showing a large number of negative values in the 0000-0300 UTC timeframe. In the east, in May (Fig. 4.15e), numerous negative significant values are found from PAL northward, otherwise, there is little difference. In June through August (Fig. 4.15 f to h) there are a large number of significant positive values from 1800-0000 UTC.

For PW, the difference values at null points with regard to EVI (Fig. 4.16) are very similar in the east sub-regions compared to the differences over anomalously wet and dry SM points (Fig. 4.10), with nearly all positive, significant values, except for May (Fig. 4.16e) which sees positive significant values mainly from PAL southward. Whereas the pattern in the west with regards to SM was similar to the east for PW, the pattern in the west with regards to EVI sees a large decrease in difference values. The pattern in May, June and August (Fig. 4.16a, b, d) is similar, with significant positive differences mainly confined to SOU and NOR and the final time period. July (Fig. 4.16c) sees even fewer significant differences with only positive differences in SOU and the final time period. For differences in PW in western sub-regions values over positive and negative anomaly EVI values at CI points, outside of May (Fig. 4.17a), which sees a few significant values from ARK southward after 2100 UTC, there are more significant values compared to the differences at null points. June (Fig. 4.17b) sees significant positive values, mainly from PLT southward and after 2100 UTC. July (Fig. 4.17c), on the other hand sees most significant positive values before 2100 UTC and from RAT and SOU. August (Fig. 4.17d) sees significant positive differences, mainly before 0000 UTC. The east sees a large increase in significant difference compared to the west, with May and June (Fig. 4.17e, f) seeing the most significant positive differences, throughout most times and regions. July (Fig. 4.17g) sees a decrease with significant differences from PAL southward and before 0000 UTC. August (Fig. 4.17h) sees significant positive differences clustered from ARK southward and after 0000 UTC.

It is clear that, in the great majority of cases, the value of the convective parameter at above mean SM and EVI points is more favorable for convection, for both null points and CI points. For the null points cases, the difference plots for both CAPE and PW over both SM and EVI differences, follow very similar patterns, apart from May, with nearly all positive significant differences in the eastern sub-regions and nearly all positive differences in the west as well, but less difference and significance, especially in the northern sub-regions. The difference at CI points shows very different patterns in May and June in the SM difference plot with numerous negative and significant values. Otherwise, the difference over CI points shows a decrease in the number of significant sub-regions, and usually a stronger decrease in the difference value at higher elevation in the west. This means that at most points and times in the region, higher warm season daytime CAPE and PW values tend to occur with higher SM values and greater vegetation cover. At times and points at which CI is occurring, the relationship is weaker, especially with regards to SM in the early warm season.

The difference is CIN at null points is similar for both SM and EVI cases in the east, but in the west, except for June, there are far more pervasive positive significant differences, indicating that lower inhibition at points where CI does not occur is concurrent with greater vegetation levels, while there is no relationship associated with high or low SM at null points. At CI points, especially in the west, there is almost no relationship between CIN and EVI, with little difference and significance. The relationship with SM is much more similar to the null case with prevalent positive, significant differences throughout.

This section shows that, while it is often the case that more favorable conditions for CI tend to occur over moist soil, this is not always the case, especially at CI points. The response over differing SM and EVI conditions does not always move in the same direction. The next section explores a method to examine the overlaying state of convective variables in the context of covarying SM and EVI conditions.

4.5. Patterns of Convective Variables over Covarying SM and EVI Anomalies at CI Points

A method similar to the contingency table is used to explore the state of overlaying atmospheric variables at points of CI as the underlying state of the surface, near-surface SM and vegetation state, covary. Fig. 4.18 shows an explanation of the plot.

Beginning with CAPE in Fig. 4.19, there is great similarity between May and June, with both east and west in both months exhibiting the highest value in the -/+ SM/EVI quadrant. All but the east in June exhibit a top heavy (top two quadrant averages are +/+ and -/+ SM/EVI) figure with the lowest value in the +/- quadrant. July and August are also similar, with all but

August in the west exhibiting a pattern of +/+ with the greatest value and -/- with the smallest. August does show the +/+ with the greatest value, but there is relatively little difference between quadrants outside of this.

Overall, while June has the highest average CAPE across quadrants, this month has the least relative difference across quadrants in the east, while the same can be said of August in the west, though it has the second lowest CAPE values after May. The greatest ratio of standard deviation to mean (sd/mean) ration is found in May followed by August, with a greater sd/mean ratio in the west in August and in May in the east. Overall, there is a greater sd /mean ration in the west than in the east.

Looking at the plot CIN in Fig. 4.20, it is clear from a quick examination of all plots that there is 1) a more universal pattern throughout of greater inhibition associated with CI events over dry soils and less over moist soils in both east and west 2) less statistical significance between adjacent quadrants in the west 3) less sd /mean ratio in the west.

Except for May, in which the lowest inhibition is found in the +/- quadrant in both west and east, the lowest inhibition in all other months and sub-region is found in the +/+ quadrant. In all months and sub-region, the plots are right side heavy, or exhibit higher values on the right side of the plot associated with below average SM. While the lowest inhibitions are found in the +/+ quadrant, the converse of the highest being in the -/- quadrant is not universal. In five of eight months/sub-regions, the greatest CIN is found in the -/+ quadrant, but is found in both east and west in August.

The seasonal cycle of PW, with low values in May increasing in June and at a maximum in July and August is seen in the color shading in Fig. 4.21. Like CIN, there is a near universal pattern between PW over SM and EVI anomalies driven primarily by SM anomalies and secondarily by EVI again. Higher PW values are found on the left side, positive SM, of the plot in all but on plot (May, east where the maximum is found over -/+ SM/EVI. Of these seven left-side heavy plots, 6/7 have the highest PW value over +/+ SM/EVI. While the difference in mean values is relatively small compared to the difference in CAPE and CIN values, the statistical significance between quadrants of each plot is greater than found in the CIN plots, primarily due to the relatively low standard deviation in the PW data.

4.6. Comparison of CI Characteristics on MCS and non-MCS days

Utilizing the MCS days from the climatology formed in Chapter 2 of this dissertation, a comparison is made between the characteristics of the CI, including time of occurrence, longitude, size and maximum precipitation rate, as well as NARR derived 500-850 hPa wind shear, CAPE, CIN and PW at the point of CI. Fig. 4.22 shows individual plots for each variable, with data broken down by month as well has for all months combined on the far right. Timing of CI reflects the results of Figs. 4.3 and 4.4 with earlier CI over moist soils. All differences between non- and MCS days show statistical significance, with the greatest differences over moist soil coming in May and June and June and August over dry soil. For all times, the difference over moist soil is greater. For mean longitude of CI, it is nearly universal that CI on MCS days occurs further west than on non-MCS days. Large differences are found over moist soil in July and August, while overall, the difference is greater over moist soil than dry.

Examining characteristics of the CI footprint, for the size of the initial CI object, in number of Stage IV grid points, in all cases, moist and dry, the size is greater on MCS days versus non-MCS days. Apart from May, when the size is greater over dry soils, the size is greater over moist soils in all other months with the largest initial CI objects in June. For all times, CI objects over moist soils were greater in size and the difference between non- and MCS days was slightly greater. Maximum precipitation rate, highest precipitation rate grid point with the CI object, shows little relationship between non- and MCS days and between under laying soil condition, with a slight advantage over moist soils in the total. The total precipitation rate follows a similar pattern to size with greater values over moist soils from June onward and in the total. CAPE correlates well with size and total precipitation with highest values in June, high values over dry soils in May and lower values over all in July and August, leading to slightly greater CAPE over moist soils at non- and MCS day CI points. For CIN, the results are slightly counter-intuitive, with the totals showing greater inhibition at MCS day CI points, while for individual months, the values bounce between higher and lower CIN at MCS day CI points. PW ends with significant differences between non- and MCS days over dry soils in 3 of 4 months and in the total, with the totals reflecting higher PW on non-MCS days, but similar totals across the values for the total.

4.7. Discussion and Conclusion

A variety of methods and datasets were used to study the impact of two land surface characteristics, near surface SM and vegetation cover, on CI in the central Front Range of the US Rocky Mountains and the adjacent high plains to the east. This area of study was broken up into seven sub-regions based on the presence of east-to-west ridgelines known to influence CI. These seven sub-regions were then split into east and west to capture the differences in CI in the higher terrain to the west versus that over the plains to the east. CI points were derived from the Stage IV hourly precipitation dataset as at initial occurrences of at least two adjacent grid points at greater than 2 mm/hr rain rate.

First the mean timing of CI was examined in context of elevation (west and east) and anomalously low and high SM, derived from the offline land surface model derived NLDAS-2 dataset, and vegetation cover, approximated by the MODIS retrieved EVI. Timing of CI with respect to SM anomaly presented a consistent relationship across regions and months with earlier mean CI over wet soils versus dry soils. The mean difference was greater in the east at low elevations than to the west. In the east, the number of significant differences was greatest in June and July, with all but the northernmost region being statistically significant. In May, there was a large difference in the north, decreasing southward with no significance from ARK region southward. This, as opposed to August, which only saw significance in the southern regions of ARK and SOU. In the west, there were no significant differences in May, with only a handful through the rest of the season, peaking with 3 regions showing a significant difference in August. In nearly every case, the difference was greater between CI events over the wettest quartile and the driest quartile soil, indicating that convection tends to occur earlier (later) the more anomalously wet (dry) the soil is. The same analysis with EVI revealed a consistent, but weaker trend in the east in June through August, with earlier CI over more heavily vegetated areas and earlier in the south in August. The large departure between timing of CI between SM and EVI was in May, where, for both west and east, earlier mean CI was associated with more sparsely vegetated areas.

Examining timing of CI, binned by hour of occurrence by month and region as well as the state of the underlying SM anomaly, the shift in distributions of CI over wet and dry soils in May, with peak CI occurring 1-2 hours earlier over wet soils in the northern regions in the east, is clear. In June and July, while there are a few instances of notably earlier CI start over wet soil, the large difference in mean CI time is mainly attributable to far larger number of CI events over dry soil late in the day. This is also demonstrated in August over high terrain to the west in CHY and PLT, where the number of CI events is nearly identical over wet and dry soil through early afternoon, but continues to grow over dry soil in a later and greater peaking distribution, leading to significant differences in mean CI time. For EVI, while the distribution for CI events over positive anomaly EVI are nearly always greater than for negative in May, there is a far greater difference later in the day, leading to the significant differences in east and west.

To gain an understanding of the relationship between the land surface and coincident state of the atmosphere at CI points, the NARR-derived CAPE, CIN and PW at CI points with above and below average SM and EVI were compared. First, the atmospheric variables were binned by region and 3-hour time period from 1800 to 0300 UTC in two groups for above and below mean SM and EVI. The difference in the means of these two groups and the statistical significance, attained with the Mann-Whitney U test, was shown in bold for cases meeting at least the .95 level. For both SM and EVI it is clear that the majority of differences in mean values between variables over wet and dry soil are positive and that most significant values are positive. For SM, 44% of time/region blocks across all three variables were statistically significant compared to 35% for EVI (290 and 232 cases of 672 respectively). Of these 290/232 cases for SM/EVI, only 32 and 44 were negative differences of mean values with statistical significance with a large proportion of these being for PW in May.

Looking at time of day, the time period with the greatest number of positive significant differences tended to be later in the day, this tendency being stronger for SM than EVI and in the east in the variables CAPE and CIN. Likewise, the time period with the least mean difference and greatest number of significant negative differences tended to be earlier in the day, with the strongest relationship coming from CAPE for both SM and EVI. It is clear that there is a consistent decrease in variable magnitude in the last time period, the evening, over dry soil. This signals that, on average, situations that have higher SM and EVI at the start of the day tend to maintain more favorable atmospheric variables for convection through the evening while CI over dry soil late occurs in more conditions with more marginal convection parameters.

Examining regional patterns of significance, for PW in the east, there is a definite pattern of larger numbers of significant positive values in the southern half of the domain for SM throughout the season and EVI in July and August. This relationship holds for CAPE and SM though not in June. For CIN and SM, the pattern switches from strong positive, significant values in the north in May, to the south in June then no spatial pattern in later months. In the west with relation to SM, there is no spatial pattern throughout for PW. For CAPE, there is a relative lack of significant differences in the middle regions of PLT and PAL. For CIN, there is a tendency for more significance in the southern regions in June and August, but no pattern in May or July.

The impact of the covariance of SM and EVI anomalies on overlaying atmospheric variables at the point of CI was explored using a method similar to the contingency table was employed. For times and regions, CAPE provided the most interesting interplay between SM and EVI, with the -/+ SM/EVI quadrant associated with the highest mean CAPE in May and June, with July and August showing high CAPE over the +/+ quadrant and lowest over the -/- quadrant at for both east and west. CIN and PW were more consistent through the months, with CIN seeing a pattern of low values over high SM and high values over low SM, with EVI modulating the relationship in May and June and having nearly no apparent effect in July and August. For PW, there was a consistent occurrence of the highest PW associated with the +/+

sector in the west and the lowest value in the east associated with the -/- sector with generally higher mean values associated with anomalously high SM.

Examining the covarying relationship of SM and EVI anomalies to overlaying atmospheric variables associated with moist convection through time of day, For CAPE, in the west, from 2000 UTC onward there is a consistent relationship of high EVI associated with high CAPE values ("top-heavy" relationship) with SM modulating the response with higher CAPE over dry soils in May and June and over wet soils in July and August. In the east, July and August show a +/+ (-/-) SM/EVI associated with the highest (lowest) mean CAPE. May and June see the highest CAPE value at all times in the -/+ quadrant and the lowest most often in the -/- quadrant. Overall, the pattern for CIN in the east is less inhibition over above mean SM on the left side of the plot throughout times and month, with the weakest difference between means in early evening. This pattern is found in the west from 1800 to 2100 UTC with comparable statistical significance to the pattern in the east, weakening through early evening and evening to little difference between quadrants. For PW, as could be inferred from the time/region diagrams in Figs. 5.9 and 5.12, outside of May the relationship is fairly straightforward with left side/high value throughout most months and time periods in both west and east. May on the other hand has no consistent pattern in the west, in the east there is consistently high PW associated with the -/+ SM/EVI quadrant.

Future work includes expanding beyond the Front Range of the central Rocky Mountains to other parts of the CONUS to study the impact of varying SM and vegetation on CI in concert with changes in atmospheric variables. The construct of this study, utilizing hourly, roughly 5 km grid spaced precipitation data makes it difficult to expand this study outside the US, though the GLDAS-2 precipitation and SM along with MODISEVI for vegetation could be utilized with appropriate caveats. While this study only looked at the uppermost layer SM, examining the interaction of different vegetation and soil types with deeper layer SM should be examined. A modelling study, similar to Burghardt et al. (2014), in which several cases of CI focused on different regions of the Rocky Mountains and high plains, including MCS days and non-MCS days are simulated at cloud-permitting horizontal grid spacing. The SM and or vegetation would be raised and lowered to test the sensitivity of CI and subsequent MCS formation on land surface parameters. This modelling study would be useful in understanding factors governing CI that are not possible in an observed-data only study.

4.8. Figures

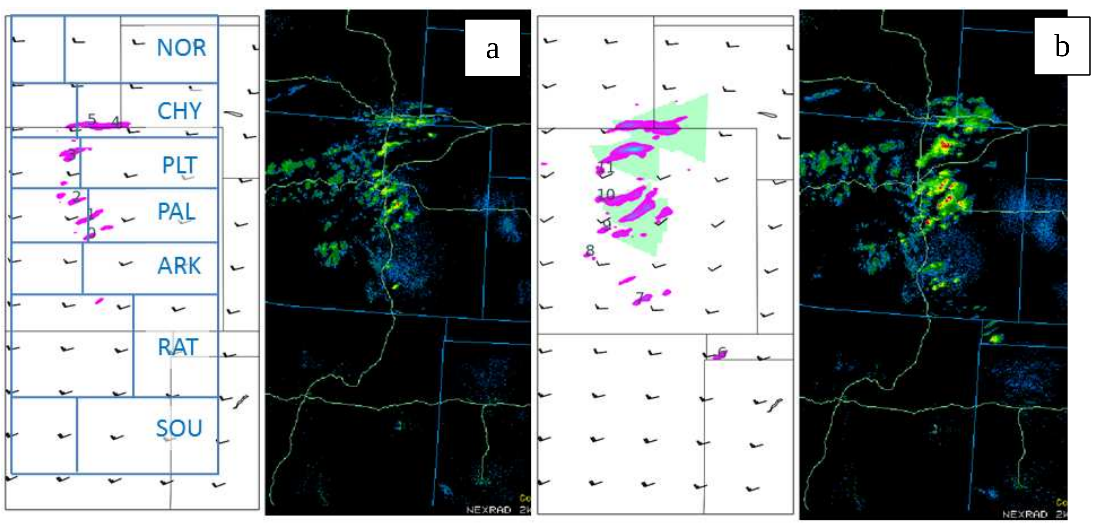

Figure 4.1. Example of the CI event detection algorithm. (a) shows the initial detection of 5 objects at 1900 UTC in Colorado on 3 June 2008. (b) shows the detection of 5 more objects (6-10) . The green triangular objects are masks, in which new CI events cannot be detected, based on the points in (a) and the 600 hPa NARR wind field (shown in barbs). The regions used in the study are outlined in (a).

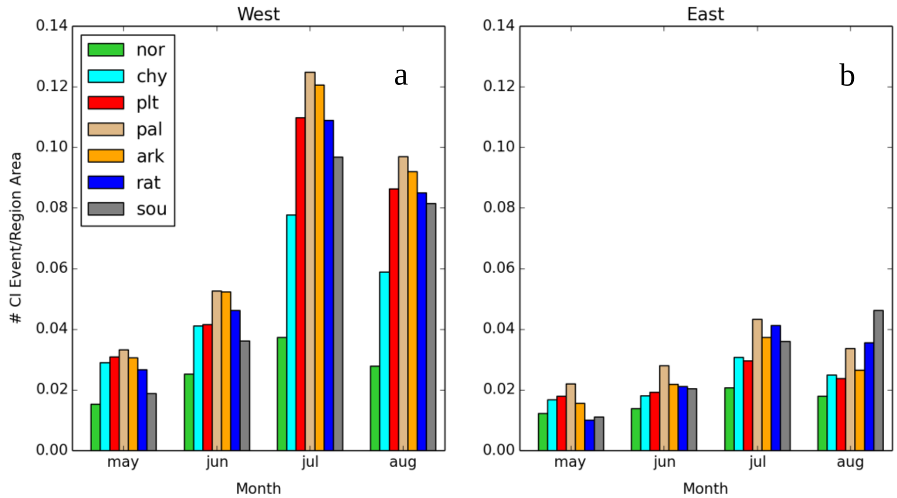

Figure 4.2. Total CI events, normalized by the area of the sub-region for the (a) west sub-regions and (b) east sub-regions.

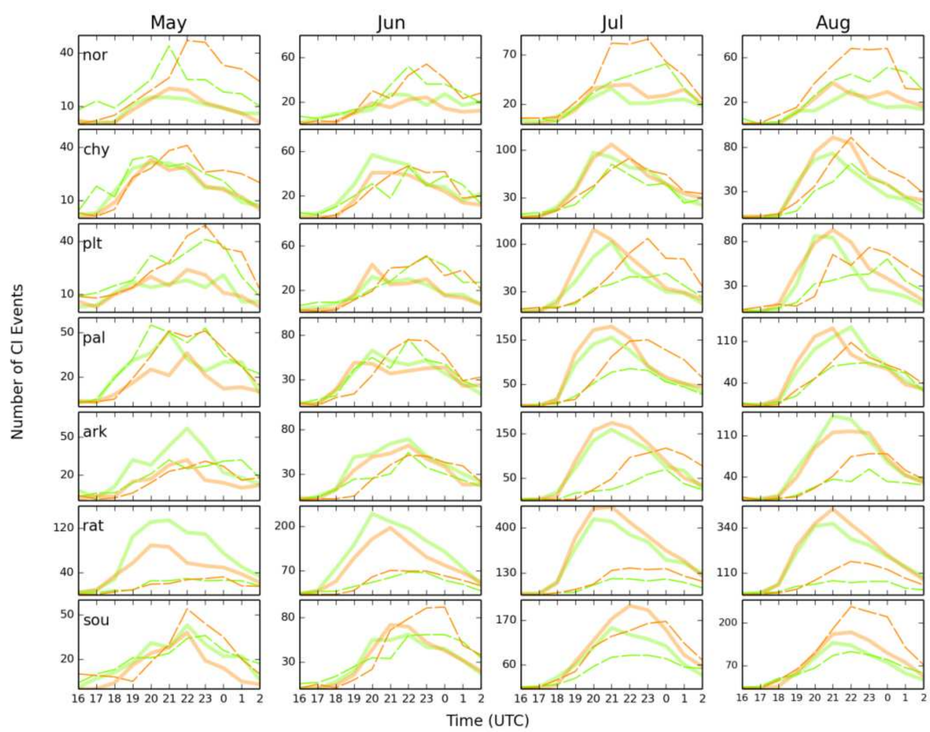

Figure 4.3. Distributions of the number of CI events by month (May through August, left to right) by time of day on the abcissa. The wide lines are numbers of CI events in the west with number of events in the east represented by thin, dashed lines. Green lines represent the number of CI events over wetter than average soil, while tan represents the number of CI events over dry soil.

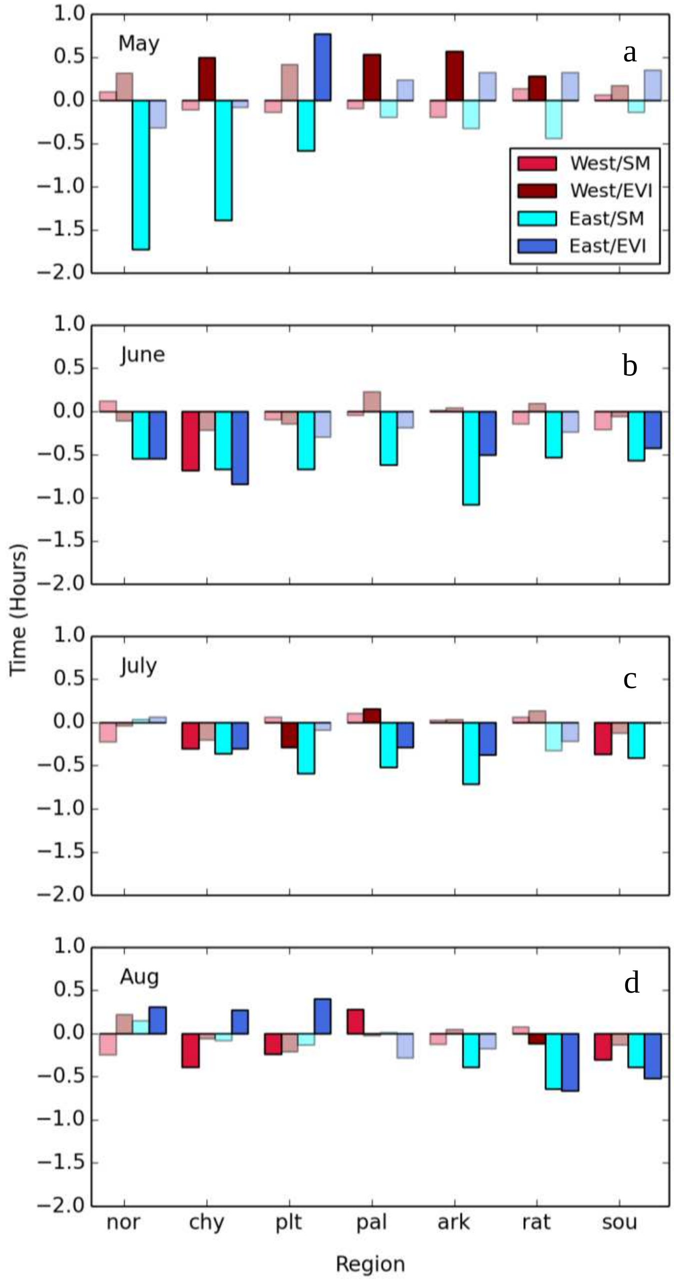

Figure 4.4. Time difference (hours) of mean CI event times over wet soils minus mean CI times over dry soils and for mean CI time over above average EVI minus below average EVI by month and by region. For each region/month, there are four bar graphs, representing SM time differences for the western sub-region (red), EVI difference time differences in the western sub-region (dark red), SM time differences in the eastern sub-region (cyan) and EVI time differences in the eastern sub-region (dark blue). Statistically significant values are in bold.

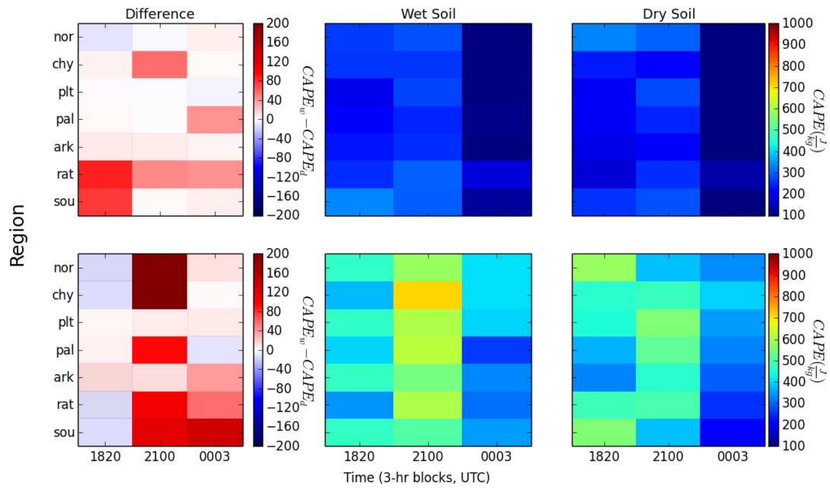

Figure 4.5. Example of difference plot for SBCAPE, July, with west subregions on the top and east on bottom. The middle plots show the means for a given time of day and region of SBCAPE over wet soil. The right figures show the mean SBCAPE for a given region and time of day over dry soil. The left plot is the difference plot of middle (wet soil mean) minus right (dry soil mean) featured in Figs 8 through 13.

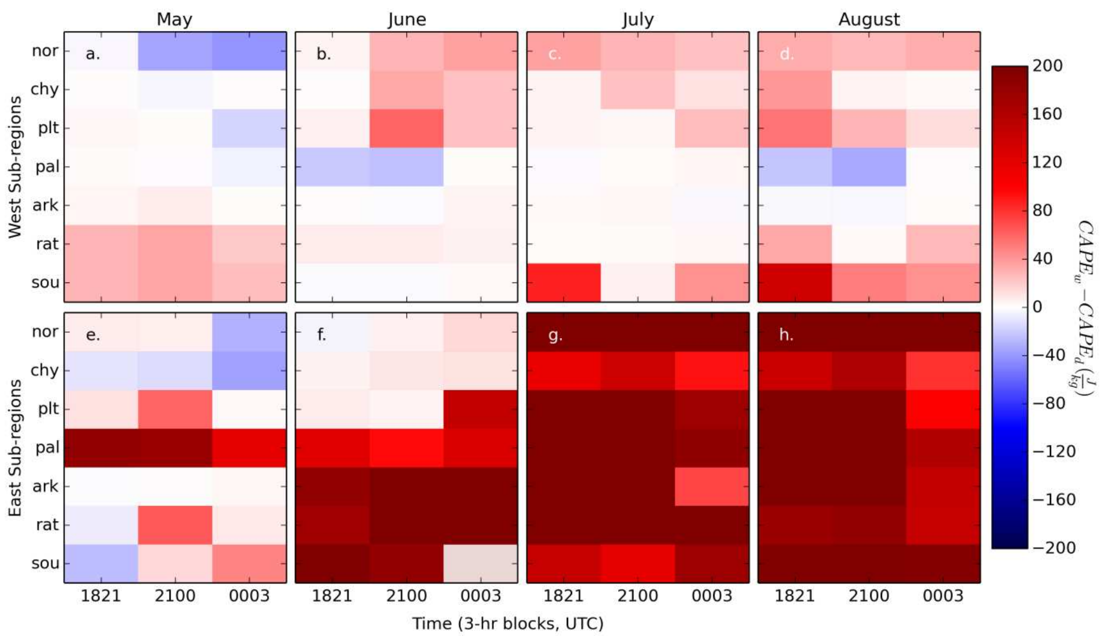

Figure 4.6. Difference in mean SBCAPE over anomalously wet minus dry soil at null points with west (east) subregions on the top (bottom), May on the left ((a) and (e)) through August on the right ((d) and (h)). Bold colors indicate statistical significance at the 0.95 level between the distributions over wet and dry soil.

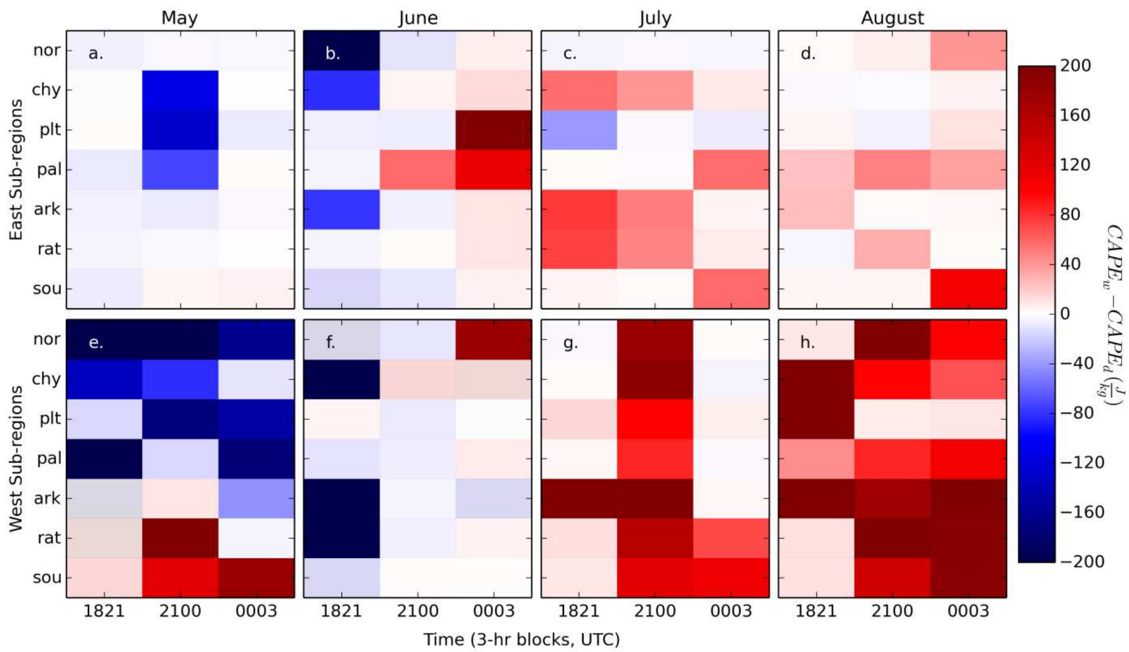

Figure 4.7. Same as Fig. 4.6 but for SM difference of SBCAPE at CI Points.

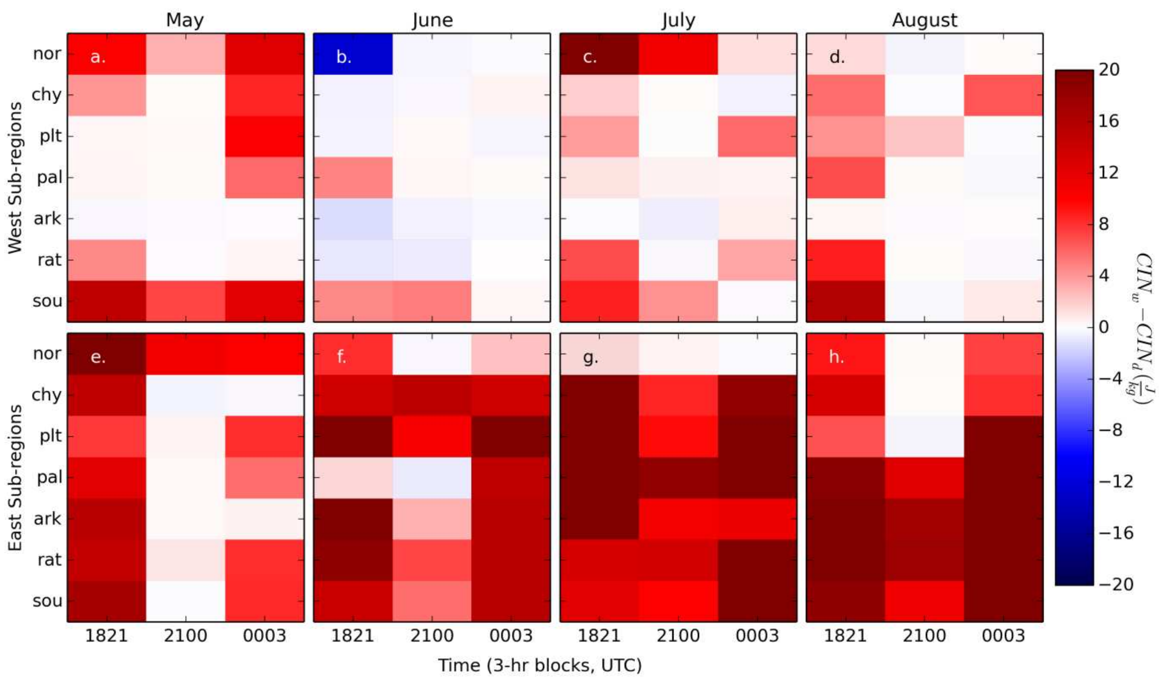

Figure 4.8. Same as Fig. 4.6 but for SM difference of SBCIN at null Points.

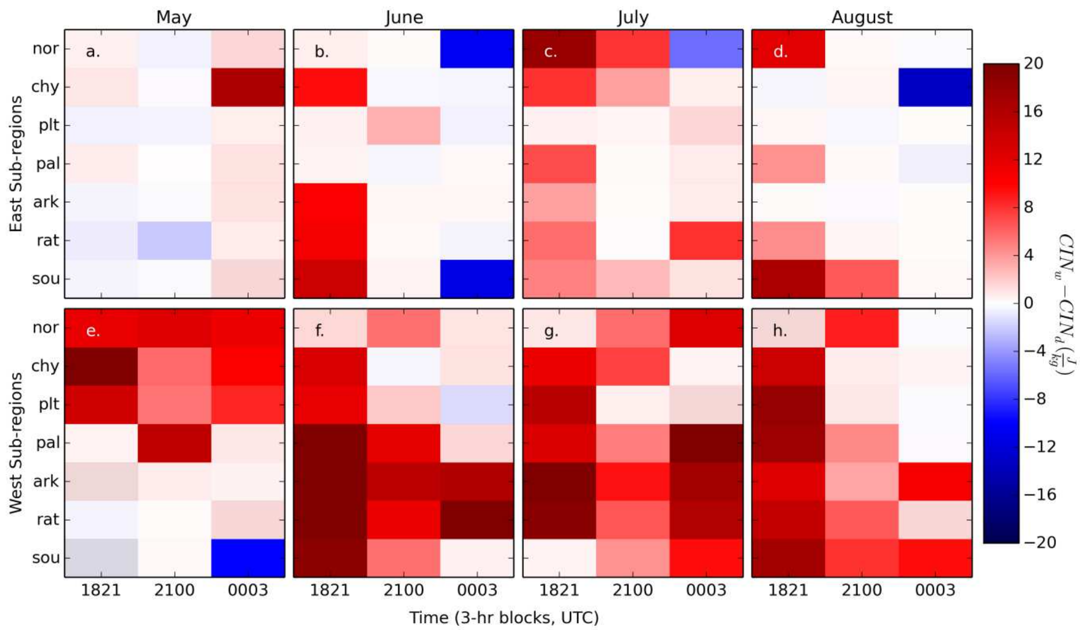

Figure 4.9. Same as Fig. 4.6 but for SM difference of SBCIN at CI Points.

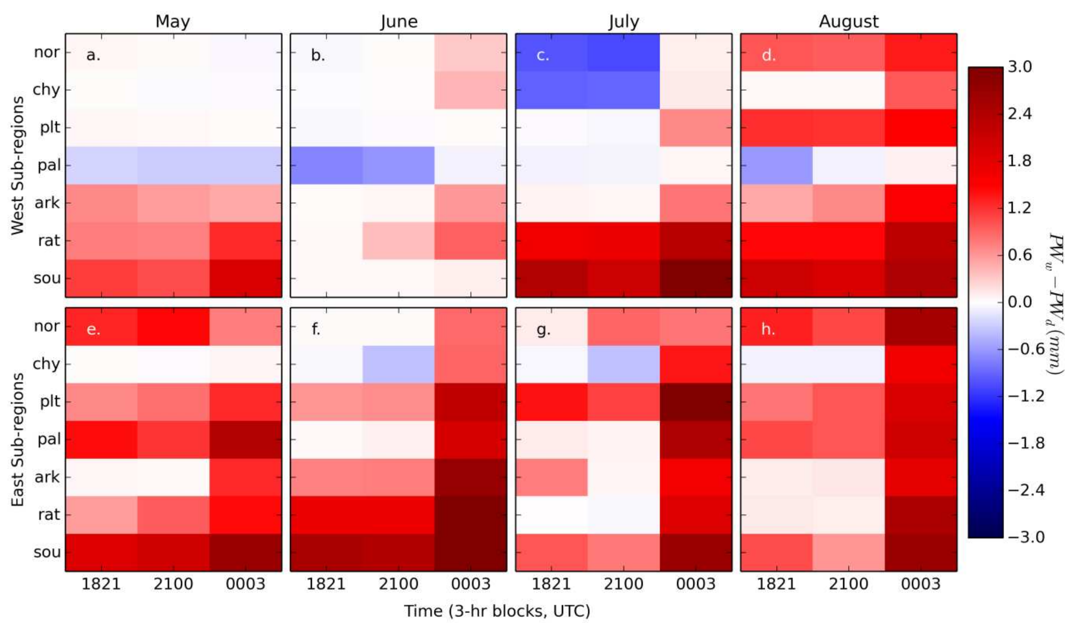

Figure 4.10. Same as Fig. 4.6 but for SM difference of PW at null Points.

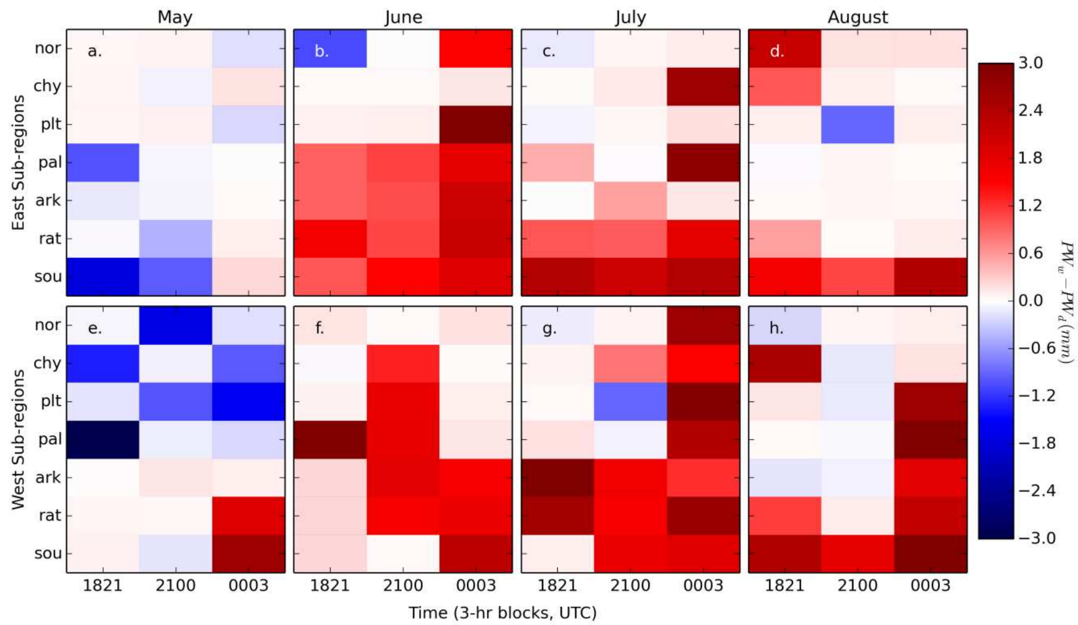

Figure 4.11. Same as Fig. 4.6 but for SM difference of PW at CI Points.

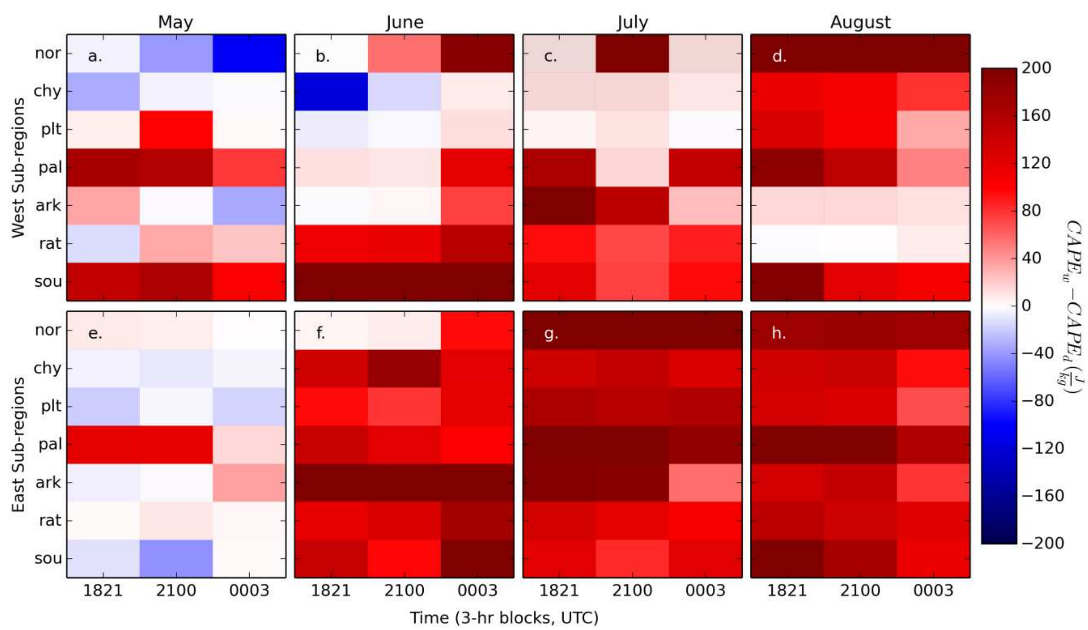

Figure 4.12. Same as Fig. 4.6 but for EVI difference of SBCAPE at null Points.

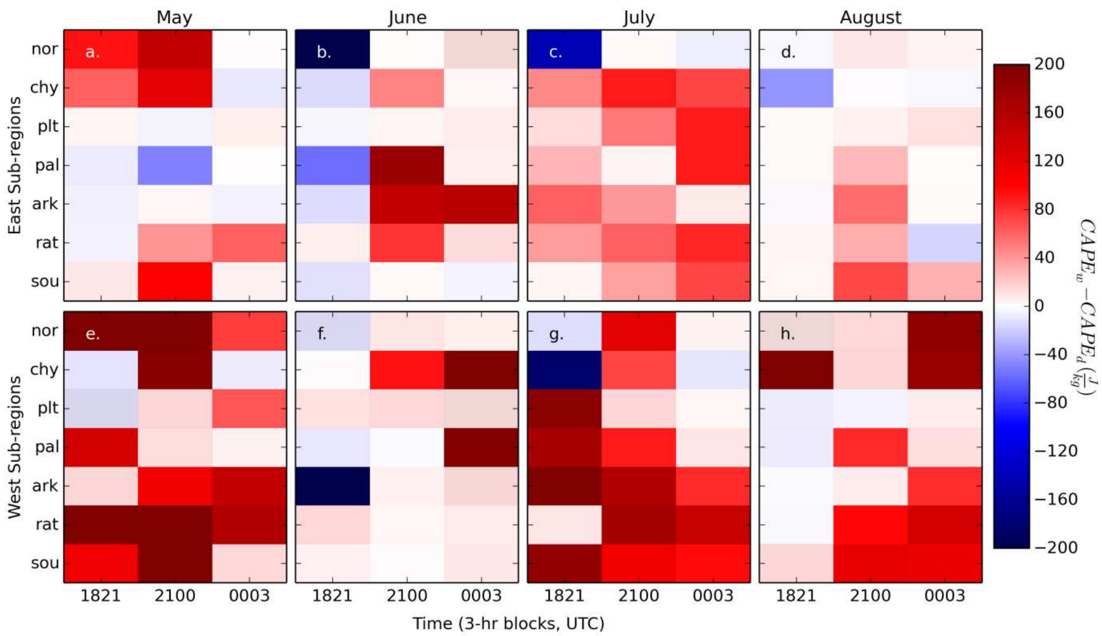

Figure 4.13. Same as Fig. 4.6 but for EVI difference of SBCAPE at CI Points.

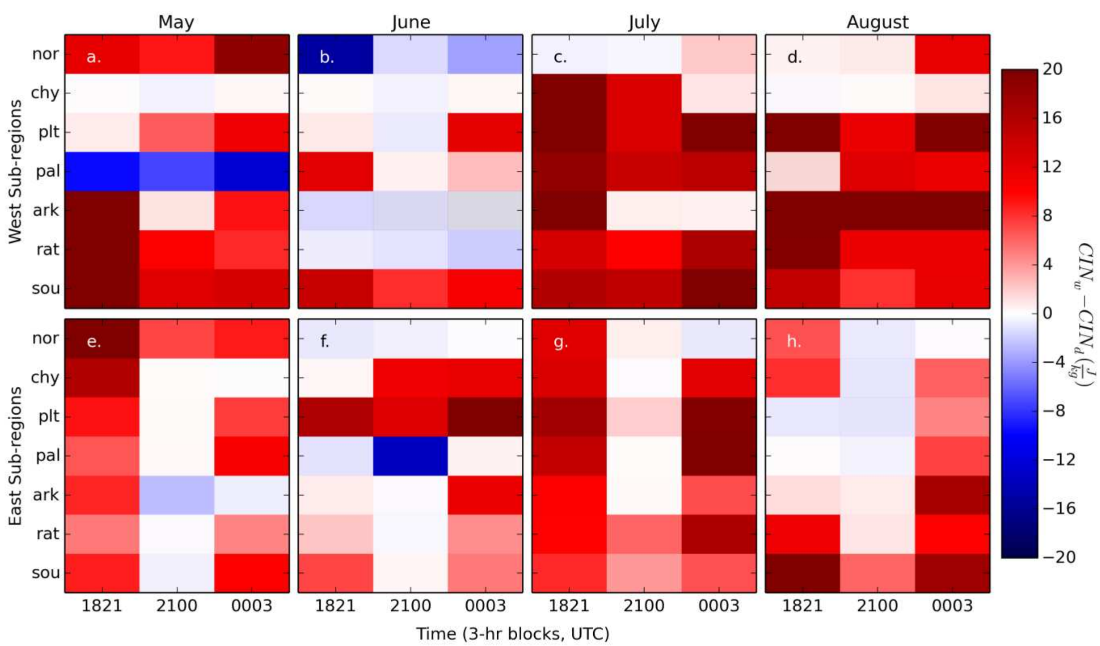

Figure 4.14. Same as Fig. 4.6 but for EVI difference of SBCIN at null Points.

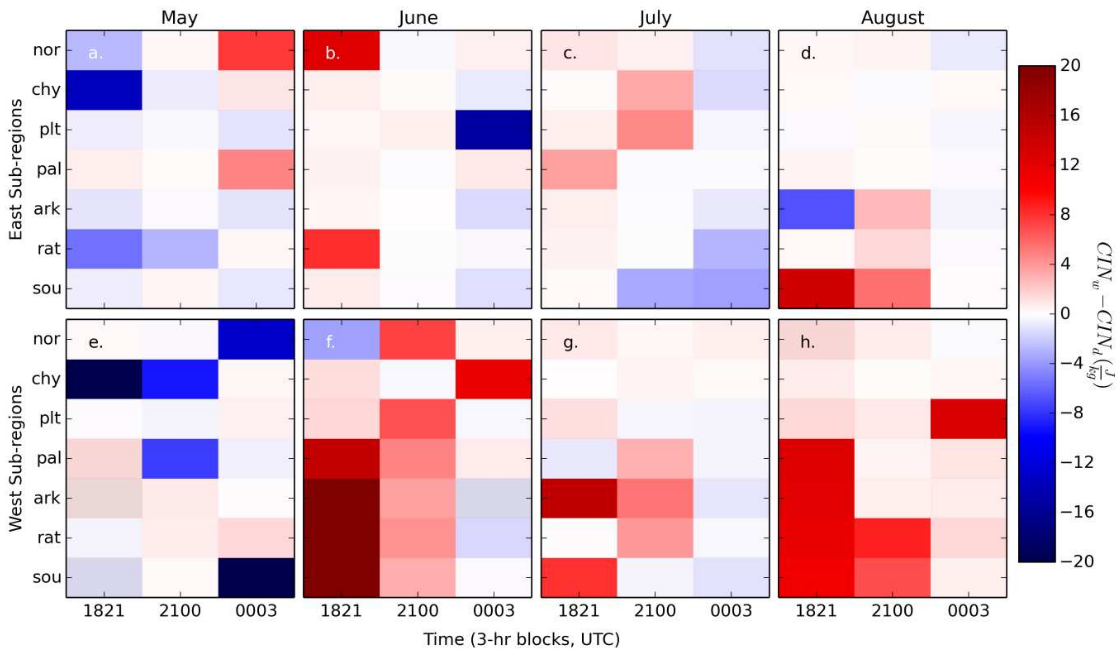

Figure 4.15. Same as Fig. 4.6 but for EVI difference of SBCIN at CI Points.

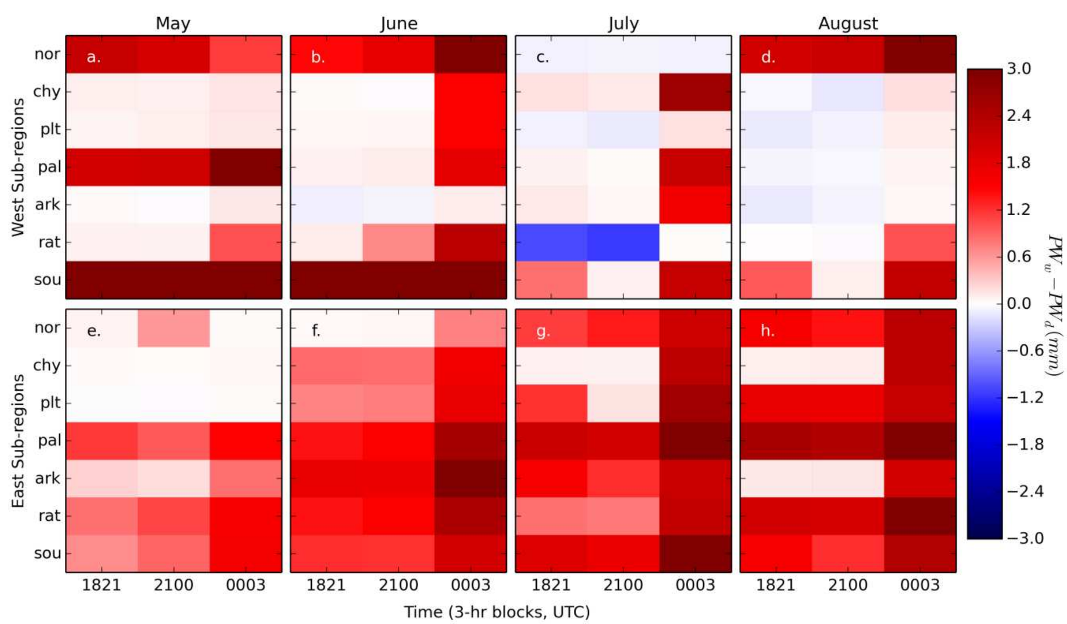

Figure 4.16. Same as Fig. 4.6 but for EVI difference of PW at null Points.

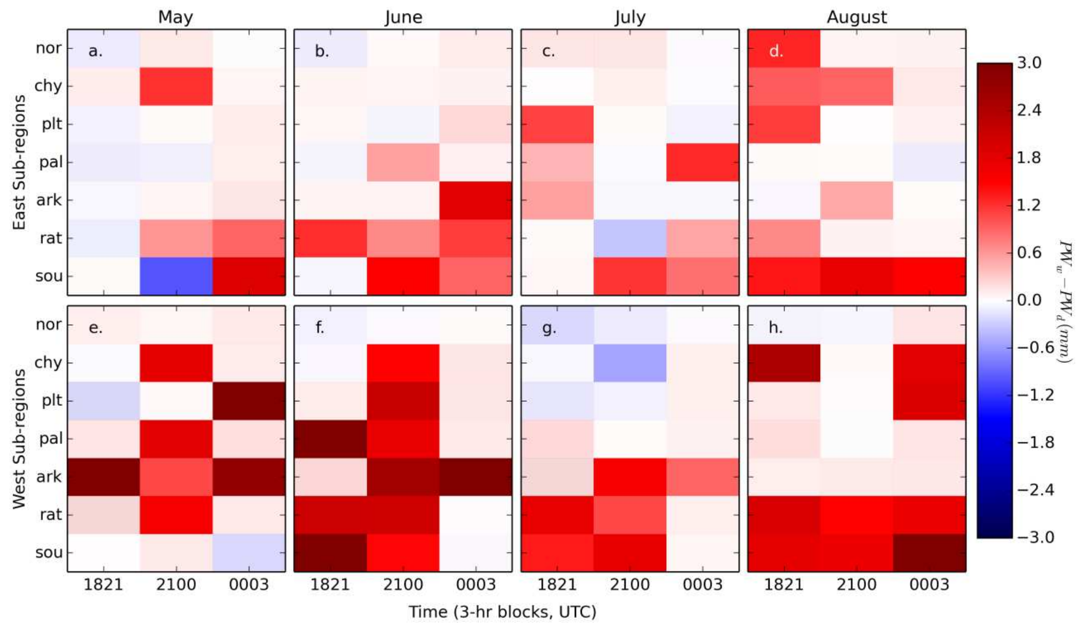

Figure 4.17. Same as Fig. 4.6 but for EVI difference of PW at CI Points.

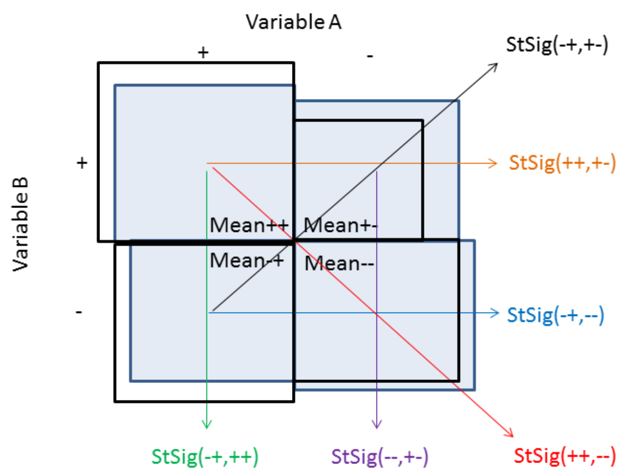

Figure 4.18. Example of the contingency table approach to examining the covarying relationship of two variables (Variables A and B on the top and left) with a third. The size of the color-filled squares represents the mean of the variable relative to the individual table. The filled color represents the value relative to all values of the variable across months for a given sub-region (i.e., east or west), with warm (cool) colors representing above-average (below-average) values. The black outlined square represents the standard deviation of the variable for the quadrant. Statistical significance (measured with the Mann-Whitney U test) is tested between all adjacent squares and plotted at the bottom and right of the plot. Significance at the 95% level is highlighted in red text.

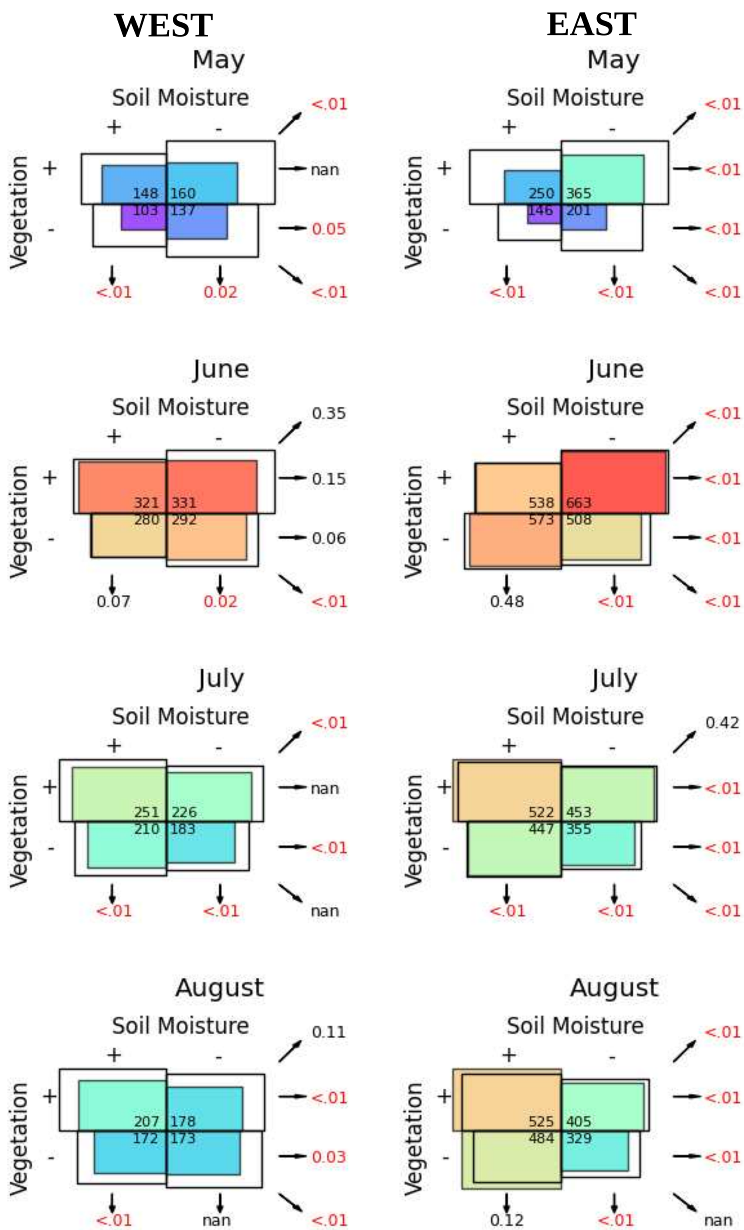

Figure 4.19. Table diagrams for SBCAPE for the west sub-region (left) and east sub-region (right).

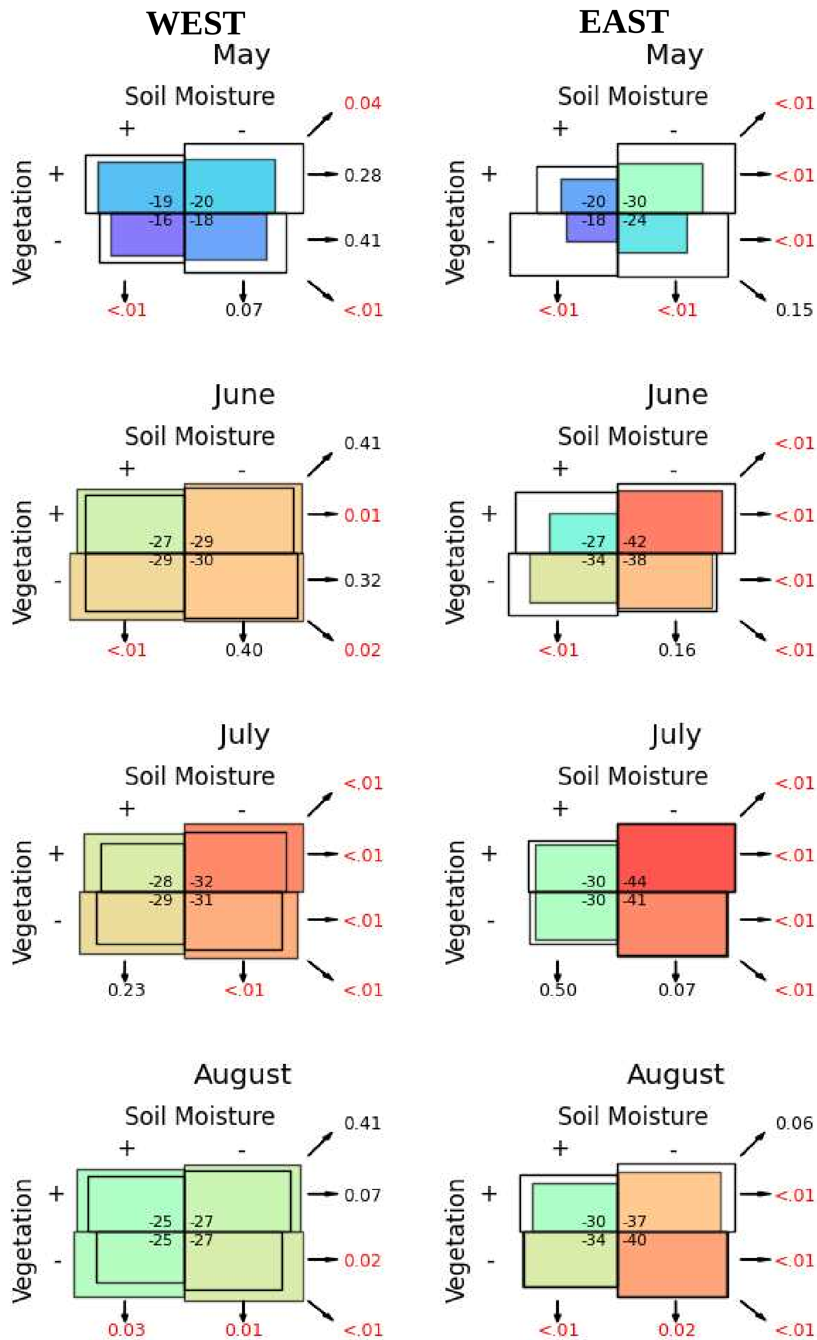

Figure 4.20. Table diagrams for SBCIN for the west sub-region (left) and east sub-region (right).

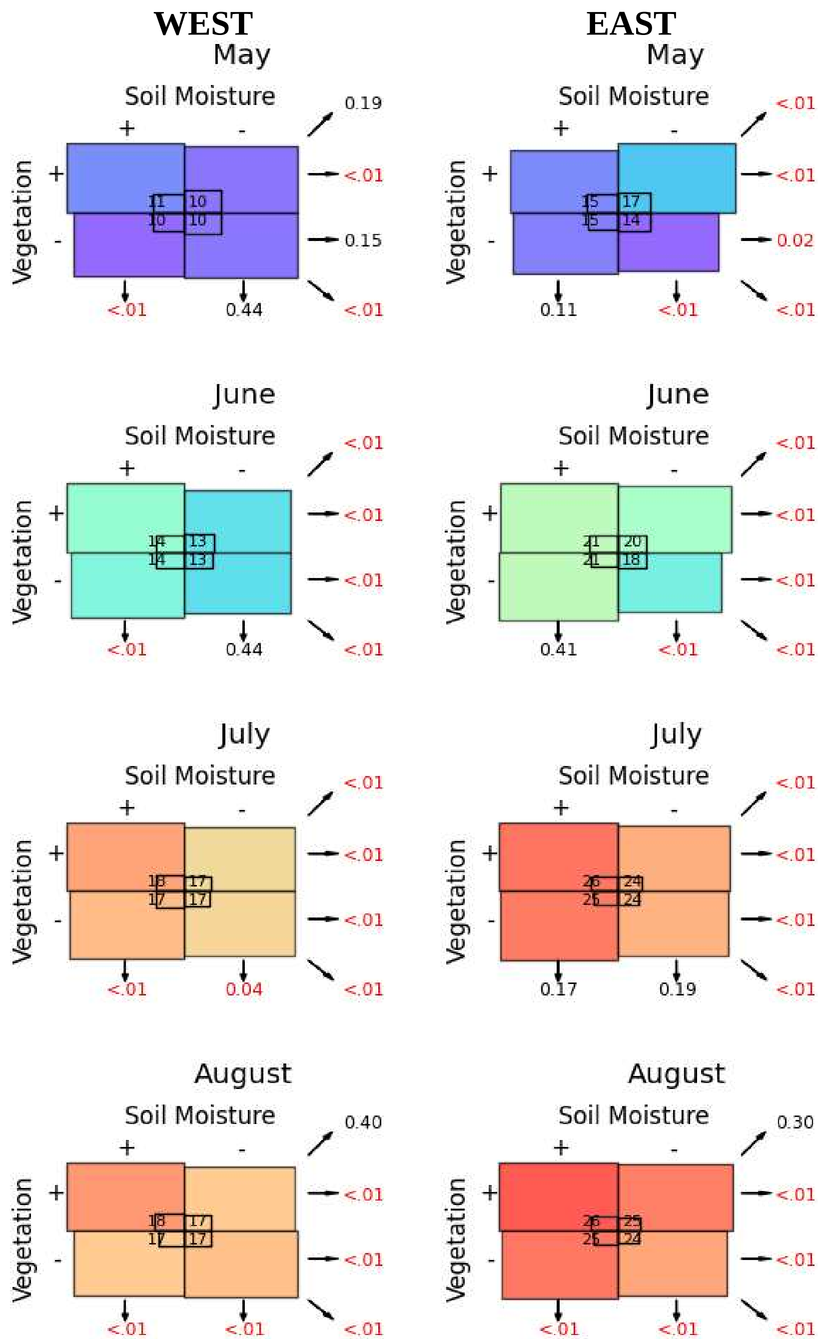

Figure 4.21. Table diagrams for PW for the west sub-region (left) and east sub-region (right).

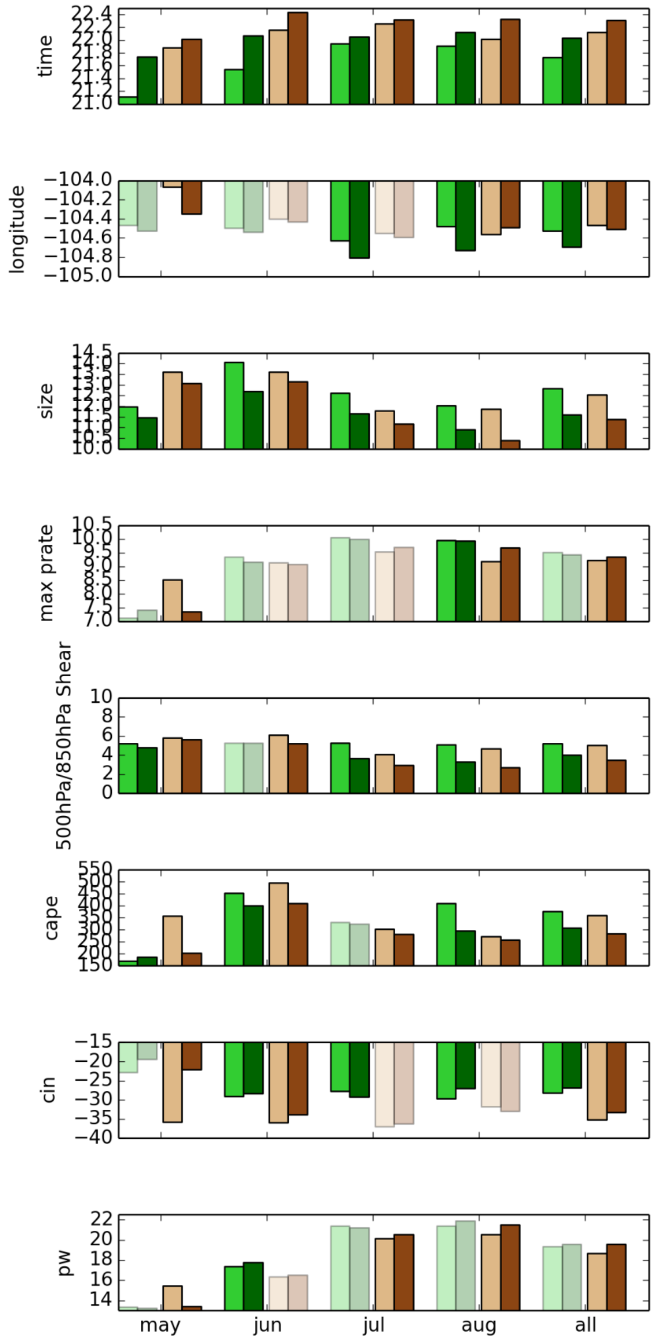

Figure 4.22. CI and environmental variables mean values for CI on MCS days over moist soil in light green, CI over moist soil on non-MCS days (dark green), CI on MCS days over dry soil (tan) and CI on non-MCS days over dry soil (brown).

CHAPTER 5

THE IMPACT OF SOIL MOISTURE AND VEGETATION COVER ON ELEVATED MIXED LAYERS IN THE US GREAT PLAINS

5.1. Introduction

When deep, well-mixed planetary boundary layers (PBLs) form over elevated terrain, they may be advected downstream over lower terrain within certain vertical wind profiles. In the absence of diabatic effects, the thermal and moisture characteristics of the layer are maintained, resulting in an elevated mixed layer (EML) that is relatively dry and having a steep lapse rate. The EML, located above a locally developed PBL that is generally cooler and moister, can act as a "lid" on deep, moist convection if the inversion at the base of the EML is sufficiently strong. The EML can also provide an environment for vigorous convection due to the associated steep lapse rate, if sufficiently warm and/or moist air exists below the EML. The idea of a "lid" on convection in the central United States Great Plains (GP) was first discussed by Means (1952), who described thunderstorm activity under warm air at 700mb, but no physical explanation or origin of the warm air aloft was given. The importance of the EML to severe weather forecasting was discussed by Fawbush and Miller in the same year (1952) as key to the type 1 tornado sounding, characterized by a moist layer in the lowest levels above which lies an abrupt relative humidity break and thermal inversion. They recognized that above the inversion was a layer resembling a well-mixed PBL, which has a nearly dry adiabatic lapse rate and nearly constant mixing ratio, extending to approximately 500 hPa.

This concept, of low-level moist air from the Gulf of Mexico overlain by deep EMLs originating from higher terrain to the southwest, was first described by Carlson and Ludlam

(1968) to characterize severe weather outbreaks in the GP. Carlson et al (1983) provide an excellent summary of research at the time on EMLs, including research on EMLs outside of the central US GP, including India, Spain and Australia. Stensrud (1993) conducted a study of EMLs (referred to as elevated residual layers in this paper) using a simple slab model to examine evolution, as well as data from a one-month field campaign in Arizona, highlighting local EML formation over the elevated terrain north of the Mogollon rim impacting soundings in the Phoenix area within 24 hours of formation. Lanicci (1991) conducted a comprehensive 3-year climatology of EMLs in the central US from 1983-1986 from April through June, characterizing monthly and regional frequency as well as relationship of EML occurrence to severe weather in addition to conducting a modeling study in which air parcel histories were examined for the upper, middle and lower atmosphere to study the origins of the EML and moist low-level jet (LLJ).

In addition to Lanicci (1991), several other early modeling studies were conducted to understand the origin of the central GP EML. Modeling studies were conducted due to the lack of a sufficiently dense observation network over the presumed genesis region of northern Mexico and SW US. Benjamin and Carlson conducted both a three-dimensional study of EML evolution in a modeling case study, including parcel trajectories through space (1986a) as well as an idealized two dimensional study of boundary layer evolution over an isolated 2000 kilometer wide plateau (1986b). In the idealized study, they found the most important factor in EML development to be differential sensible heating brought on by differences in soil moisture (SM) between the EML genesis region and downstream, finding that, while the elevated terrain assisted in creating conditions for an EML with higher potential temperature, that the differential sensible heating created the EML even without the elevated terrain. Lanicci et al (1997) conducted a series of four numerical simulations, varying the SM distribution in the Penn State/NCAR regional model to study PBL evolution, EML, dryline lifecycle and rainfall distribution. While the regional SM distribution variations were most interesting in regards to dryline formation and evolution, the SM distribution over northern Mexico was found to be critical to EML development.

More recently, Banacos and Ekster (2010, BE2010) conducted a comprehensive study of EML relationship to severe weather occurrences over the Northeast CONUS. They found that out of 447 convective event days from 1970 through 2006 associated with significant severe weather, 34 of these days were associated with EMLs. Though a small number of days (7.6%), the significant severe days associated with EMLs accounted for 53% of the fatalities. BE2010 found that the mean 700 hPa flow pattern preceding and on EML days showed a trough on the west coast and ridging over the eastern CONUS, as opposed to non EML significant severe weather event days showing a progressive shortwave trough, with the axis moving from the mountain west 48 hours prior to the event to the Midwest by the day of the event using the NOAA HYSPLIT model using the NCEP/NCAR Reanalysis three-dimensional motion fields. Trajectory analysis revealed that parcels originated from wide ranging locations in and around the CONUS, but finding in the mean parcel trajectory a pattern of subsidence 12 to 48 hours prior to the severe weather event in the Northeast.

Within modeling studies, the importance of choice of physical parameterizations was highlighted by Stensrud et al (1993) in a one-month model climatology experiment of the North American Monsoon (NAM). They highlighted that the choice of physical parameterizations was as important as initial conditions in model performance. Bright and Mullen (2002) specifically looked at the importance of PBL parameterizations in simulating the NAM. They found that significant differences between PBL schemes existed in the depiction of PBL development , and the convective inhibition in particular, which then impacted the depiction of convection in the model runs. More recently, Erlingis and Barros (2014) conducted a modeling study to examine the importance of land use and SM in relation to the PBL parameterization in forecasting a day-to-night transitioning mesoscale convective system (MCS). They found that, while land use impacted thermodynamic variables, and to a lesser extent shear, the choice of PBL parameterization had a greater impact on the depiction of the pre-storm PBL and subsequent MCS.

Except for BE2010, little recent research has been conducted on the subject of EMLs with regard to origin, sensitivity to SM and other land surface properties and relationship to severe weather activity downstream over lower elevations. Since the seminal work on the subject by Carlson, Lanicci and others, several new satellite observational datasets have been developed that allow an inspection of the sensitivity of EML genesis over elevated terrain to surface properties and the subsequent importance of these EMLs to weather downstream. Additionally, higher resolution reanalysis datasets such as the North American Regional Reanalysis (NARR: Mesinger et al. 2006). have been developed, providing a consistent three dimensional depiction of the atmosphere through time to allow a backward depiction of the flow field prior to EMLs arriving at GP sites back to the point of origin.

The remainder of the paper is organized as follows. Section 2 provides an overview of the observational data and methods utilized in this research. Section 3 provides the results of the observational research, which is broken into three major areas. Section 3a presents the results of the EML climatology for eight US GP radiosonde launch sites, including prevalence of EMLs throughout the warm season and the relationship to severe weather local to the site. Section 3b details the results of the relationship between PBL mixed layer and EMLs at sites to the west over elevated terrain to satellite observed SM and vegetation. Section 3c shows the results of back trajectories from EMLs detected in section 3a, including the relationship between parcel origin and severe weather downstream as well as surface characteristics at the origin. Section 4 provides an overview of the modeling study methods and results of a case study from one of the EML event days from section 3c, including the sensitivity to altering SM over the site of EML origin and to PBL parameterization. Section 5 presents a discussion of the results and conclusion.

5.2. Observational Study Data and Methods

First, a climatology of EMLs from US GP radiosonde launch was developed using data from the National Climatic Data Center's Integrated Global Radiosonde Archive (Durre, 2006). Only 1200 UTC soundings were utilized in the assumption that these were the closest, consistent soundings prior to severe weather events later in the day, whereas 0000 UTC soundings stand a greater chance of being contaminated by afternoon convective activity. Observed radiosonde data was utilized rather than reanalysis data due to the greater vertical resolution necessary to accurately capture characteristics of the EMLs. The period of 2003 through 2015, April through September, was examined (2196 days total). The detection of EMLs was conducted in a similar manner to previous studies, including Lanicci (1991). Initially, a system utilizing both temperature and dewpoint profiles was utilized to detect EMLs using characteristics of near adiabatic lapse rate and constant mixing ratio described in previous literature. As in Lanicci (1991) a system utilizing only the temperature profile was utilized due to the dewpoint criteria excluding too many cases from the study.

Second, a study of EML source region mixed layer sensitivity to surface properties of SM and vegetation was conducted. As in the previous section, radiosonde data was utilized and the same method for detecting EMLs was utilized here to detect mixed layers. A map of the EML sites and the EML source sites is shown in Fig. 5.1. Only the 0000 UTC soundings were utilized as these are closest to the time of maximum PBL depth.

The SM data from the North American Land Data Assimilation System 2 (NLDAS), utilizing the Noah land surface model (LSM) are used (Xia et al 2012). The NLDAS is an offline LSM run with observations of surface weather and hydrologic phenomenon. The horizontal resolution of the NLDAS is one-eighth degree or roughly 14 km. Only the upper most layer available (0-10 cm) was used. The NLDAS snow mask was also used to eliminate mask points with greater than 25% snow cover at the grid point.

The Enhanced Vegetation Index (EVI) data used was from the Moderate Resolution Imaging Spectroradiometer (MODIS). This dataset is updated every 16 days. The level 3 dataset was utilized, which has 1-km resolution and utilizes data from both the Aqua and Terra Satellites. The EVI developed and implemented in MODIS land (Strahler et al 1999) is similar to the well-known Normalized Difference Vegetation Index, with constant multipliers on factors and a blue band correction in the denominator.

Third, based on the EMLs found in the first part of the study in the US GP, a study of the land surface sensitivity of EMLs at the point of origin was examined. To do this, back trajectories were accomplished using three-dimensional motion vectors in a manner similar to HYSPLIT Lagrangian parcel trajectory model (Draxler and Hess 1997). The NARR was used for motion vectors. The Runge-Kutta third order time integration was used to complete the back trajectories utilizing NARR three-dimensional motion vectors.

For each EML event, 18 back trajectories were made from 1800 UTC the day of the detected EML event to 1800 hours prior to 0000 UTC and from 1200 UTC back 36 hours to 0000 UTC. The 18 points consist of 9 points from levels +/-20 hPa above and below the vertical midpoint of the EML. The nine points are +/- 100km in the cardinal directions and at the vertices of a 200 by 200km box with the radiosonde point in the middle. An example of the spatial array of parcel starting points and back trajectories are shown in Fig. 5.2 for 27 April 2003 from the KOUN radiosonde site and in Fig. 5.4 for a 36-hr back trajectory from KDDC on 28 May 2003. The origin points are represented with black stars, with the sounding site in the middle, and the back trajectory points in black triangles.

From this "cloud" of back trajectory points, the central point is chosen using Affinity Propagation clustering (Frey and Dueck 2007) as implemented in the Python programming language library Scikit-learn (Pedregosa et al 2011). AP clustering considers all points as potential exemplars (cluster centers) with each data point viewed as node in a network that then communicates recursively across the network to minimize an energy function to arrive at exemplars. In this case, the energy function used was the Euclidean distance. If the mean distance from the cluster center point and all other points was greater than 400 km, the case was not used under the assumption that the origin of the parcel was unreliable due to the large spread in the back trajectories. At this cluster center point, the surface properties were determined from the previously described SM and vegetation datasets for comparison across space and time. The surface properties were sampled in a 100 by 100km box surrounding the back trajectory point.

As seen in the back trajectory example in Fig. 5.2, even on a day with relatively uniform flow near the trajectory level, the spread is quite wide, across thousands of square kilometers, but it is reasonable to assume that the parcel at KOUN at 1200 UTC on 27 Apr 2003 originated in central New Mexico over high terrain. Fig. 5.3 shows the Skew-t diagram with the EML from the KOUN sounding in (a) and the KABQ sounding, near the back-trajectories in (b), showing the origin deep PBL mixed layer along the same adiabat as the downstream EML. This is opposed to Fig. 5.4, showing a 36-hr back trajectory originated from KDDC on 28 May 2003. In this case, the mean flow over time is weaker than that in Fig. 5.2 given that the point of origin is closer. Despite this, there is large spread in the horizontal distance, from SE Montana to central CO and east into Nebraska, but also in the parcel origin height, from 820 hPa in the northernmost origin in MT point to 700 hPa in western SD. The spread between points grows with time and is the primary factor for limiting the back trajectories to only 36 hours. In addition to limiting the back trajectories to 18 and 36 hours, points are also eliminated by elevation of origin, to include only parcels originating above terrain above certain elevation levels. Tested elevation levels and reasoning is explained in the following section.

Significance testing is accomplished using the Mann-Whitney (MW) U test. Unless otherwise stated, statistical significance is assumed at the 95% level. The MW test assumes that measurements are independent of one another. It is not uncommon in this dataset to have an EML event occur at multiple sounding locations on a single day. To attempt to ensure independence of measurements, if the 100 by 100 km SM/EVI sample area of two back trajectory locations overlap, all but one overlapping member is thrown out.

5.3. Observational Study Results

5.3.a. EML climatology

A total of 1533 EML events (depth greater than 75hPa) were found in radiosonde data from the eight US GP sites. An event is defined as an EML of sufficient depth at an individual station. The number drops to 595 for a depth greater than 125hPa and further to 147 for depth greater than 200hPa. Of the 1533 total, 660 were associated with severe weather (at least one severe weather report within 200km of the radiosonde site on the day of the EML). Fig. 5.5 shows a graph and table of the EML counts by depth of EML and whether severe weather occurred near the site. It is clear that the stations with large numbers of EML events are the stations closest to the elevated terrain of the Rocky Mountains to the west with Rapid City (KRAP), North Platte (KLBF) and Dodge City (KDDC) having the greatest number of EMLs at all depths with KRAP leading all stations in all EML depths. Although the western radiosonde sites lead in total counts of severe EML events, by percentage of EML and severe count at the station, the two stations furthest to the north and east have the highest number, Omaha (KOAX) and Topeka (KTOP), with KOAX having the greatest proportion of severe EML events to total at 0.52. The two stations with the lowest proportion of severe EML events to total were the two northernmost stations, Rapid City and Aberdeen (KABR).

Looking at the data by month (Fig. 5.6), there is a poleward transition through the warm season, with EMLs occurring more frequently at the southern stations in April and May, and more frequently at the northern stations in July through September. The two southern stations (Norman, KOUN and Dallas, KFWD) have 54% and 64% of warm season EML events respectively in April and May, while the mean for the for northernmost stations is roughly half this total with 30% in the first two months while 16% of EML days are found in July-September in KOUN/KFWD and 36% occur in the northern 4 stations. Comparable numbers of EML days occur across all stations, with an average of 16%, varying between 13-18% across all stations. Similar figures are shown by considering EMLs detected on days with severe weather in the vicinity as a percentage of all EMLs in Fig. 5.7, but are more exaggerated regionally. In this case Apr/May have 68% of all severe EML events in the southern two stations while only 22% in the northern 4 stations, as opposed to July-September having only 12% of events versus 54% of events in the northern stations, with June once again having the lowest variance of all months across stations.

5.3.b. EML Source Region Climatology and Relationship to Surface Properties

The record of mixed layer (MLs) from the 10 EML source region radiosonde sites from 0000 UTC soundings, close to the time of expected maximum PBL depth, from 2003 to 2015 shows that, compared to EMLs at downstream sites, there is much less spatial and temporal variability (by month). Fig. 5.8 shows the total by month MLs with tops less than 650hPa. Aside from the lower elevation Texas site, KMAF, included to try to catch southwesterly flow entering the CONUS from the hypothesized key EML genesis region (e.g., Carlson and Ludlum 1968, Lanicci 1991) in lieu of consistent radiosonde data from northern Mexico in this time period, the distribution of deep ML events is consistent across months, with roughly 10 per month per station.

First, Fig. 5.9 shows the mean and standard deviation of SM and EVI for April through September, broken into three regions: North (KDEN, KRIW, KSLC, and KGJT), South (KFGZ, KTUZ, KEQZ and KABQ) and Texas (KAMA, KMAF). All northern sites see a large drop in SM from April until early July when mean values become steady with time. Southern sites see a less dramatic drop in SM mean, then dramatically increase with the arrival to the Southwest Summer Monsoon. Texas mean and standard deviation values hold fairly steady throughout. Interestingly, from roughly the beginning of July onward, the mean and standard deviation values are similar for all regions. The regional pattern of EVI is very different from SM. North shows a large increase from the beginning to a peak in June, while South steadily increases to a peak in August with Texas the most similar to the SM pattern, is relatively steady throughout. The standard deviations show Texas with high variability throughout, North showing a higher variability than South until a switch at the beginning of August.

Correlations between NLDAS SM and MODIS EVI were conducted in the following manner. The NLDAS SM data at the time of the radiosonde launch, 0000 UTC in this case, was correlated to NLDAS SM at the same time. When comparing MODIS EVI data to radiosonde data, the last available EVI data was used, with the vegetation assumed to change slowly between 16-day measurement intervals. Values for both SM and EVI were averaged within a 100x100km box with the radiosonde site at the center. All sites and month have significant, negative correlations as expected (Fig. 5.10; low SM leads to more sensible heat flux from the surface, leading to hotter, deeper PBLs). By region, the southern sites show consistently higher correlations in the last three months, corresponding to the period of higher mean SM and greater variance in Fig. 5.9a. In the north, outside of KGJT, which has the highest two correlations in May and Aug, the other three northern stations have their two highest correlation values in the first four months of the time period, consistent with the period of higher mean in early summer. Texas stations have relatively high correlations through the time period.

The same relationship is seen in Fig. 5.10b, showing significant correlations between EVI and ML depth. There are far fewer significant correlations and the correlations are much lower for EVI to ML depth compared to SM. Once again, with less vegetation, drier conditions would be expected, leading to a greater Bowen ratio, more sensible heating and deeper boundary layers in the afternoon. The strength and significance of correlations of SM to EML depth show a spatial-temporal pattern, with strongest correlations in the north stations (KRIW, KDEN and

KSLC) in early summer, more sparsely vegetated southwest station (KTUS, KEQZ and KABQ) showing significant correlations mostly in late summer and high plain station to the east (KAMA, and KMAF) showing the strong correlations throughout the summer. This is in line with the mean and standard deviation of EVI in Fig. 5.9b, with the strongest correlations during the period of peak vegetation, with Texas showing steady vegetation throughout.

5.3.c. Relationship of EML to Surface Properties at Back Trajectory Sites

Using the back trajectory model described in section 2a, Fig. 5.11 shows the 18- and 36-hr mean trajectory end points from the eight GP sounding sites (black) with red representing days with severe weather within 200km of the radiosonde site and blue with no severe on the day the EML was detected. In all cases, the mean 18-hr severe back trajectory point is a greater distance from the radiosonde site and further south, implying that the winds at the midpoint of the EML are greater leading up to severe weather days and tended to originate further southwest. The same holds true in nearly all 36-hr back trajectories as well. Comparing the 36-hr to 18-hr trajectories, the 36-hr trajectories have a mean end point further south.

First, correlations are made with all 1533 18-hr and 872 36-hr cases in which there are valid SM values at the back trajectory point and the EML depth at the radiosonde site is greater than or equal to 75hPa. The correlation between EML depth and SM was -0.073, meaning a low SM at 0000 UTC the prior day at the back trajectory point is correlated to a deeper EML downstream the next day 18 hours later. A slightly greater magnitude correlation was found between the EML top pressure and SM at 0.10, with the pressure of the EML base also positively correlated at 0.058. The correlations between severe event count and SM yielded no meaningful correlation (.002). As for correlations by month, while all months have a negative correlation between SM and EML depth, only August EML depth has a significant correlation at -0.14. The 36-hr back trajectories had no overall significant correlations, while the month with the strongest correlation between SM and EML depth was June at -0.18.

Further examination of all back trajectories reveal that the mean elevation for nearly a third of the 18-hr (509) cases and 47% (409) of cases for 36-hr back trajectories were at 1600m or less, meaning the underlying surface was not at an elevation over which deep PBLs mixing to low pressures above would be expected. Examining, by radiosonde site, only those EMLs that track back to points with elevations greater than 1600m reveals distinct regional patterns for both 18- (Fig. 5.12a) and 36-hr (Fig. 5.12b) back trajectories. First, for 18-hr back trajectories, the southern three sites show almost no significant correlation between EML depth, base or top with back trajectory point SM with KFWD and KOUN having correlations of the opposite sign that we would expect. This is opposed to the result in the north where from KTOP north, positive correlations are found between SM and EML top and bottom as well as negative between SM and EML depth. When these 5 northern stations are pooled together (Fig. 5.14a) the result is significant correlations between all EML characteristics with SM, strongest at all EMLs 100hPa or greater depth to 150 hPa or greater depth, though a degraded relationship with greater depth.

The pattern is different for 36-hr back-trajectories in Fig. 5.13b, with the southern three stations showing similar, but not significant positive correlations between EML top and bottom with SM, with similar correlations in the northern two (KRAP and KABR), with the middle three stations show no relationship between EML characteristics and SM at the back trajectory point. Pooling the three southern stations (Fig. 5.14b) shows positive correlations results in significant correlations between all EML top and bottom with SM, with a stronger relationship with greater EML depth to 150 hPa depth.

For EVI, examining only back trajectories with origins above 1600m as in the SM analysis yielded no significant results for 18- or 36-hrs. Conducting the analysis to include all points with elevations greater than 1200m reveals some significance in the 18-hr back trajectories and regional differences. The pattern (not shown) is different from the SM correlations, with the southern four stations having the overall strongest correlation between EML depth the EVI. Examining the correlation with by EML depths in Fig. 5.15 including only these southern stations reveals only significant correlations between depth for EMLs of 100 hPa depth or less, with no significant correlations in the 36-hr back trajectories. Comparing these results to the origin radiosonde correlations in Fig. 5.10b, it is clear that the west Texas stations possessed the strongest negative correlation to ML depth, with the southern four stations having mean trajectories in this region for 18-hr trajectories, as seen in Fig. 5.11, justifying the lowering of the minimum elevation threshold to 1200m, closer to the mean elevation in the region.

5.4. Modeling Study

5.4.a. Modeling Study Data and Methods

A modeling case study was conducted to explore aspects of EML genesis, downstream EML advection and role of the EML in downstream convection in a quasi-idealized environment. All model simulations were accomplished with the Advanced Research Weather Research and Forecasting Model (WRF; Skamarock et al. 2008) version 3.4.1. A two-domain nested structure was used with the outer and inner domain horizontal grid spacing set to 12 and 3 kms (domains shown in red boxes in Fig. 5.1) with 50 vertical levels on a stretched grid. The interface between the outer and inner nest was one-way (i.e., no feedback from the inner to outer nest). Parameterizations common to all simulations are the Noah Land Surface Model (Ek et al.

2003), Goddard radiation (Chou and Suarez 1999), Thompson microphysics (Thompson et al, 2008) and Kain-Fritsch cumulus (Kain et al 2004) in only the outer domain. For the planetary boundary layer and turbulence, one set of simulations was accomplished with the Yonsei University (YSU) scheme (Hong et al. 2006) and one set of simulations with the Mellor-Yamada-Nakanishi-Niino (MYNN) 2.5 order closure (Nakanishi and Niino, 2006) scheme in order to test the sensitivity of PBL growth over the EML source region and the subsequent downstream advection into the GP.

Five 42-hour simulations were conducted focusing on the central Rocky Mountains to the central GP from 1200 UTC 7 May 2004 at through 0600 UTC 9 May 2004. The observed KOAX skew-t diagram from the time of EML detection is shown in Fig. 5.16. A deep layer with a nearly adiabatic lapse rate exists from 750 hPa to nearly 500 hPa. The back trajectories, shown in Fig. 5.17, show that, while there was decent spread from the points originating in the vicinity of KOAX, all points originated over high terrain, with the points originated the furthest east in NE Colorado originating at over the lowest elevation, but still above 1500 m. This case was chosen because of the great number of EML events detected in the northern radiosonde station data and because this case did follow the correlation found in section 3, i.e., low SM at the point of trajectory origin in the Rocky Mountains with deep EML downstream at the KOAX radiosonde site. Fig. 5.18 shows NEXRAD composite reflectivity of the event at 2100 UTC to 0300 UTC on 8-9 May and the accumulated Stage IV precipitation from 1200 UTC to 0600 UTC 8-9 May. At 2100 UTC (Fig. 5.18a), convection initiation is beginning across NE and into IA with the first weak radar returns in a line form just north of the KS/NE border, northeastward into central IA. By 0000 UTC (Fig. 5.18b) there are numerous mature supercells south and east of the convection initiation features at 2100. By 0300 UTC (Fig. 5.18c) the supercells have morphed into two distinct MCSs, one in central southern NE and one in southern IA. The total precipitation from Stage IV precipitation rate data (Fig. 5.18d) shows the greatest totals in south central NE from training supercells then a stationary MCS line as the system organized.

The model run was started at 1200 UTC on 7 May to allow the PBL to fully develop over the EML source region to the west to then advect downstream the next day. First a control simulation (CNTL) was conducted with no alterations made to SM to assess model performance with regards to observed conditions. The upper layer SM distribution is shown in Fig. 5.19a. Four quasi-idealized simulations were then conducted: 2 with the YSU PBL scheme and 2 with the MYNN PBL scheme. For each PBL scheme, the SM at high elevations was modified to include either a high or low SM anomaly (DRY_YSU, MOIST_YSU, DRY and MOIST). For these four runs, the SM in the eastern portion of the domain was set to 19% SM by volume, the average over this area at the start of the model simulations. For the outer domain, the SM was set to a uniform 19%. An example of the dry anomaly initial SM is shown in Fig.5.19b, with the minimum value at 4% SM by volume. The moist anomaly would appear the same spatially but with a maximum value of 34% by volume. Additionally, the land use was set to grassland and soil type to clay loam throughout in the idealized cases.

5.4.b. Modeling Study Results

Fig. 5.20 shows the simulated precipitation totals for all model runs from 1200 UTC to 0600 UTC 8-9 May. All simulations produce precipitation over far too wide an area compared to the observed precipitation in Fig. 5.18d. While all simulations produce convection in western NE southward into eastern CO and western KS, the poorest performers compared to observations were the MOIST (b), MOIST_YSU (d) and CNTL (e) runs. While the DRY (a) and DRY_YSU

(c) runs located the precipitation maxima in south central NE further north than the MOIST runs, the areal agreement of the total precipitation field in NE and IA, as well as the convection that moved off the Black Hills, compared better to observations. On the other hand, the CNTL and MOIST runs performed better in regards to the placement of the precipitation maxima in south central NE.

To examine the evolution of MLs, to include both deep PBLs over the mountain west, then subsequent EMLs transitioning east, Fig. 5.21 shows Hovmöller diagrams of mean ML depth between geopotential height levels 1500m and 7000m by longitude in the along the length of the domain east to west and in the center north to south (-112 to -98W and 38 to 44N). Through time, from top to bottom, from -105 W longitude, the diurnal cycle of deep PBL growth during the day to stable PBLs at night is seen in all plots, with the strongest 2-day amplitude in the DRY_YSU (Fig. 5.21a) case and the weakest, with visible growth of the PBL above 1500m on the second day in the MOIST (d) experiment. The clearest difference between the dry and moist experiments is the ML growth near -105 W longitude then slow EML movement eastward between 0600 UTC through 1800 UTC to about -100W. There is a secondary ML movement eastward, nearly identical in all experiments, also originating at about -105W, faster than the primary EML moving eastward in the DRY experiments, making it to -100 W between 0600 and 1200 UTC before weakening. Also of note is the magnitude of the PBL depth increase is greater than on the first day for all models, with the greatest increase close to the eastern edge of the Rocky Mountains. This is primarily due to the EML from the western edge of the domain moving eastward and facilitating a deeper PBL on day two.

More insight in the difference between the DRY and MOIST runs, as well as the behavior of PBLs and EMLs with differing PBL parameterization schemes, difference plots of the

Hovmöllers in Fig. 5.21 are made in Fig. 5.22. First, in the difference plots between DRY and MOIST and DRY_YSU minus MOIST_YSU (Fig. 5.22c and Fig. 5.22b), the primary EML movement is visible in both differences, moving to the top and right of the plot in a positive difference, though wider and of greater length in the MYNN difference plot, making it to the edge of the plot eastward and timewise to the end of the experiment. In both differences the difference in PBL growth is greater than on the first day, lending more weight to the argument that the atmosphere is conditioned on the first day with an EML that facilitates growth on the second day rather than a decrease in SM leading to more sensible heat flux on the second day (there is more SM loss in the MOIST experiments). In the DRY_YSU minus MOIST_YSU plot (Fig. 5.22b) between 1200 UTC and about 1700 UTC there is no difference from -106W westward, meaning there is no difference in mean MLs at this time, while in the MYNN difference (Fig. 5.22c), a weak positive difference is maintained, especially between -108W and -105W. This is evident in the DRY_YSU minus DRY experiment with a negative (DRY with greater ML) value between 0600 to 1500 UTC on 8 May, providing evidence that MYNN is maintaining the EML over the rough terrain of the Rocky Mountains better than the YSU experiments. Also notable in Fig. 5.22a is the large negative area where the EML was noted in Fig. 5.21a and c. Again, the MYNN is maintaining the EML at greater depth than in the YSU experiment and moving it out on the GP while the YSU is maintaining at EML of greater depth from 0600 to 1800 UTC adjacent to the Rocky Mountains from -105W to -102W. In the MOIST_YSU minus MOIST (Fig. 5.22d), the magnitudes are greatly diminished from the DRY difference, which is to be expected with PBL heights much lower over the Rocky Mountains. Of note is that, unlike the dry difference, which is a mixture of positive and negative depending on where mixed layers were favorably transported in each experiment, the MOIST experiment is nearly all positive, or that the YSU scheme is producing deeper PBLs and these PBLs are being maintained as EMLs by the YSU scheme.

Examining Skew-T diagrams from 41.3N, -101W (black dot in western NE in 5.Fig. 19b) at 1000, 1400 and 1800 UTC on 8 May for DRY and MOIST in Fig. 5.23 reveals changes from a base state at 0600 UTC when the diagrams were nearly identical (not shown). At 1000 UTC (Fig. 5.23a), the lapse rate for DRY shows warmer temps from 720 hPa to 500 hPa, but no steeper lapse rate than MOIST, while mid-level moisture values are also comparable. At this time, the PW is higher in the DRY experiment due to higher low level moisture. By 1400 UTC (Fig. 5.23b), the signature of the EML is stronger in the DRY experiment, with a distinct inversion at 750 hPa and greater difference between the two temperature plots appearing at this level. Also evident is mid-level drying, causing the PW to be nearly equal between the two experiments. At 1800 UTC (Fig. 5.23c), the inversion below the EML is still evident with the PBL trying to grow underneath in the DRY experiment, while in the MOIST the PBL appears to be much deeper to the 700 hPa level. The PW in the MOIST experiment has surpassed the DRY at 20 and 19 mm as the EML continues to dry the mid-levels in the DRY experiment. At this time, with the EML driven inversion in the DRY experiment, the convective inhibition (CIN) remains high at 73 J/kg, but is almost non-existent in the MOIST experiment at 1.4 J/kg.

Comparing the same times, but this time examining the difference in skew-t plots for DRY and DRY_YSU in Fig. 5.24, we see almost no difference at 1000 UTC (Fig. 5.24a), with a slight edge in PW and CAPE in the YSU due to greater moisture near the surface. By 1400 UTC (Fig. 5.24b), the difference in the EMLs is evident with a stronger inversion in the MYNN run at about 770 hPa with the inversion higher at about 720 hPa in the DRY_YSU. There is also more drying in the MYNN run in the midlevels. These factors lead to more favorable thunderstorm indices in the YSU, with PW at 20.49 mm and CAPE at 1027 J/kg compared to 17.27 mm and 995 J/kg in the MYNN. By 1800 UTC (Fig. 5.24c), the difference in the EML has disappeared with the YSU aggressively building a deeper PBL in the previous three hours and maintaining a slight advantage here over the MYNN.

The differences in stability brought about by the differences in PBL formation over the mountain west and subsequent EML transport over the western GPs the following day with differing SM and PBL parameterizations causes differences in timing and spatial variation in precipitation. CI occurred earlier in the MOIST experiments and too far west and south. The results of this are shown in the total precipitation field in Fig. 5.20, the MOIST and CNTL experiments produced far more precipitation in western NE and in CO and KS, where the observations did not show precipitation. Fig. 5.25 shows the number of individual convective cells in the bar graph, and the mean size of these cells in the line plot from 1800 UTC to 0600 UTC on 8 to 9 May 2004. Individual convective cells were determined using image processing software of the Scipy library of the Python programming language. The software identified cells by finding contiguous grid points of at least 5 m/s vertical velocity at 500 hPa. The MOIST experiment has the earliest CI at 1900 UTC and maintains the most convective cells until 0000 UTC on 9 May. This is due to the much lower CIN as shown in Fig. 5.23c. Despite the low CIN, the CAPE in the MOIST run is the lowest compared to all other runs, leading to MOIST having the smallest convective cells from 2100 to 0000 UTC. During the period of initial cell growth, from 2100 to 2300 UTC, the MOIST experiments maintain cell count superiority over like-parameterized DRY experiments, while the inverse is true of mean convective cell size. This relationship is enabled by low CAPE/low CIN in the moist experiments and high CAPE/high CIN in the DRY experiments, leading to fewer, but more intense cells. At 0000

UTC DRY surpasses MOIST in cell count, while it takes until an hour later in the YSU experiments for this to occur due to the later overall start in convection in the YSU experiments. After 0200, the individual cells in NE and IA merge into an MCS, complicating results, but generally, the YSU experiments maintain larger and more convective cells until the end of the model run.

5.5. Discussion

The observational portion of the study utilized radiosonde data, in both the EML source region of the western CONUS, and downstream sites over the GPs, as well as offline land surface model derived NLDAS SM and MODIS satellite observed EVI values. First, MLs were detected over the EML source region from radiosonde data and compared to SM and EVI, finding a consistent negative correlation between regional ML depth from the 0000 UTC radiosonde data. This relationship matches our understanding of first-order SM and vegetation impact on the partitioning of sensible and latent heat fluxes, i.e., a barren, dry environment would have nearly all incoming shortwave insolation partitioned to sensible heat flux while a moist, vegetated area would have much more of incoming radiation partitioned into latent heat flux. All things being equal, the dry barren environment would have deeper mixed layers, with more shallow in the vegetated, moist environment. Many other factors influence the depth of the PBL, including low level water vapor concentration, temperature and humidity above the boundary layer and cloud cover that cannot be accounted for here. There were definite spatial and temporal relationships between the SM and EVI correlations. Partitioning the ten origin radiosonde sites into three regions to examine mean and variance revealed that the highest correlations between SM and EVI with ML depth occurred when the mean and variance were maximized i.e., the best overall correlation in the North stations in late Spring early Summer while the mean is not maximized, but still relatively high, and the variance is greatest.

While most studies of the EML focus on the southern Great Plains and the relationship to severe weather in this region, of the EMLs found in 1200 UTC radiosondes from GP sites this study found the greatest number at the western GP sites (KRAP, KLBF and KDDC) while the greatest percentage of EMLs associated with severe weather were found at the central, eastern sites of KOAX and KTOP. Taking back trajectories of the GP EMLs from 18- and 36-hr with the NARR motion fields, the back trajectories for days with severe near the GP radiosonde site tended to have longer back trajectories from a more southwesterly direction, with the greatest difference between mean severe and non-severe day back trajectories at the KOUN and KFWD sites. This matches our understanding of GP severe weather being associated with greater mid-level flow speed, baroclinicity and a more southwest flow indicative of an approaching trough on severe weather associated EML days. The southern GP sites also have many back trajectories ending up in the vicinity of the site, a stagnant airmass featuring an EML born outside the local area but not within the last 36 hours, a scenario not favoring severe weather and an EML that is not reasonably traceable given the spatial and temporal limitations of the reanalysis data.

At the back trajectory points, the SM and EVI was determined and compared to the characteristics of the downstream EML, as well as the prevalence of severe weather in the vicinity of the downstream radiosonde site. When the correlations for all sites and months was accomplished, little relationship was found. When points were only included based on originating location elevation, and the results of the elevated terrain ML correlations were taken into account, statistically significant relationships were found between EMLs and origin point SM and EVI. The five northern most stations had statistically significant correlations between

SM in the back trajectory region when considering only back trajectories to points greater than 1600m and downstream EML depth and top. On the contrary, the correlation between EVI and EML characteristics was significant when considering only the southern-most four stations. This difference was reflected in the correlation analysis of elevated radiosonde site 0000 UTC ML depth to SM and EVI. One possible explanation of the lack of correlation at the southern sites between SM and EML/ML depth is the fact that only NLDAS 0-10cm depth moisture was used. High evapotranspiration rates over the relatively barren surface under the low humidity in Texas and eastern New Mexico, compared to greater vegetation cover further north and lower evapotranspiration rates could mask the deep column SM more so in the south. The relationship between EVI and EML characteristics at the southern radiosonde sites will need to be further explored, possibly being owed to region wide, northern Mexico and Texas, relationships to regional precipitation and EML characteristics associated with large scale climate variability.

The modeling case study utilized a case where EML depth at KOAX was inversely related to SM at the EML back trajectory source in the central Rocky Mountains. The control run showed some timing and magnitude error in relation to observed precipitation rate and radar depiction from Stage IV and NEXRAD composites, though some error is owed to the length of the simulation. The CI was too early, too far west and over too large an area in the CNTL, but the simulations with dry SM over elevated terrain, especially the simulation using the YSU PBL scheme, had a much better depiction of storm CI, with an east-west line of intense convection through central NE. Comparing the simulated soundings on the morning of 8 May shows that the soundings in the dry simulations a closer to reality than the control or wet soundings in the depiction of the EML, which provides both a “lid” on convection and a steep mid-level lapse rate to promote more vigorous convection once initiated.

Analysis of the evolution of EML characteristics between model configurations shows the greatest difference between varying SM over the elevated western portion of the domain. Boundary layers are much deeper and drier in the dry runs over elevated terrain, in the intermediate and downstream there is evidence of an EML in the dry runs, with none in the moist runs, leading to capped, later CI in the dry runs. The difference in EML characteristics is still large between PBL schemes, with the YSU building a deeper PBL over elevated terrain. This does not lead to a deeper EML downstream, as the MYNN scheme maintains an EML further east into the plains, evident in ML difference field in Fig. 5.22c. While these parameterizations are referred to in the literature as PBL schemes (as in this study), they are more accurately turbulence schemes as they treat the parameterization of turbulence throughout the atmosphere, though with less differences in the free atmosphere than in the PBL. Further study should be undertaken to understand the influence of the handling of free atmosphere turbulence in PBL schemes to understand the impact on elevated conditionally unstable layers, especially on turbulent transfer at the top and bottom of the EML.

Further work should be conducted with current and developing SM datasets to understand the impact of surface properties on EML genesis. One interesting result from the modeling study was the early, vigorous convection initiated over the elevated terrain of the Black Hills in South Dakota on the morning of 8 May in the DRY experiments (evident in Fig. 5.20a as a line of precipitation totals extending from the Black Hills, SD to the central NE/SD border). A future study could examine the role and sensitivity of EML characteristics to upstream surface properties in early day initiated severe convection over isolated, elevated terrain. Along a similar line, study should be undertaken to understand the role of EMLs in invigorating nocturnal GP convection, either in assisting nocturnal convection initiation or in invigorating rearward development of convection in an existing MCS, i.e., the arrow in the "bow and arrow" of Keene and Schumacher (2013) in a similar manner to the convection initiation over the Black Hills from the modeling portion of this study.

5.6. Figures

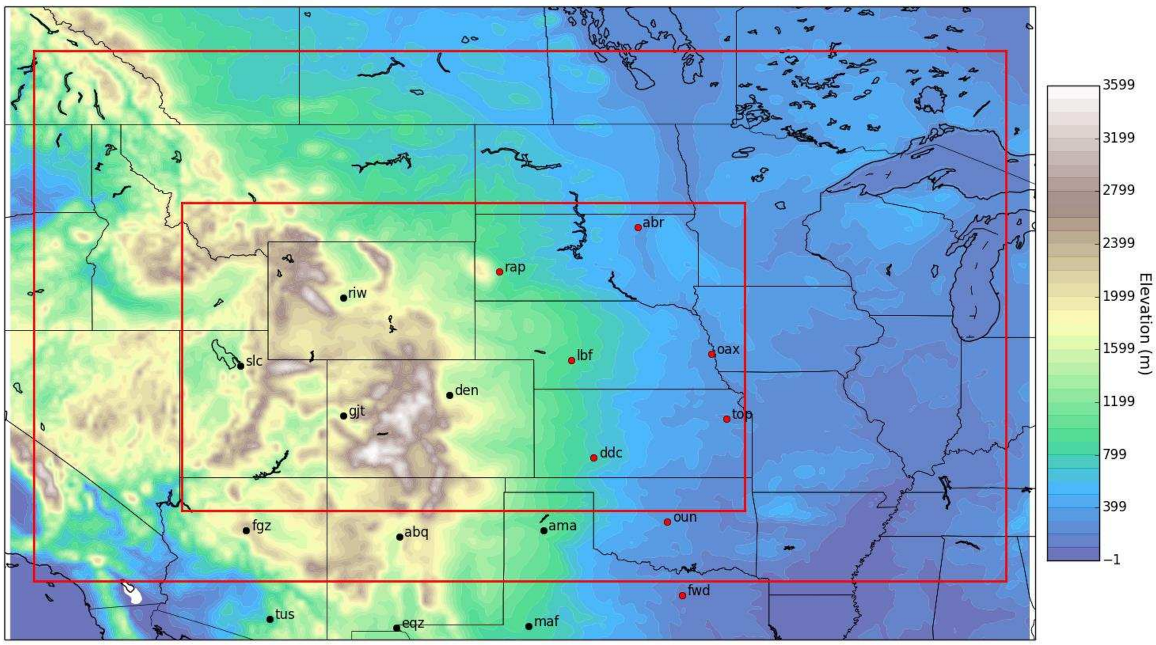

Figure 5.1. Elevated Mixed Layer (EML) source radiosonde sites (black dot) and downstream Great Plains EML sites (red dot). Outer and inner domain of the modeling experiment are outlined in red boxes with elevation in the background in meters.

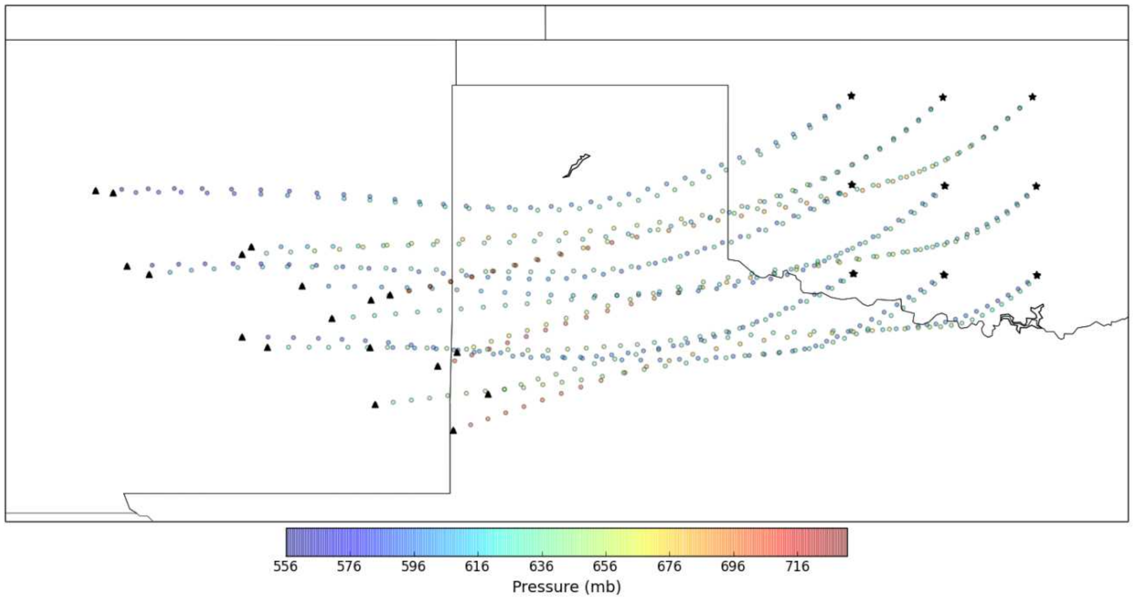

Figure 5.2. Example of back trajectory plot for points surrounding and at the KOUN radiosonde site on 27April 2003. Back trajectory points are colored by the parcel pressure.

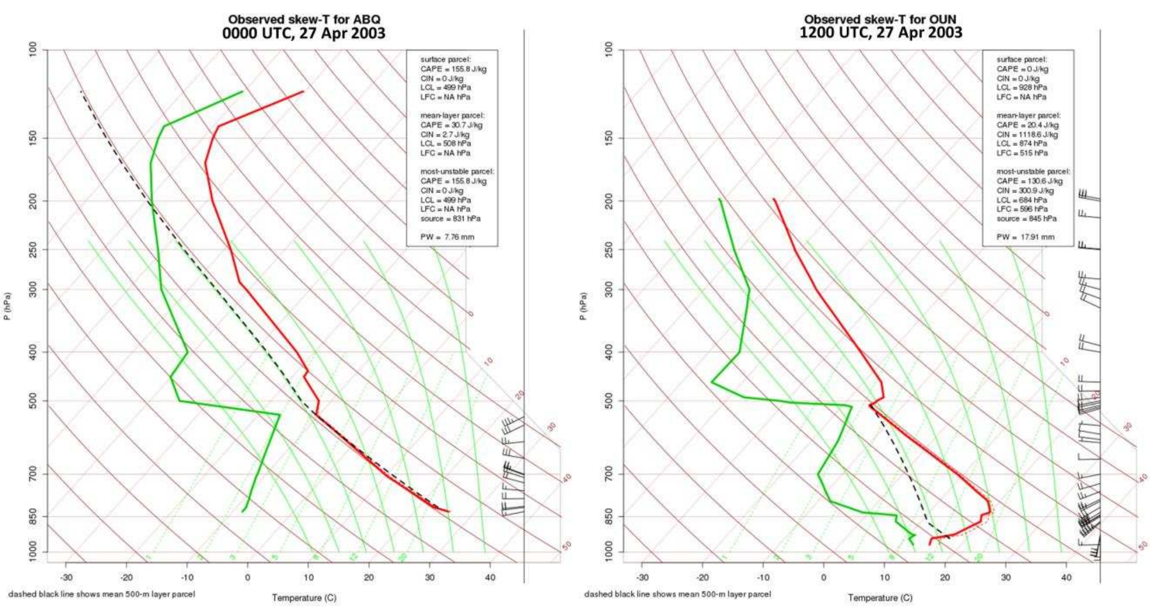

Figure 5.3. Example of back trajectory plot for points surrounding and at the KOUN for 27 April 2003 at 1200 UTC (a) and near the back trajectory point at KABQ on 27 April 2003 at 0000 UTC.

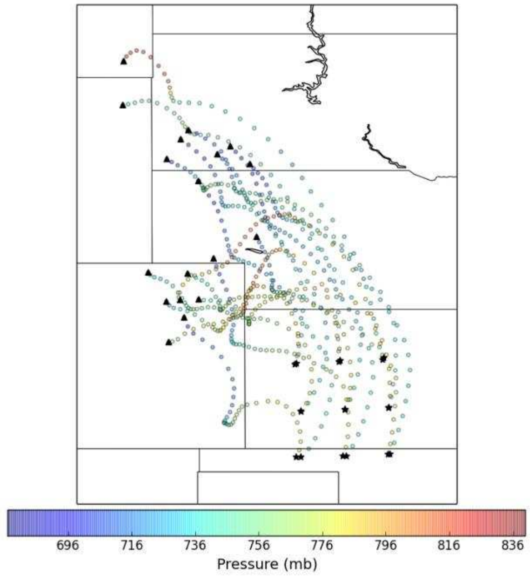

Figure 5.4. Example of back trajectory plot for points surrounding and at the KDDC radiosonde site on 28 May 2003. Back trajectory points are colored by the parcel pressure.

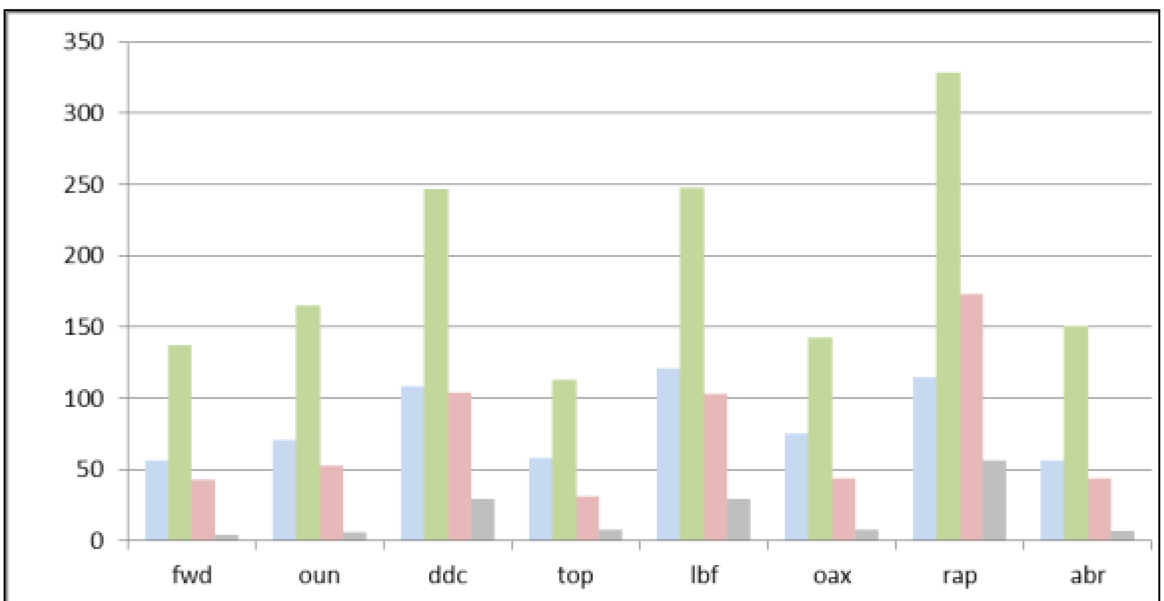

Severe	56	71	108	58	121	75	115	56
>75mb	137	165	247	113	248	143	329	151
>125mb	43	53	104	31	103	44	173	44
>200mb	4	6	29	8	29	8	56	7

Figure 5.5. US GP EML numbers by site (x-axis), by depth and by occurrence of severe in vicinity of the radiosonde site.

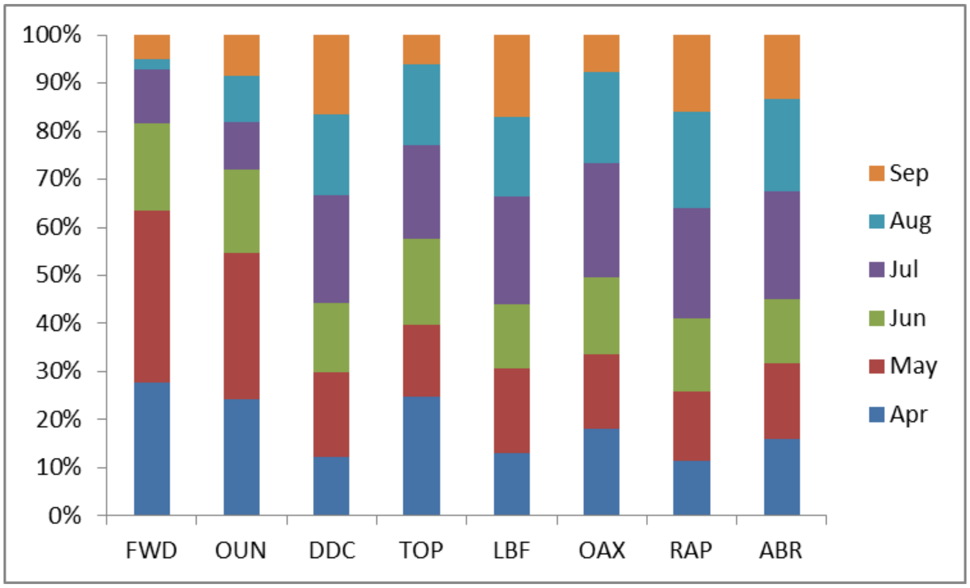

Figure 5.6. EMLs with depth of 75-hPa or greater at each radiosonde site, percent by month.

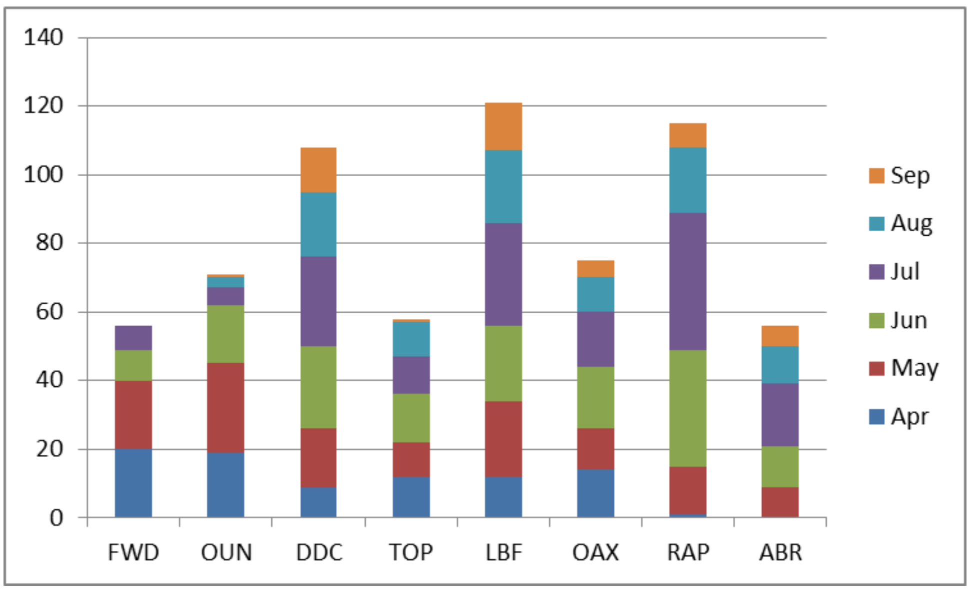

Figure 5.7. Number of severe days associated with EML by site and by month

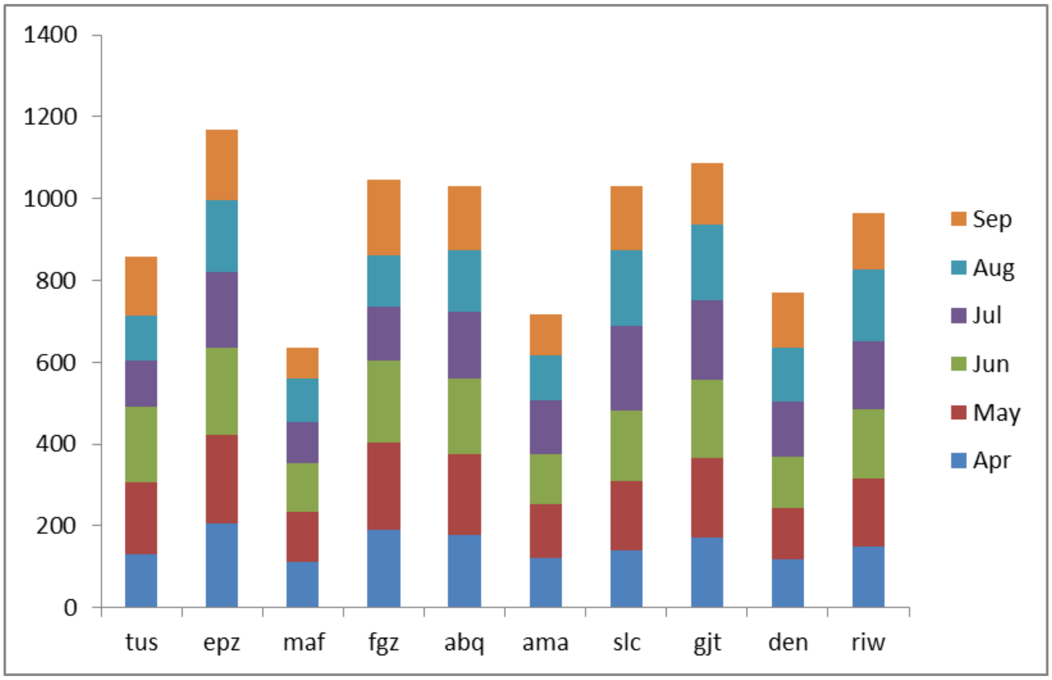

Figure 5.8. Origin Radiosonde Site 0000 UTC mixed layers with tops at 650hPa or lower by site and month

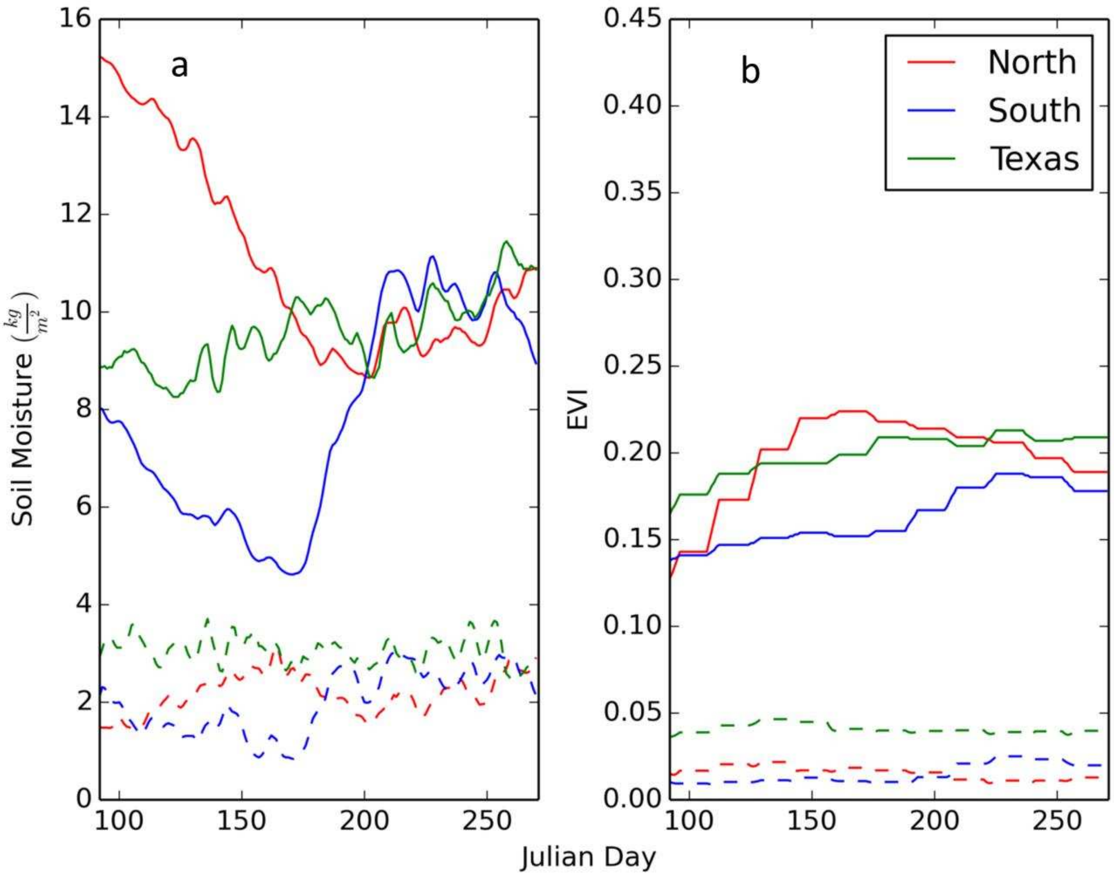

Figure 5.9. Mean (solid) and standard deviation (dashed) of (a) SM and (b) EVI for the three EML origin radiosonde site regions of North (KDEN, KRIW, KSLC, and KGJT), South (KFGZ, KTUZ, KEQZ and KABQ) and Texas (KAMA, KMAF).

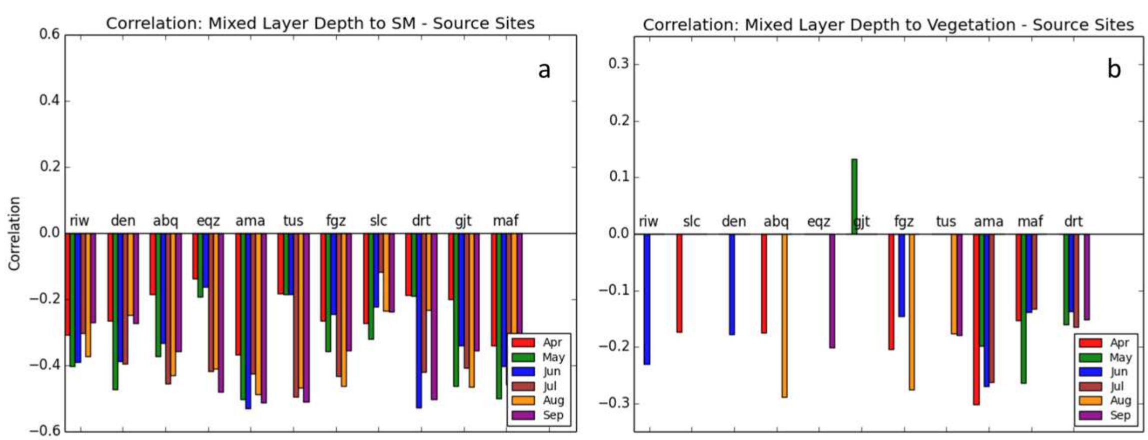

Figure 5.10. Correlation of origin site mixed layer depth to (a) soil moisture and (b) EVI.

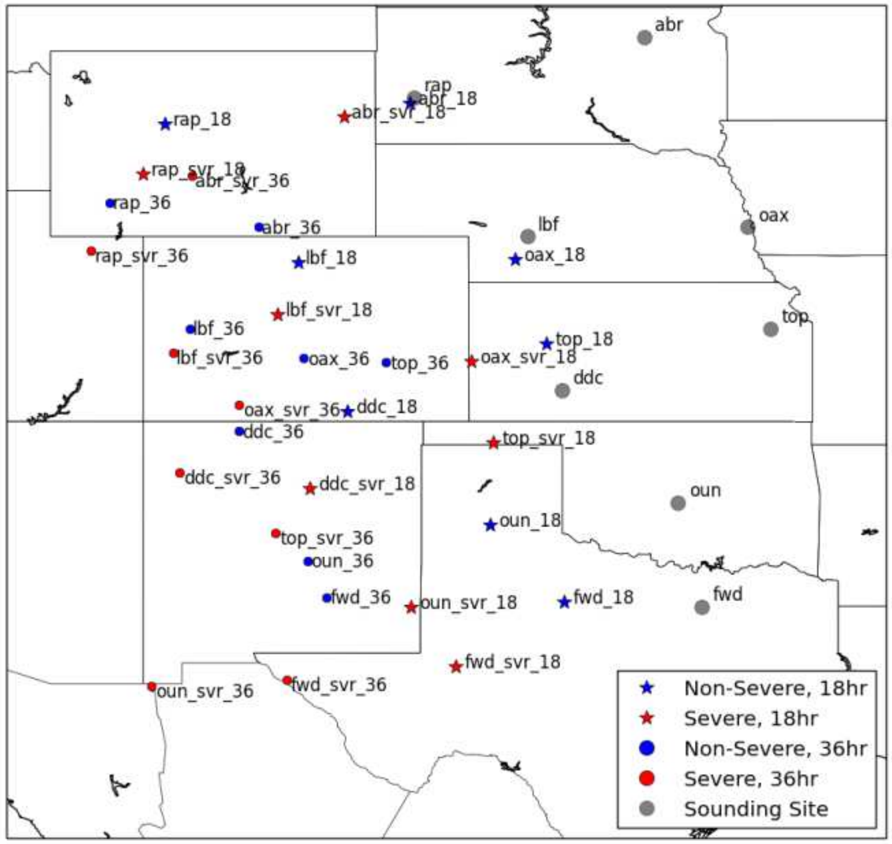

Figure 5.11. Mean back trajectory point for each site for all EMLs associated with severe weather (blue star for 18-hr, blue star for 36-hr) and non-severe weather days (red dot for 18-hr, red star for 36-hr).

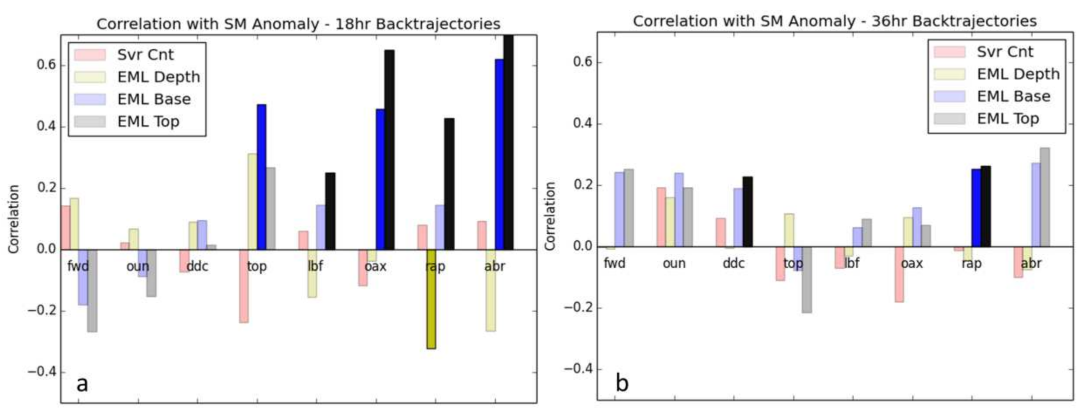

Figure 5.12. Correlations between soil moisture at back trajectory origin and EML characteristics (for all EML depths greater than 75 hPa for (a) 18-hr and (b) 36-hr back trajectories with end points at elevation above 1600m. Statistical significant relationships are in bold (95% level).

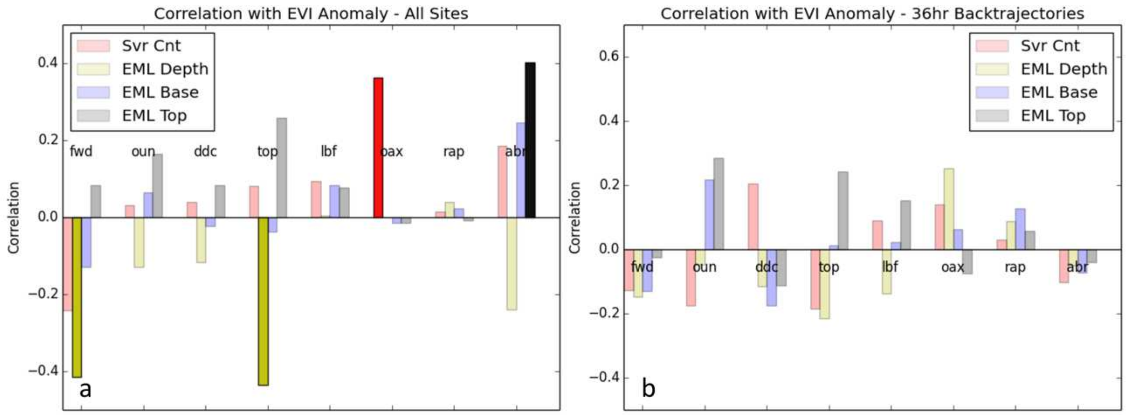

Figure 5.13. Correlations between EVI at back trajectory origin and EML characteristics (for all EML depths greater than 75 hPa for (a) 18-hr and (b) 36-hr back trajectories with end points at elevation above 1200m. Statistical significant relationships are in bold (95% level).

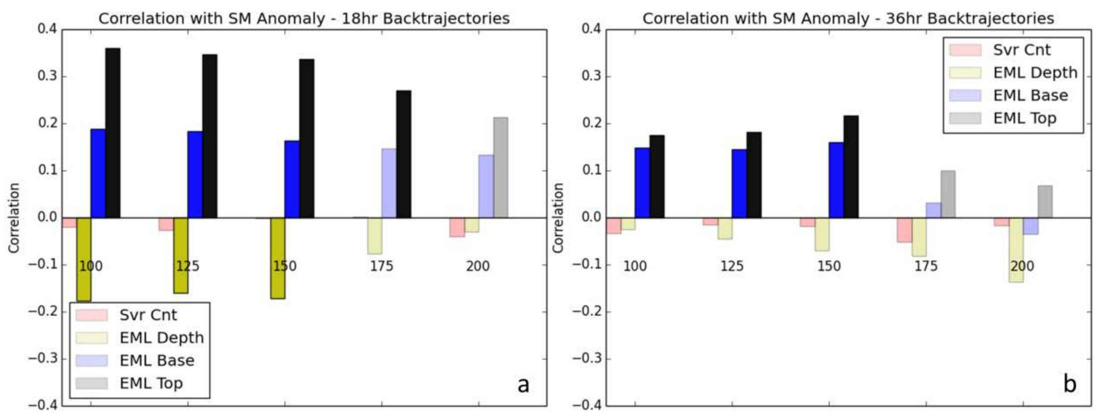

Figure 5.14. Correlations between soil moisture at back trajectory origin for various EML depths for (a) 18-hrexcluding the three southern-most sites and (b) 36-hr back trajectories of only the southern three sites (KFWD, KOUN, and KDDC). Statistical significant relationships are in bold (95% level).

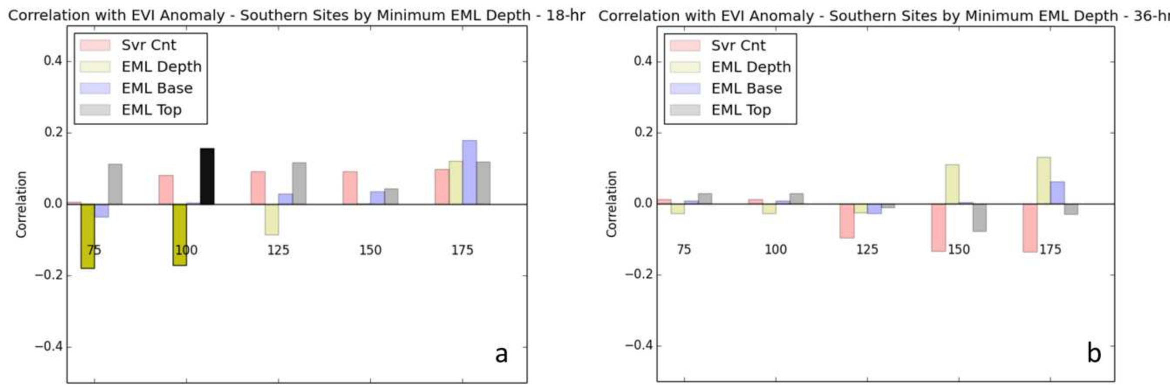

Figure 5.15. Correlations between EVI at back trajectory origin for various EML depths for (a) 18-hr and (b) 36-hr back trajectories excluding the northern four sites (KABR, KRAP, KLBF AND KOAX). Statistical significant relationships are in bold (95% level).

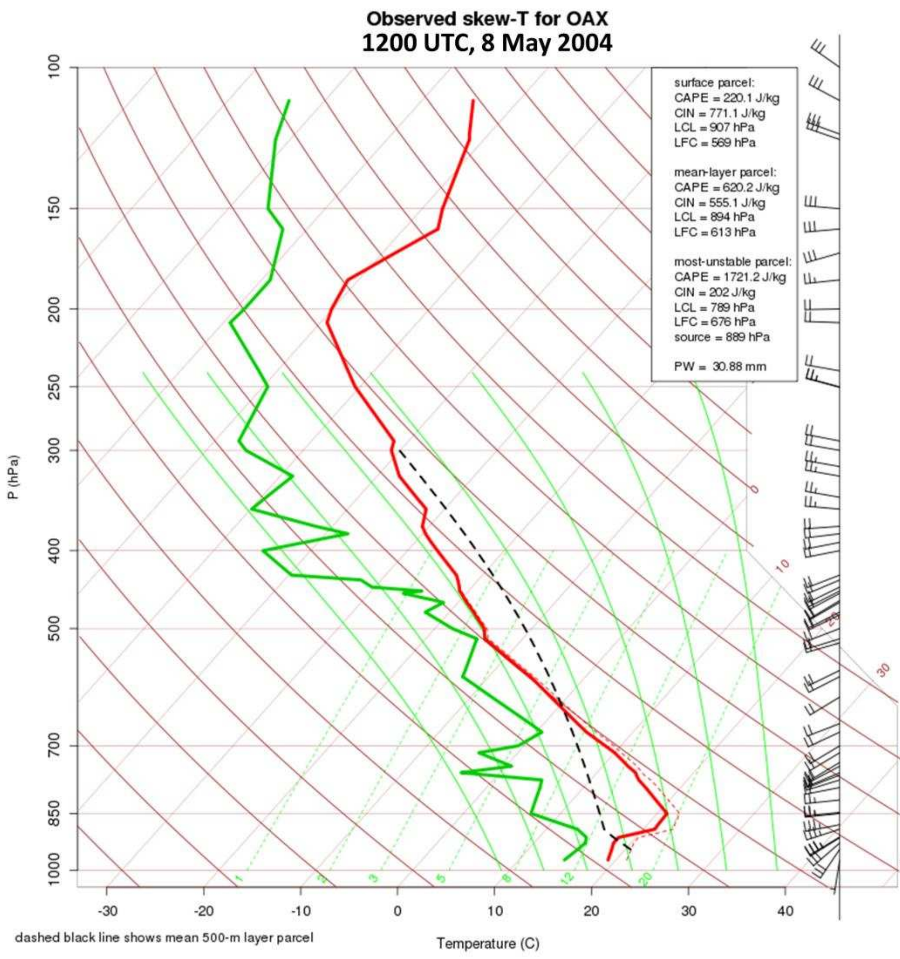

Figure 5.16. Skew-T diagram for KOAX on 8 May 2004 at 1200 UTC.

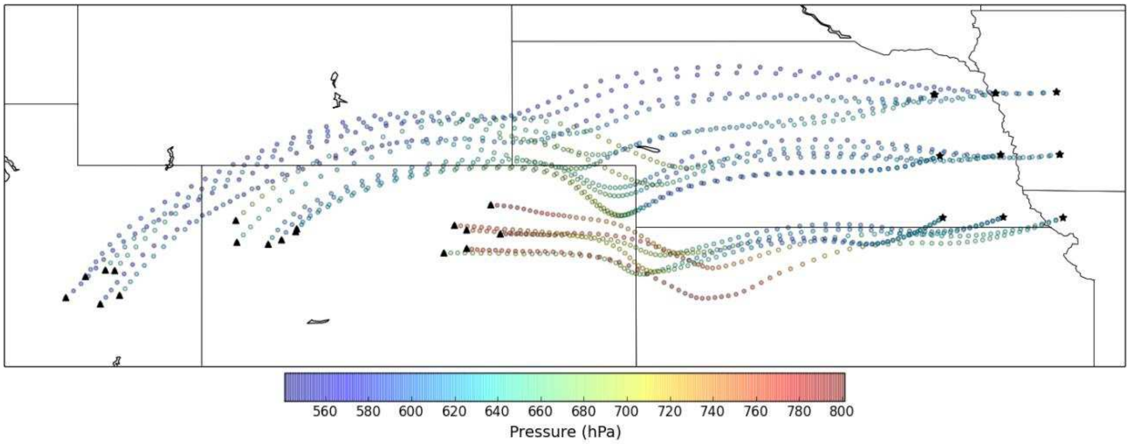

Figure 5.17. 36-hr back trajectories from KOAX beginning at 1200 UTC on 8 May 2004.

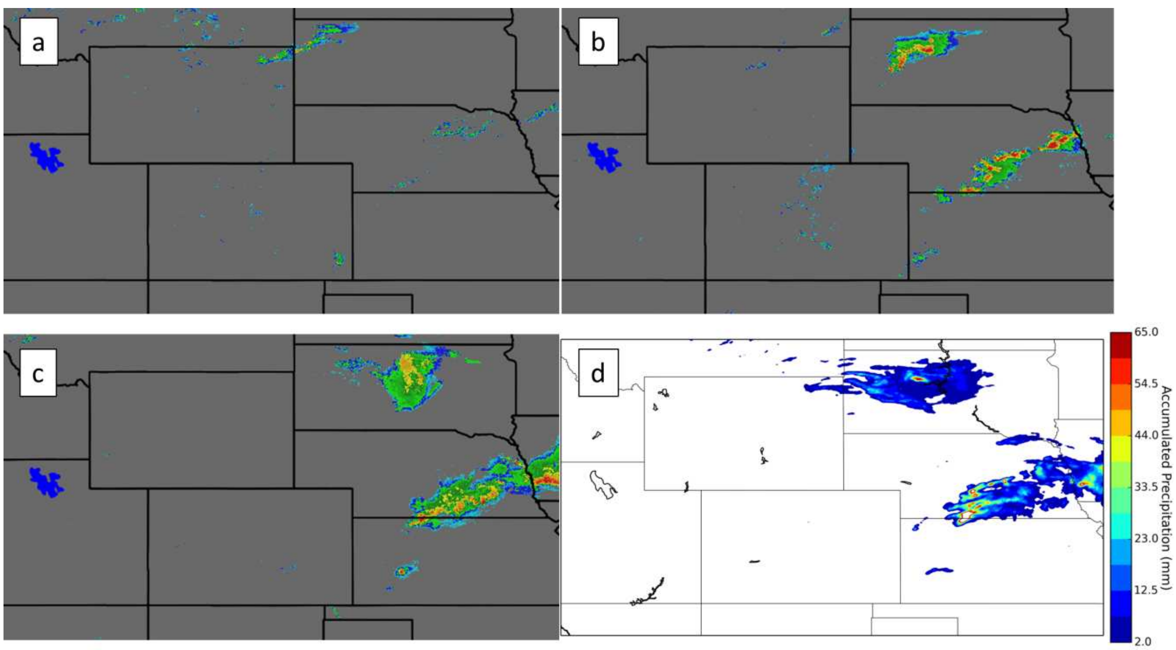

Figure 5.18. NEXRAD composite reflectivity for (a) 2100 UTC (b) 0000 UTC and (c) 0300 UTC on 8 to 9 May 2004. The total observed Stage IV precipitation data for 1200 8 May to 0600 UTC 9 May 2004 is shown in (d).

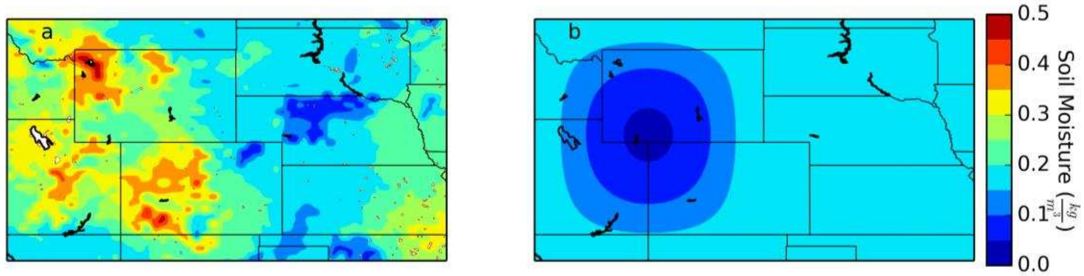

Figure 5.19. Unaltered lower boundary condition land use and SM(a) and altered SM and land use, in this case the DRY run.

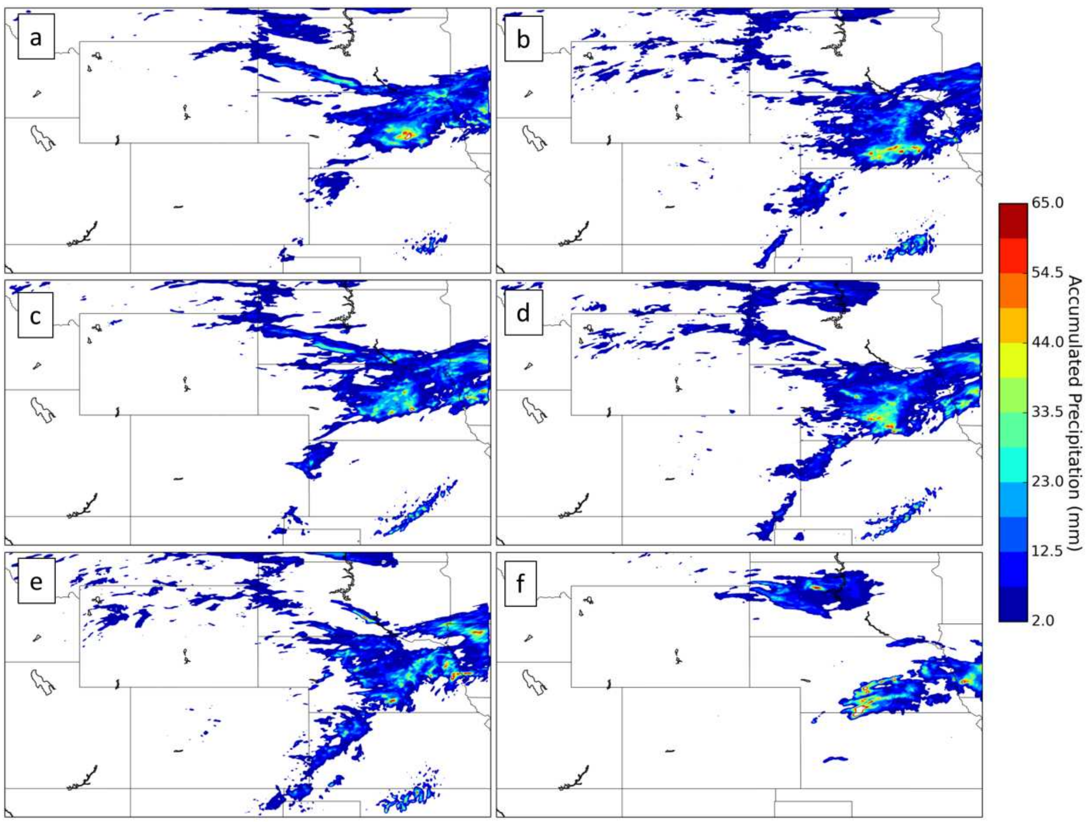

Figure 5.20. Total simulated precipitation for (a) DRY, (b) MOIST, (c) DRY_YSU (d) MOIST_YSU and (e) CNTL.

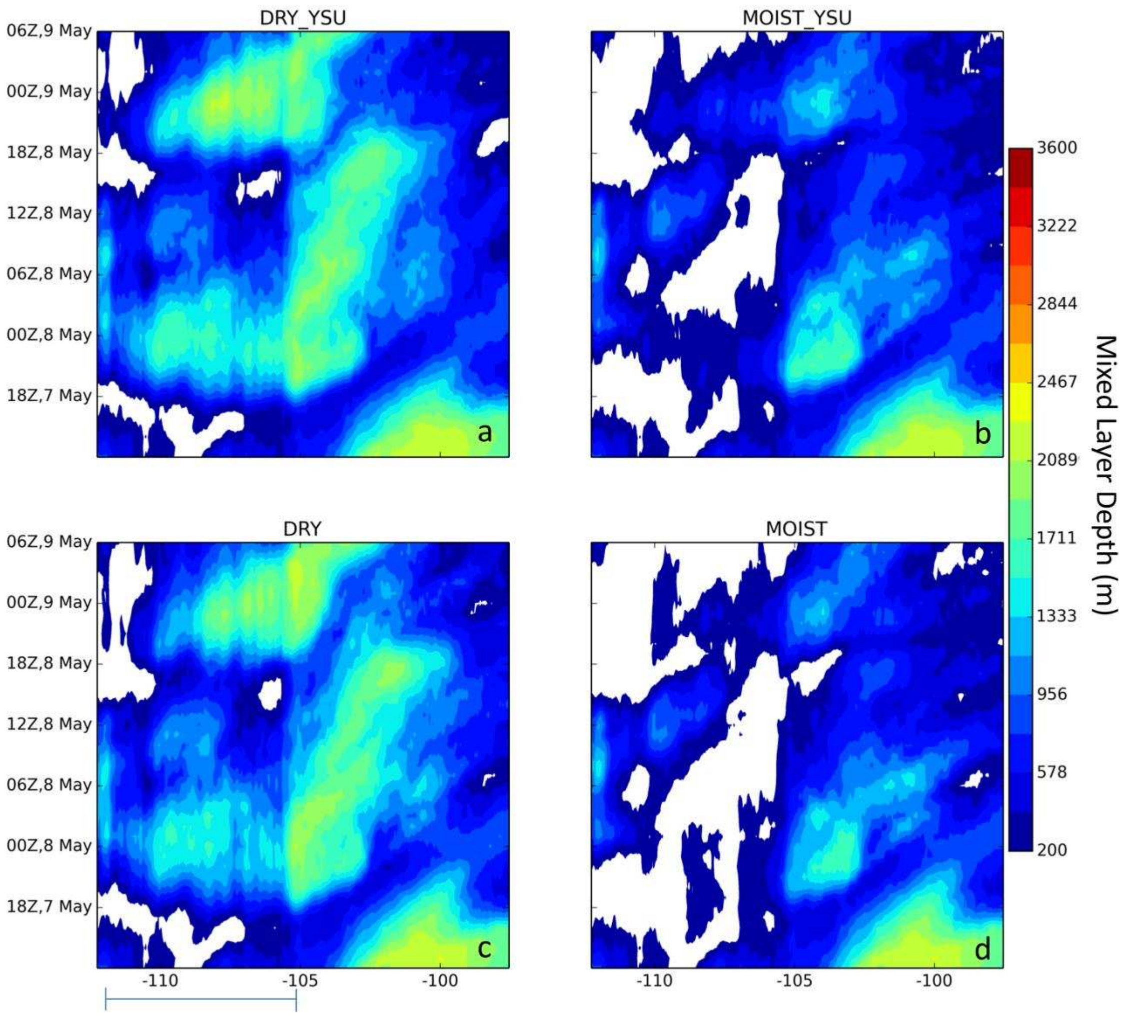

Figure 5.21. Hovmöller diagrams showing mean mixed layer depth (ML between1500 and 7000m) between 38N and 44N along the longitude shown in the x-axis (the east-west length of the 3-km grid spacing domain).

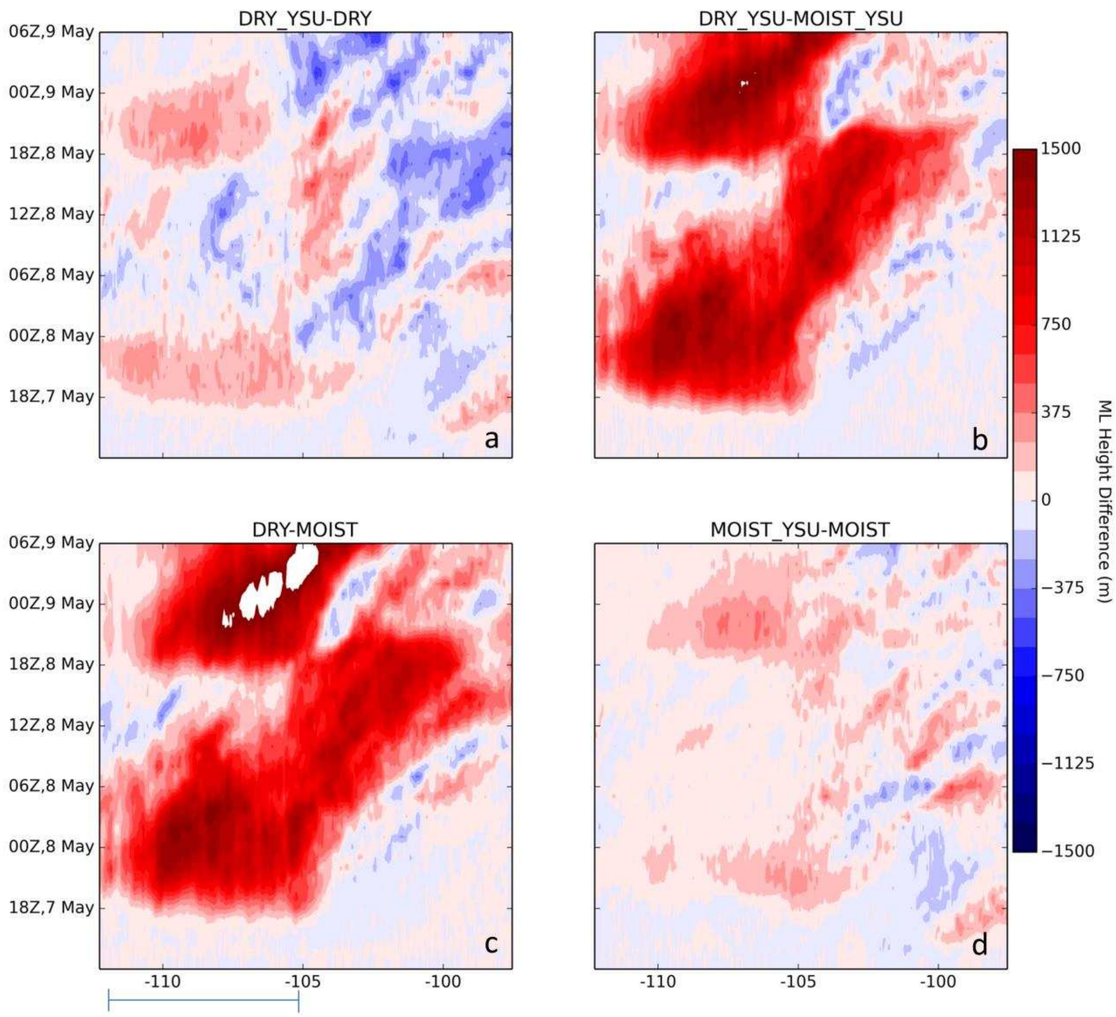

Figure 5.22. ML height difference (ML between 1500 and 7000m) Hovmöller diagrams between each of the simulations from 38N to 44N.

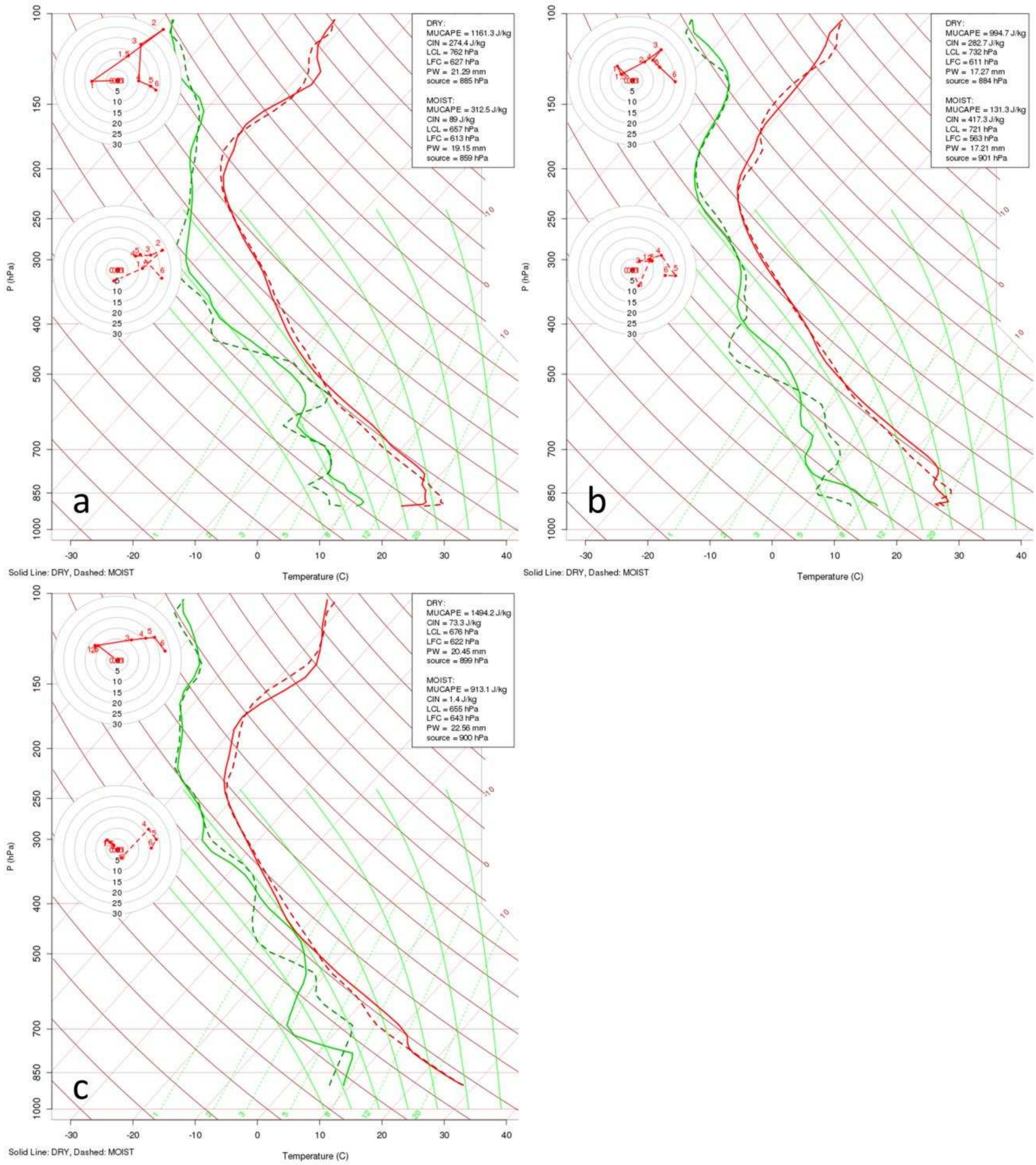

Figure 5.23. Skew-T for 1000 UTC (a), 1400 UTC (b) and 1800 UTC (c) for DRY (solid) and MOIST (dashed) experiments.

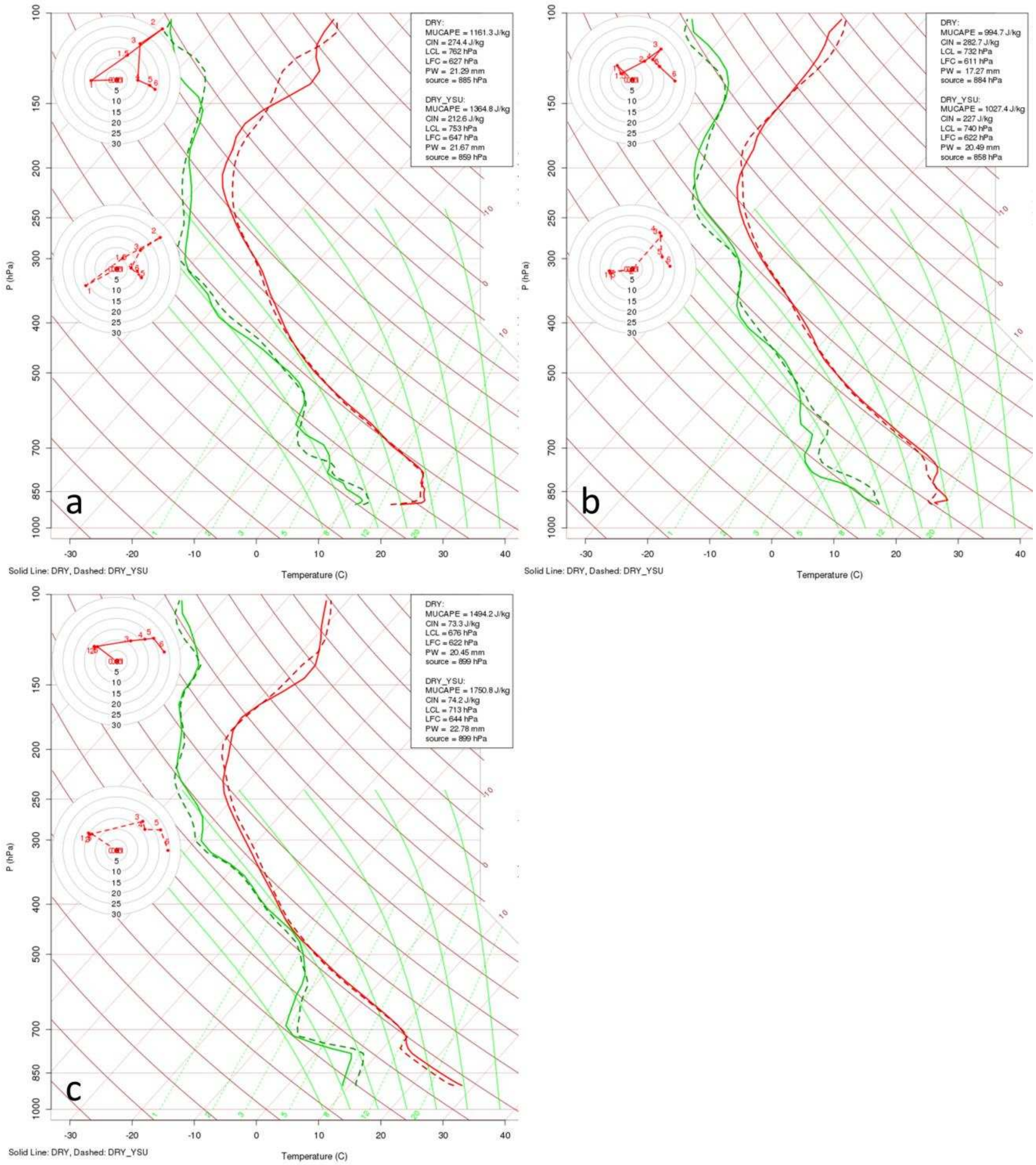

Figure 5.24. Skew-T for 1000 UTC (a), 1400 UTC (b) and 1800 UTC (c) for DRY (solid) and DRY_YSU (dashed) experiments.

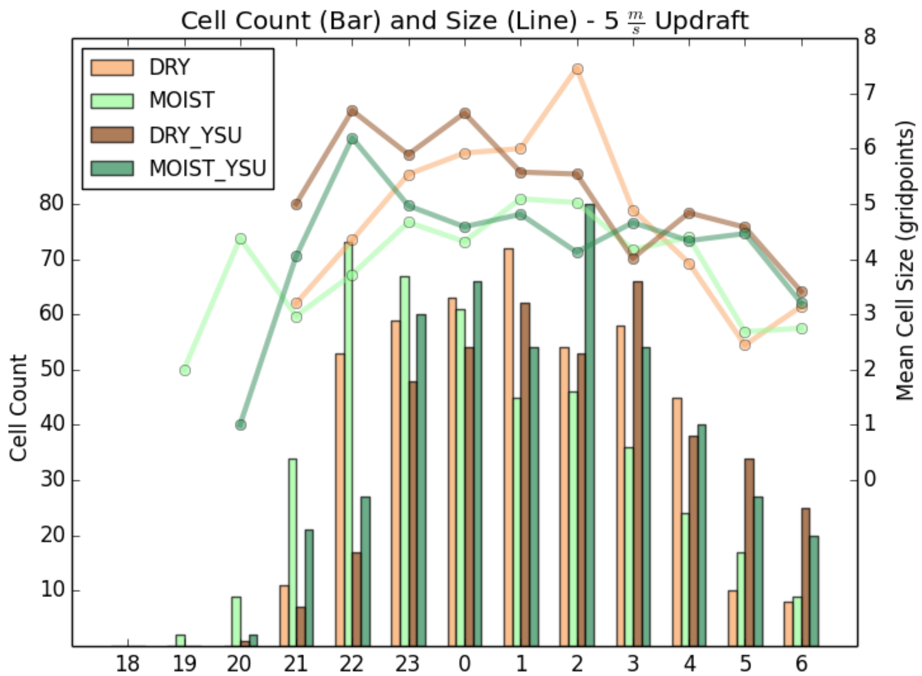

Figure 5.25. Convective Cell count (bar graph) and mean cell size (line graph) by experiment, through time on the x-axis in UTC.

CHAPTER 6

SUMMARY OF OVERALL CONCLUSIONS

- **Climatology of Rocky Mountain/High Plains Born MCS**
    - These MCSs showed distinct, west to east distributions of precipitation, with the distributions showing greater maximum values with a peak at 0700 UTC
    - In terms of total warm season precipitation, in the 500 to 1300m elevations of the Great Plains (GP) to the east in eastern Colorado to central Nebraska and northwest Kansas.
    - Longer lasting MCSs showed longer tracks beginning further south and ending further south. Longer lasting MCSs, in general, began earlier and showed later and greater peaks in total precipitation rate.
    - Variables preceding the MCSs showed different trends according to length of MCS
        - CIN and 0-6 km shear showed consistently greater values in longer lasting MCS, though all shared the same pattern of decreasing values through the night time hours.
        - CAPE showed conditions that improved through time for long lasting MCSs.
        - Large-scale mid-level vertical motion and PW showed no difference across mean conditions ahead of MCSs of different longevity.

- Future work includes utilizing higher fidelity soil moisture data from current satellite platforms, such as SMOS, to enhance the study of land surface interaction with developing, mature and decaying MCSs.

- **Idealized SM MCS Numerical Simulations**
  - Composite initial and boundary conditions developed from reanalysis data from days in which an MCS originated from the source regions of southern Wyoming, Colorado and New Mexico successfully simulated MCSs bearing qualitative similarity to observed precipitation patterns
  - The three control runs for each MCS origin region showed that:
    - The WY simulation produced the earliest MCS transition, but was limited by low PW environment early on and moderate CIN ahead of the system, though the CAPE values were highest ahead of the system, leading to the greatest number of intense embedded cells 0300 to 0600 UTC.
    - The CO case had the most favorable environment for widespread CI in the RM/HP, leading to the greatest number of cells early and the largest MCS, producing the greatest amount of precipitation, aided by the most favorable deep layer shear until 0800 UTC.
    - The NM case, while having the lowest CIN and highest PW values preceding the MCS, shows the lowest overall CAPE, as well as a sharp decline north of the developing system, limiting the size of the MCS and the precipitation output.
  - Idealized experiments, with an imposed SM dipole, with one “sign” of the anomaly in the RM/HP and the other in the GP downstream produced differing

thermodynamic and shear environments depending on the sign of the dipole. Each MCS experienced differing environmental stability and shear depending on where the SM anomaly was traversed.

- Sensitivity tests changing the PBL parameterization showed that a smaller difference than that found by changing the sign of the SM dipole alone, with the main difference being more widespread initial convection when using the non-local PBL scheme.
- Future Work:
    - A more idealized study of the importance of land use, SM and slope play on the initiation of convection and the development of subsequent MCSs will be undertaken.
    - While the differences between the MYNN and YSU PBL parameterization scheme were subtle, further study should be undertaken to understand the sensitivity of MCS lifecycle to PBL scheme with varying topography, land cover, soil type and SM.
    - Simulating each regional MCS in quasi-idealized environment emulating modern estimates to the region brought about by climate change to assess the impact on the hydrology of the region to future change.
    - Additionally, the transportability of this study to similar MCS regimes in other regions of the world, including China and Argentina, should be explored to study the effects of idealized soil moisture variations to differences in background flow and land/ocean configurations presented in other regions.

- **Climatology of CI in the Rocky Mountain/High Plains**
    - When comparing the timing of CI over anomalies of SM and vegetation, the timing of CI had a stronger relationship with SM, with earlier CI over wetter than average soils. Greater vegetation generally followed this pattern (more vegetation, earlier CI) except for May where this relationship was reversed.
    - When the overlaying CAPE, CIN and PW at CI and null points was examined, it was nearly universal that higher SM/EVI was associated with more favorable conditions for convection above with May and June at CI points showing an inverse relationship.
    - When examining the covariance of SM and EVI anomalies at CI points, July and August showed expected covariance relationships with concurrently measured convective variables (i.e., high SM/vegetation associated with high CAPE and vice versa for low SM/vegetation) while May and June higher CAPE and CIN over low vegetation anomalies.
    - Future Work:
        - Expanding beyond the Front Range of the central Rocky Mountains to other parts of the CONUS to study the impact of varying SM and vegetation on CI in concert with changes in atmospheric variables
        - A modelling study, similar to Burghardt et al. (2014), in which several cases of CI focused on different regions of the Rocky Mountains and high plains, including MCS days and non-MCS days are simulated at cloud-permitting horizontal grid spacing. The SM and or vegetation would be raised and lowered to test the sensitivity of CI and subsequent MCS

formation on land surface parameters. This modelling study would be useful in understanding factors governing CI that are not possible in an observed-data only study

- **EML Relationship to Origin Region Surface Properties**
    - From a climatology of EMLs at GP radiosonde sites back trajectories (BT) were conducted for 18 and 36 hours.
        - BT on days with severe weather at the GP site were further west and south from the origin point.
        - SM showed a negative correlation to EML depth at northern GP sites while vegetation showed a negative significant negative correlation at southern GP sites to EML depth.
    - A modeling case study was conducted, altering SM in the EML origin region and testing the sensitivity of results to PBL parameterization.
        - With the soil dried in the origin region, results showed better performance compared to the control and moistened soil run, though positional error of the precipitation maximum in south NE was greater.
        - While the YSU PBL scheme produced deeper PBLs over the origin region, the deep ML was not transported downstream as a deep EML as it was in the MYNN scheme, leading to differences in precipitation timing and intensity.
    - Future Work:

- Examine the role and sensitivity of EML characteristics to upstream surface properties in early day initiated severe convection over isolated, elevated terrain.
- Study should be undertaken to understand the role of EMLs in invigorating nocturnal GP convection, either in assisting nocturnal convection initiation or in invigorating rearward development of convection in an existing MCS.

REFERENCES

Avissar, R. and Y. Q. Liu, 1996: Three-dimensional numerical study of shallow convective clouds and precipitation induced by land surface forcing. *J. Geophys. Res.*, **101.D3**, 7499-7518.

Banacos, P. C., and M. L. Ekster, 2010: The association of the elevated mixed layer with significant severe weather events in the Northeast United States, *Wea. Forecasting*, **25**, 1082-1102.

Banta, R. M. and C. B. Schaaf, 1987: Thunderstorm Genesis Zones in the Colorado Rocky Mountains as Determined by Traceback of Geosynchronous Satellite Images. *Mon. Wea. Rev.*, **115**, 463-476.

Benjamin, S. G., and T. N. Carlson, 1986: Some effects of surface heating and topography on the regional severe storm environment. Part I: Three-dimensional simulation. *Mon. Wea. Rev.*,**114,** 307–329.

Benjamin, S. G., 1986: Some effects of surface heating and topography on the regional severe storm environment. Part II: Two-dimensional idealized experiments. *Mon. Wea. Rev.*, **114,** 330–343.

Blackadar, A. K. 1957: Boundary layer wind maxima and their significance for the growth of nocturnal inversions, *Bull. Amer. Meteor. Soc.*, **38**, 283-290.

Bright, D. R., and S. L. Mullen, 2002: Short-range ensemble forecasts of precipitation during the southwest monsoon. *Wea. Forecasting*, **17**, 1080–1100.

Bryan, G. H., and H. Morrison, 2012: Sensitivity of a Simulated Squall Line to Horizontal 644 Resolution and Parameterization of Microphysics. *Mon. Wea. Rev*., **140**, 202–225.

Burghardt, B. J., C. Evans, and P. J. Roebber, 2014: Assessing the predictability of convection initiation in the high plains using an object-based approach. *Wea. Forecasting*, **29**, 403-418.

Carbone, R. E., J. D. Tuttle, D. A. Ahijevych, and S. B. Trier, 2002: Inferences of predictability associated with warm season precipitation episodes. *J. Atmos. Sci*., **59** (13), 2033-2056.

Carbone, R. E. and J. D. Tuttle, 2008: Rainfall Occurrence in the U.S. Warm Season: The Diurnal Cycle. *J. Climate*, **21**, 4132-4146.

Carlson, T. N., and F. H. Ludlam, 1968: Conditions for the occurrence of severe local storms. *Tellus*, **20,** 203-226.

Carlson, T. N., S. G. Benjamin, G. S. Forbes, and Y. F. Li, 1983: Elevated mixed layers in the regional severe storm environment: Conceptual model and case studies. *Mon. Wea. Rev.*, **111,** 1453-1473.

Chou, M. D., and M. J. Suarez, 1999: A solar radiation parameterization for atmospheric studies. NASA Tech. Rep. Series on Global Modeling and Data Assimilation, NASA/TM-1999-104606, **15**, 40 pp.

Clark, A. J., R. G. Bullock, T.L. Jensen, M. Xue, and F. Kong, 2014: Application of Object-Based Time-Domain Diagnostics for Tracking Precipitation Systems in Convection-Allowing Models. *Wea. Forecasting*, **29**, 517-542.

Coniglio, M. C., and D. J. Stensrud, 2001: Simulation of a progressive derecho using composite initial conditions. *Mon. Wea. Rev.*, **129,** 1593-1616.

Coniglio, M. C., K. L. Elmore, J. S. Kain, S. J. Weiss, M. Xue, and M. L. Weisman, 2010: Evaluation of WRF model output for severe weather forecasting from the 2008 NOAA Hazardous Weather Testbed Spring Experiment. *Wea. Forecasting*, **25**, 408–427.

Coniglio, M. C., J. Correia, P. T. Marsh, and F. Kong, 2013: Verification of convection-allowing WRF Model forecasts of the planetary boundary layer using sounding observations. *Wea. Forecasting*, **28**, 842-862.

Cotton, W. R., R. L. George, P. J. Wetzel, R. L. McAnelly, 1983: A long-lived mesoscale convective complex, I, The mountain-generated component, *Mon. Weather Rev.*, **111**, 1893–1918.

Cotton, W. R., and R. A. Anthes, 1989: Storm and Cloud Dynamics. International Geophysics Series, Vol. 44, Academic Press, 883 pp.

Crow, L. W., 1969: Relationships between hail and rain in Kansas, Nebraska and Eastern Colorado. LWC Final Report, Number 76, Contract NSF C-522, National Science Foundation.

Draxler, R. R., and G. D. Hess, 1997: Description of the HYSPLIT_4 modeling system. NOAA Tech. Memo. ERL ARL-224, 24 pp.

Duda, J. D., and W. A. Gallus, 2013: The impact of large-scale forcing on skill of simulated convective initiation and upscale evolution with convection-allowing grid spacings in the WRF. *Wea. Forecasting*, **28**, 994–1018.

Ek, M. B., K. E. Mitchell, Y. Lin, P. Grunmann, E. Rodgers, G. Gayno, and V. Koren, 2003: Implementation of the upgraded Noah land surface model in the NCEP operational mesoscale Eta model. *J. Geophys. Res.*, **108**, 8851.

Ek, M. B., and A. A. M. Holtslag, 2004: Influence of soil moisture on boundary layer cloud development. *J. Hydrometeor.*,**5**, 86–99.

Erlingis, J. M., and A. P. Barros, 2014: A study of the role of daytime land–atmosphere interactions on nocturnal convective activity in the southern Great Plains during CLASIC. *J. Hydrometeor.*, **15**, 1932–1953.

Fast, J. D., and M. D. McCorcle, 1990: A Two-Dimensional Numerical Sensitivity Study of the Great Plains Low-Level Jet. *Mon. Wea. Rev*., **118**, 151–164.

Fawbush, E.J., and R.C. Miller, 1952: A mean sounding representative of the tornadic airmass environment. *Bull. Amer. Meteor. Soc.*, **33**, 303-307.

Findell, K. L., and Elfatih Eltahir, 2003: Atmospheric controls on soil moisture-boundary layer interactions. Part II: Feedbacks within the continental United States. *J. Hydrometeor.*, **4:3**., 570-583.

Ford, T. W., A. D. Rapp, and S. M. Quiring, 2015: Does afternoon precipitation occur preferentially over dry or wet soils in Oklahoma? *J. Hydrometeor.*, **16**, 874–888.

Frey, B. J. and D. Dueck, 2007: Clustering by passing messages between data points. *Science* **315**, 972–976.

Fritsch, J. M., and G. S. Forbes, 2001: Mesoscale convective systems. Severe Convective Storms, Meteor. Monogr., **50**, Amer. Meteor. Soc., 323–357.

Frye, J. D., and T. L. Mote, 2010: Convection initiation along soil moisture boundaries in the southern Great Plains. *Mon. Wea. Rev.*, **138**, 1140–1151.

Gensini, V. A., T. L. Mote, and H. E. Brooks, 2014: Severe thunderstorm reanalysis environments and collocated radiosonde observations, *J. Appl. Meteorol. Climatol.*, **53**, 742–7513.

Henz, J., 1974: Colorado High Plains Thunderstorm Systems - A Radar Synoptic Climatology. Colorado State University, MS Thesis.

Holt, J. D., D. Niyogi, F. Chen, K. Manning, M. A. LeMone, and A. Qureshi, 2006: Effect of Land–Atmosphere Interactions on the IHOP 24–25 May 2002 Convection Case. *Mon. Wea. Rev.*, **134**, 113-133.

Holton, J. R. 1966: The diurnal boundary layer wind oscillation above sloping terrain, *Tellus*, **19**, 199-205.

Hong, S. Y., and J. O. J. Lim, 2006: The WRF single-moment 6-class microphysics scheme (WSM6). *J. Korean Meteor. Soc*., **42**, 129–151.

Houze, R.A., Jr., B.F. Smull, and P. Dodge, 1990: Mesoscale organization of springtime rainstorms in Oklahoma. *Mon. Wea. Rev*., **118**, 613–654.

Houze, R.A., Jr., 2004: Mesoscale convective systems, *Rev. Geophys*., **42**, RG4003.

Janjic, Z. I., 1990: The step-mountain coordinate: Physical package. *Mon. Wea. Rev*., **118**, 1429–1443.

Jones, E., E. Oliphant, P. Peterson, SciPy: Open Source Scientific Tools for Python, 2001-, http://www.scipy.org/ [Online; accessed 2016-05-19].

Kain, J. S., 2004: The Kain–Fritsch convective parameterization scheme: An update. *J. Appl. Meteor.*, **43**, 170–181.

Keene, K.M., and R.S. Schumacher, 2013: The bow and arrow mesoscale convective structure. *Mon. Wea. Rev*., **141**, 1648-1672.

Koster, R. D. and Coauthors, 2004: Regions of strong coupling between soil moisture and precipitation. *Science,* **305.5687**, 1138-1140.

Lamb, P. J., D. H. Portis, and A. Zangvil, 2012: Investigation of Large-Scale Atmospheric Moisture Budget and Land Surface Interactions over U.S. Southern Great Plains including for CLASIC (June 2007). *J. Hydrometeor.*, **13**, 1719-1738.

Lanicci, J. M., and T. T. Warner, 1991: A synoptic climatology of the elevated mixed-layer inversion over the southern Great Plains in spring. Part III: Relationship to severe-storms climatology. *Wea. Forecasting*, **6,** 198–213.

Lanicci, J. M., and T. T. Warner, 1997: A case study of lid evolution using analyses of observational data and a numerical model simulation. *Wea. Forecasting*, **12,** 228–252.

Lin, Y. and K. E. Mitchell, 2005: The NCEP Stage II/IV hourly precipitation analyses: development and applications. Preprints, *19th Conf. on Hydrology, American Meteorological Society*, San Diego, CA, 9-13 January 2005, Paper 1.2.

Lock, N. A., and A. L. Houston, 2014: Empirical examination of the factors regulating thunderstorm initiation. *Mon. Wea. Rev.*, **142**, 240–258.

Maddox, R. A., 1980: Meoscale Convective Complexes. *Bull. Amer. Meteor. Soc.*, **61**, 1374–1387.

Mellor, G. L., and T. Yamada, 1982: Development of a turbulence closure model for geophysical fluid problems. *Rev. Geophys. Space Phys*., **20**, 851–875.

Mesinger, F., and Coauthors, 2006: North American regional reanalysis, *Bull. Am. Meteorol. Soc.*, **87**(3), 343–360.

Nakanishi, M., and H. Niino, 2006: An improved Mellor–Yamada level-3 model: Its numerical stability and application to a regional prediction of advection fog. Bound.-Layer Meteor., **119**, 397–407.

Oberthaler, A. J., and P. M. Markowski, 2013: A Numerical Simulation Study of the Effects of Anvil Shading on Quasi-Linear Convective Systems. *J. Atmos. Sci*., **70**, 767–793.

Parker, M.D. and R.H. Johnson, 2000: Organizational modes of midlatitude mesoscale convective systems. *Mon. Wea. Rev*., **128**, 3413-3436.

Pedregosa, G. and Coauthors, 2011: Scikit-learn: Machine learning in Python. *J. Machine Leanring Res.*, **12**, 2825–2830.

Peters, J. M. and R. S. Schumacher, 2015: The Simulated Structure and Evolution of a Quasi-Idealized Warm Season Convective System with a Training Convective Line. *J. Atmos. Sci* , **72**, 1987–2010.

Pielke, R. A., Sr., T. J. Lee, J. H. Copeland, J. L. Eastman, C. L. Ziegler, and C. A. Finley, 1997: Use of USGS-Provided Data to Improve Weather and Climate Simulations. *Ecological Applications*, **7.1**, 3-21.

Rotunno, R., J. B. Klemp, and M. L. Weisman, 1988: A Theory for Strong, Long-Lived Squall Lines. *J. Atmos. Sci*., **45**, 463–485.

Skamarock, W. C., and Coauthors, 2008: A description of the Advanced Research WRF version 3. NCAR Tech. Note NCAR/TN-475+STR, 113 pp.

Stensrud, D. J., 1993: Elevated residual layers and their influence on surface boundary layer evolution. *J. Atmos. Sci.,* **50,** 2284–2293.

Stevenson, S. N. and R. S. Schumacher, 2014: A 10-year Survey of Extreme Rainfall Events in the Central and Eastern United States Using Gridded Multisensor Precipitation Analyses. *Mon. Wea. Rev.,* 142, 3147–3162.

Strahler, A., and Coauthors, 1999: MODIS land cover product, Algorithm Theoretical Basis Document (ATBD), Version 5.0. Boston, MA: Center for Remote Sensing, Department of Geography, Boston University.

Thompson, G., P. R. Field, R. M. Rasmussen, and W. D. Hall, 2008: Explicit forecasts of winter precipitation using an improved bulk microphysics scheme. Part II: Implementation of a new snow parameterization. *Mon. Wea. Rev.*, **136**, 5095–5115.

Tripoli, G. J., and W. R. Cotton, 1989: Numerical simulation of an observed orogenic mesoscale convective system. Part 2: Analysis of governing dynamics. *Mon. Wea. Rev.*, **117,** 305–328.

Troen, I. and L. Mahrt, 1986: A simple model of the atmospheric boundary layer: Sensitivity to surface evaporation. *Bound. Layer Meteorol.*, **37**, 129-148.

Zhang, Y., F. Zhang, D. J. Stensrud, and Z. Meng, 2015: Practical predictability of the 20 May 2013 tornadic thunderstorm event in Oklahoma: Sensitivity to synoptic timing and topographical influence. *Mon. Wea. Rev.*, **143**, 2973–2997.

Zhou, X. and B. Geerts, 2013: The Influence of Soil Moisture on the Planetary Boundary Layer and on Cumulus Convection over an Isolated Mountain. Part I: Observations. *Mon. Wea. Rev*., **141**, 1061-1078.